

# Thermo-Fluids and Acoustics



## Simulation of Acoustic Fluid-Structure Interaction with Advanced Boundary Element Method

Lothar Gaul<sup>1</sup> and Matthias Fischer<sup>2</sup>

Institut A für Mechanik, Universität Stuttgart  
 Pfaffenwaldring 9, 70550 Stuttgart, Germany

<sup>1</sup> gaul@mecha.uni-stuttgart.de

<sup>2</sup> fischer@mecha.uni-stuttgart.de

**Keywords:** Fast Multipole BEM, Acoustic-Structure Interaction, Iterative Solver

**Abstract.** The fast multipole boundary element method is presented for the simulation of acoustic fluid-structure interaction problems. The BEM is coupled to a finite element formulation for plate vibrations by a mortar algorithm to take into account the interaction effects. For the solution of the coupled system of equations a nested iteration scheme is employed. The methodology is applied to simulate experiments on active structural-acoustic control.

### Introduction

In many applications the interaction between acoustic fluid and vibrating structure plays a dominating effect. This situation is encountered in particular for thin and flexible structures that are easily excited by the sound pressure. For reliable simulations, the two fields must be fully coupled. Thus, a BEM-FEM scheme [2] is developed for the model problem as displayed in Fig. 1. The structure is modeled as a Kirchhoff plate on the interaction boundary  $\Gamma^{\text{int}}$  where the out-of-plane displacement is denoted by  $w$  and the loading  $f = f^f + f^e$  consists of surface forces due to the acoustic field  $f^f$  and externally applied forces  $f^e$ . For time-harmonic behavior  $e^{-i\omega t}$ , the pressure  $p$  in the acoustic field  $\Omega_f$  is governed by the Helmholtz equation  $\Delta p + \kappa^2 p = 0$  with the circular wavenumber  $\kappa = \omega/c_f$  and speed of sound  $c_f$ . The acoustic flux on the boundary is defined as  $q = \partial p / \partial \vec{n}_f$  where  $\vec{n}_f$  is the normal vector on the boundary  $\partial\Omega_f = \Gamma$  pointing outwards from  $\Omega_f$ . The boundary  $\Gamma = \Gamma^{\text{int}} \cup \Gamma^{\text{N}} \cup \Gamma^{\text{D}}$  is composed of acoustic-structure interface, Neumann boundary and Dirichlet boundary. The orientation of the normal vector on the acoustic-structure interface is defined as  $\vec{n} = \vec{n}_f = -\vec{n}_s$ , yielding the coupling conditions to enforce equilibrium  $p = f$  and continuity  $q = -\rho_f \omega^2 w$ .

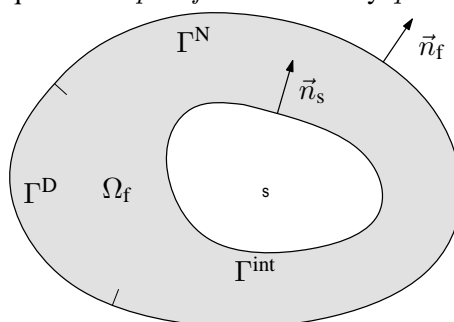


Figure 1: Acoustic-structure interaction

### Fast Multipole Boundary Element Method

For the acoustic domain  $\Omega_f$  a BEM is derived. Weighting the Helmholtz equation for the acoustic pressure  $p$  with the fundamental solution  $P^*(x, y) = e^{i\kappa|\vec{x}-\vec{y}|} / (4\pi|\vec{x}-\vec{y}|)$  and applying Green's second theorem yields the representation formula

$$p(x) = \int_{\Gamma} P^*(x, y) q(y) ds_y - \int_{\Gamma} \frac{\partial P^*(x, y)}{\partial n_y} p(y) ds_y, \quad x \in \Omega_f. \quad (1)$$

For details on the derivation of boundary integral formulations, it is referred to [5]. Taking the limit on the smooth boundary  $\Omega_f \ni \vec{x} \rightarrow \Gamma$ , one obtains the boundary integral equation

$$p(x) = \frac{1}{2}p(x) + \underbrace{\int_{\Gamma} P^*(x, y) q(y) ds_y}_{(Vq)(x)} - \underbrace{\int_{\Gamma} \frac{\partial P^*(x, y)}{\partial n_y} p(y) ds_y}_{(Kp)(x)}, \quad x \in \Gamma, \quad (2)$$

where  $(Vq)(x)$  and  $(Kp)(x)$  are the single and double layer potential, respectively. The hyper-singular boundary integral equation is obtained by taking the normal derivative of (1)

$$q(x) = \frac{1}{2}q(x) + \underbrace{\int_{\Gamma} \frac{\partial P^*(x, y)}{\partial n_x} q(y) ds_y}_{(K'q)(x)} - \underbrace{\int_{\Gamma} \frac{\partial^2 P^*(x, y)}{\partial n_x \partial n_y} p(y) ds_y}_{-(Dp)(x)}, \quad x \in \Gamma, \quad (3)$$

where  $(K'q)(x)$  and  $(Dp)(x)$  are the adjoint double layer potential and the hyper-singular operator, respectively.

To obtain a BEM, a boundary triangulation is introduced and the acoustic pressure and flux are approximated by piecewise linear and constant shape functions, respectively,

$$p_h(x) = \boldsymbol{\varphi}^p(x)^T \mathbf{p}, \quad q_h(x) = \boldsymbol{\varphi}^q(x)^T \mathbf{q}. \quad (4)$$

Galerkin testing yields, for example, the matrix of the discrete single layer potential

$$\mathbf{V} = \int_{\Gamma} \boldsymbol{\varphi}^q(x) \int_{\Gamma} P^*(x, y) \boldsymbol{\varphi}^q(y)^T ds_y ds_x. \quad (5)$$

The fast multipole method can be used to evaluate efficiently the matrix-vector product of the fully populated BEM matrices [3]. The algorithm is demonstrated for the  $\nu$ -th component of the matrix-vector product  $v_{\nu} = (\mathbf{V}\mathbf{u})_{\nu}$  of the single layer potential evaluated for constant shape functions. For convenience,  $\mu$  and  $\nu$  are used as indices for the element vectors as well as to denote the elements  $\mu$  and  $\nu$ , respectively. The nearfield part of the boundary integral operator is evaluated directly—i.e. the matrix entries are computed and stored when field and load point are close to each other—whereas for the farfield part, the multipole method is applied. The double surface integral is substituted by Gauss quadrature on the elements

$$\begin{aligned} v_{\nu} &= (\mathbf{V}_{\text{nearfield}}\mathbf{u})_{\nu} + \int_{\nu} \sum_{\mu \in \text{farfield}} u_{\mu} \int_{\mu} P^*(x, y) ds_y ds_x \\ &\approx (\mathbf{V}_{\text{nearfield}}\mathbf{u})_{\nu} + \sum_{j=1}^{G_{\nu}} \omega_{\nu,j} \Delta_{\nu} \sum_{\mu \in \text{farfield}} u_{\mu} \sum_{i=1}^{G_{\mu}} \omega_{\mu,i} \Delta_{\mu} P^*(x_{\nu,j}, y_{\mu,i}), \end{aligned} \quad (6)$$

where  $\Delta_{\mu}$ ,  $\omega_{\mu,i}$ , and  $y_{\mu,i}$  are the Jacobi determinant, Gauss weight, and integration point for element  $\mu$ , respectively. The terms are defined analogous for the element  $\nu$ . The expression

$$\Phi(x_{\nu,j}) = \sum_{\mu \in \text{farfield}} u_{\mu} \sum_{i=1}^{G_{\mu}} \omega_{\mu,i} \Delta_{\mu} P^*(x_{\nu,j}, y_{\mu,i}) \quad (7)$$

can be evaluated efficiently using the multipole method while the remaining operations in (6) are local at element  $\nu$ .

Using the fast multipole method, the numerical cost of the BEM is reduced from quadratic to quasi-linear in the number of boundary elements which allows the application of the BEM to large-scale models. The reduction is achieved by series expansion of the fundamental solution and a multilevel scheme. The appropriate theory of the multipole expansion for the Helmholtz operator and its diagonal translation operators is developed by

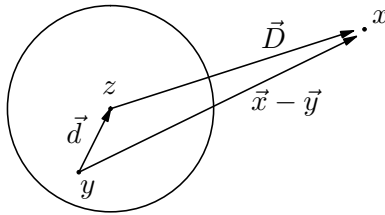


Figure 2: Definition of distance vectors for translation operators

Rokhlin. Following [6], the diagonal form of the multipole expansion of the fundamental solution around the center  $z$  as depicted in Fig. 2 reads

$$\frac{e^{i\kappa|\vec{D}+\vec{d}|}}{|\vec{D}+\vec{d}|} = \frac{i\kappa}{4\pi} \sum_{l=0}^{\infty} (2l+1) i^l h_l^{(1)}(\kappa|\vec{D}|) \int_{\mathbb{S}^2} e^{i\kappa\vec{d}\cdot\hat{s}} P_l(\hat{s}\cdot\hat{D}) ds, \quad |\vec{D}| > |\vec{d}|, \quad (8)$$

where  $\hat{s}$  represents the farfield directions on the unit sphere  $\mathbb{S}^2$ . Hankel functions and Legendre polynomials are denoted by  $h_l(\cdot)$  and  $P_l(\cdot)$ , respectively. Normalized vectors are indicated by  $\hat{(\cdot)} = (\cdot)/|\cdot|$ . The summation over  $l$  in (8) must be truncated, since the Hankel function diverges for large  $l$ . For the truncated series, summation and integration can be interchanged and one defines the translation operators

$$M_L(s, D) = \sum_{l=0}^L (2l+1) i^l h_l^{(1)}(\kappa|\vec{D}|) P_l(\hat{s}\cdot\hat{D}), \quad (9)$$

which solely depend on the distance vector  $\vec{D}$  and allow the implementation of an efficient multilevel scheme. The boundary elements of the triangulation are assigned to a cluster tree with levels  $\ell = 0 \dots \ell_{\max}$ . The cluster on the highest level  $\ell = 0$  represents a parallelepiped containing all boundary elements. Subsequent child clusters are constructed by bisection of the parent cluster. The clusters are denoted by  $C_\ell^\gamma$  where  $\gamma = 1 \dots 2^\ell$ . Two clusters on the same level are in each others nearfield when the distance  $D$  between their centers  $z_\ell^\gamma$  fulfills the condition

$$D < c \frac{d_\ell}{2}, \quad (10)$$

where  $d_\ell$  is the diameter of the clusters at level  $\ell$  and  $c$  is a suitable constant. Clusters, whose father clusters fulfill the nearfield condition, but themselves are not in each others nearfield, form the interaction list.

The multipole algorithm consists of the following steps:

- (i) Compute the farfield signature  $F_{\ell_{\max}}^\gamma(s)$  for all clusters on the lowest level  $\ell = \ell_{\max}$

$$F_{\ell_{\max}}^\gamma(s) = \sum_{\mu \in C_{\ell_{\max}}^\gamma} u_\mu \Delta_\mu \sum_{i=1}^{G_\mu} \omega_{\mu,i} e^{i\kappa(\vec{y}_{\mu,i} - \vec{z}_{\ell_{\max}}^\gamma) \cdot \hat{s}}. \quad (11)$$

- (ii) Translate  $F_\ell^\gamma(s)$  to the interaction list using the translation operators  $M_L$

$$N_\ell^\gamma(s) = \sum_{\text{interaction list}} M_L(s, D) F_\ell^\gamma(s), \quad (12)$$

where  $D$  is the distance between  $z_\ell^\gamma$  and the center of the respective interaction list cluster.

- (iii) Shift  $F_\ell^\gamma(s)$  to the center of the father cluster.  
 (iv) Repeat last two steps upwards until the interaction list is empty.  
 (v) In the downward pass, shift the nearfield signatures  $N_\ell^\gamma(s)$  in interaction lists to the child clusters.

(vi) On the lowest level, recover solution in integration points  $x_{\nu,j}$

$$\Phi(x_{\nu,j}) = \frac{i\kappa}{4\pi} \int_{\mathbb{S}^2} e^{i\kappa(\tilde{z}_{\ell_{\max}}^j - \tilde{x}_{\nu,j}) \cdot \tilde{s}} N_{\ell_{\max}}^\gamma(s) ds. \quad (13)$$

Finally, the matrix-vector product (6) is evaluated by summation of the element contributions  $\Phi(x_{\nu,j})$  and addition of the nearfield contribution which is calculated directly using the standard BEM.

### Mortar Coupling for Acoustic Fluid-Structure Interaction

Employing the pressure on the acoustic-structure interface as Lagrange multiplier, i.e.  $\lambda = p^{\text{int}} = f^f$ , one obtains the coupled system of equations [4]

$$\begin{pmatrix} \rho_f \omega^2 \mathbf{A} & \mathbf{0} & \mathbf{0} & \mathbf{0} & \mathbf{0} & -\mathbf{C}_{\text{FEM}} \\ \mathbf{0} & \mathbf{V}_{i,i} & \mathbf{V}_{i,D} & \frac{1}{2}\mathbf{I} - \mathbf{K}_{i,i} & -\mathbf{K}_{i,N} & -\mathbf{C}_{\text{BEM}} \\ \mathbf{0} & \mathbf{V}_{D,i} & \mathbf{V}_{D,D} & -\mathbf{K}_{D,i} & -\mathbf{K}_{D,N} & \mathbf{0} \\ \mathbf{0} & -\frac{1}{2}\mathbf{I}^T + \mathbf{K}_{i,i}^T & \mathbf{K}_{i,D}^T & \mathbf{D}_{i,i} & \mathbf{D}_{i,N} & \mathbf{0} \\ \mathbf{0} & \mathbf{K}_{i,N}^T & \mathbf{K}_{D,N}^T & \mathbf{D}_{N,i} & \mathbf{D}_{N,N} & \mathbf{0} \\ \mathbf{C}_{\text{FEM}}^T & \mathbf{C}_{\text{BEM}}^T & \mathbf{0} & \mathbf{0} & \mathbf{0} & \mathbf{0} \end{pmatrix} \begin{pmatrix} \mathbf{w} \\ \mathbf{q}^{\text{int}} \\ \tilde{\mathbf{q}} \\ \mathbf{p}^{\text{int}} \\ \tilde{\mathbf{p}} \\ \lambda \end{pmatrix} = \begin{pmatrix} \rho_f \omega^2 \int_{\Gamma^{\text{int}}} \varphi^w f^e ds_x \\ -\int_{\Gamma^{\text{int}}} \varphi^q (V\bar{q})(x) ds_x + \int_{\Gamma^{\text{int}}} \varphi^q \left( \frac{1}{2}\bar{p}(x) + (K\bar{p})(x) \right) ds_x \\ -\int_{\Gamma^D} \varphi^q (V\bar{q})(x) ds_x + \int_{\Gamma^D} \varphi^q \left( \frac{1}{2}\bar{p}(x) + (K\bar{p})(x) \right) ds_x \\ -\int_{\Gamma^{\text{int}}} \varphi^p (D\bar{p})(x) ds_x + \int_{\Gamma^{\text{int}}} \varphi^p \left( \frac{1}{2}\bar{q}(x) - (K'\bar{q})(x) \right) ds_x \\ -\int_{\Gamma^N} \varphi^p (D\bar{p})(x) ds_x + \int_{\Gamma^N} \varphi^p \left( \frac{1}{2}\bar{q}(x) - (K'\bar{q})(x) \right) ds_x \\ \mathbf{0} \end{pmatrix}, \quad (14)$$

where  $\mathbf{A}$  is the dynamic FEM stiffness matrix and  $\mathbf{V}$ ,  $\mathbf{K}$ , and  $\mathbf{D}$  are the BEM system matrices evaluated on the boundary sections corresponding to their subscripts.  $\mathbf{I}$  denotes a mass matrix on the boundary arising from the discretized identity operator. The coupling matrices  $\mathbf{C}_{\text{FEM}}$  and  $\mathbf{C}_{\text{BEM}}$  are defined by integration of the respective ansatz functions over the coupling interface

$$\mathbf{C}_{\text{FEM}} = \rho_f \omega^2 \int_{\Gamma^{\text{int}}} \varphi^w(x) \varphi^\lambda(x)^T ds_x, \quad \mathbf{C}_{\text{BEM}} = \int_{\Gamma^{\text{int}}} \varphi^q(x) \varphi^\lambda(x)^T ds_x. \quad (15)$$

Direct iterations on the system (14) converge very poorly, thus, an approximate Uzawa algorithm is employed. The system (14) is solved for  $\lambda$  and GMRES iterations are employed on the reduced equation

$$\begin{pmatrix} \mathbf{C}_{\text{FEM}}^T & \mathbf{C}_{\text{BEM}}^T \end{pmatrix} \begin{pmatrix} (\rho_f \omega^2 \mathbf{A})^{-1} & \mathbf{0} \\ \mathbf{0} & \mathbf{B}^{-1} \end{pmatrix} \begin{pmatrix} \mathbf{C}_{\text{FEM}} \\ \mathbf{C}_{\text{BEM}} \end{pmatrix} \lambda = \begin{pmatrix} \rho_f \omega^2 \mathbf{f}_{\text{FEM}} \\ \mathbf{f}_{\text{BEM}} \end{pmatrix}, \quad (16)$$

where the BEM matrix  $\mathbf{B}$  was introduced for simplification of notation. The matrix inverses in (16) are not evaluated explicitly, but are approximated by iterative schemes. For the BEM part, preconditioned GMRES iterations are employed [7]. The accuracy for the approximation of the inner systems is chosen to control the residual gap of the outer GMRES iterations according to the analysis by Simoncini and Szyld [8].

### Simulation of Hydro-Acoustic Experiments

A practical application of the mortar FEM-BEM coupling algorithm is the simulation of experiments on active structural-acoustic control in the hydro-acoustic lab at the Institut A für Mechanik [1]. For the chosen example, a rectangular plate ( $0.475 \text{ m} \times 0.48 \text{ m}$ ,  $t = 1.5 \text{ mm}$ ) is mounted on the box depicted in Fig. 3 and submerged in the water pool. Plate vibrations are excited by a shaker inside the box, and the acceleration on the plate as well as the acoustic pressure in the pool are recorded.

For the simulations, a BEM mesh of the pool and the box is set up that consists of 4726 triangular elements. The lower right hand corner of the plate is chosen as origin for the reference coordinate system. Homogeneous Dirichlet boundary conditions are applied on the pressure-free surface of the pool, whereas the pool walls are



Figure 3: Hydro-acoustic lab and submergeable box.

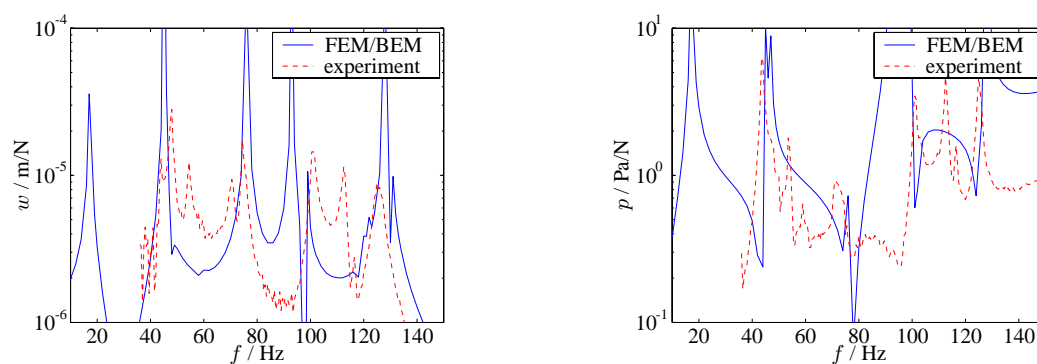


Figure 4: Experimental and computed frequency response.

modeled as rigid, i.e. homogeneous Neumann boundary conditions are applied. The plate is discretized using  $16 \times 16$  finite elements and is assumed to be clamped onto the rigid box.

In Fig. 4 the simulated and experimental frequency response functions for the plate displacement at position  $(0.42, 0.32)$  m and the acoustic pressure in the pool at position  $(0.15, -0.50, 0.51)$  m are plotted. The shaker is mounted at the position  $(0.20, 0.11)$  m on the plate and the forcing amplitude is used to normalize the plotted values. One notices that the principal behavior of simulation and experiment correlates. The differences can be traced back to various sources. The peaks in the experimental frequency response functions at 55 Hz, 71 Hz, and 113 Hz are due to resonance frequencies of the pool's front wall that is modeled as rigid in the FEM-BEM simulation. The influence of mounting the plate onto the box plays a dominant role as well: sealing material and fixing screws introduce a vast amount of model uncertainties. Finally, the acoustic boundary conditions of the pool walls must be determined in more detail. In this context, the simulation results are satisfying, however, more effort should be placed on the modeling of the system pool-box-plate.

#### References

- [1] O. Fein and L. Gaul. Reduction of sound emission from submerged structures using piezoelectric sensors and actuators. In *Proceedings of the 9th International Congress on Sound and Vibration*, pages 316–323, Orlando, FL, 2002.
- [2] M. Fischer. The Fast Multipole Boundary Element Method and its Application to Structure-Acoustic Field Interaction. PhD thesis, Institut A für Mechanik, Universität Stuttgart, 2004.
- [3] M. Fischer, U. Gauger, and L. Gaul. A multipole Galerkin boundary element method for acoustics. *Engineering Analysis with Boundary Elements*, 28(2):155–162, 2004.

- [4] M. Fischer and L. Gaul. Fast BEM-FEM mortar coupling for acoustic-structure interaction. *International Journal for Numerical Methods in Engineering*, accepted for publication, 2005.
- [5] L. Gaul, M. Kögl, and M. Wagner. *Boundary Element Methods for Engineers and Scientists*. Springer-Verlag, Berlin, 2003.
- [6] V. Rokhlin. Diagonal forms of translation operators for the Helmholtz equation in three dimensions. *Applied and Computational Harmonic Analysis*, 1:82–93, 1993.
- [7] Y. Saad. *Iterative Methods for Sparse Linear Systems*. SIAM, Philadelphia, PA, second edition, 2003.
- [8] V. Simoncini and D.B. Szyld. Theory of inexact Krylov subspace methods and applications to scientific computing. *SIAM Journal of Scientific Computing*, 25(2):454–477, 2003.

## Sound Pressure Reduction Provided by an Infinite Elastic Layer Containing Heterogeneities via BEM

Andreia Pereira<sup>1</sup>, António Tadeu<sup>1</sup>

<sup>1</sup> Department of Civil Engineering, University of Coimbra, Portugal,

[apereira@dec.uc.pt](mailto:apereira@dec.uc.pt), [tadeu@dec.uc.pt](mailto:tadeu@dec.uc.pt)

**Keywords:** Boundary Element Method; sound insulation; single layer; heterogeneity

**Abstract.** A Boundary Element Method (BEM), formulated in the frequency domain, is used to the study wave propagation across a single infinite elastic partition dividing an infinite acoustic medium. The influence of a heterogeneity in the elastic partition on the airborne sound insulation is studied using the solution of a single homogeneous elastic layer as a reference. In the BEM model, the discretization of the flat interfaces is avoided since Green's functions for the layered media. Thus, only the heterogeneity is discretized. In the simulations, the incident wave field is generated by cylindrical line loads placed in the acoustic medium and the heterogeneity is assumed to be an empty void (free boundary conditions). Material losses are simulated by using complex velocities. To better understand the acoustic phenomena involved, time domain responses are also discussed.

### Introduction

To accurately predict the acoustic performance of plate-like partitions, several variables have to be considered, such as the physical properties of the panel, the mounting conditions, the finiteness of the element and the non-diffusivity of the test room. Besides these variables, sound insulation may also be influenced by the presence of heterogeneities, which are often present inside partitions. These may refer to other building elements such as heating, sewerage, drainage or water pressure pipes. They are not taken into account at the design stage, and when the performance of walls is tested the results often fail to match the predictions. Therefore it is important to determine whether the presence of these elements can influence the sound insulation of partitions. In this work, a model using the Boundary Element Method (BEM) is developed to assess the acoustic behavior of single partitions (infinite along two directions dividing an infinite acoustic medium), in the presence of a heterogeneity inside the elastic medium. In this algorithm only the heterogeneity needs to be discretized as Green's functions are used for the single-layered medium. This heterogeneity is assumed to be free. The Green's functions' solutions are the same as those developed by Tadeu et al. [1]. This model is used to find frequency and time domain responses due to excitation by a cylindrical line load. The influence of heterogeneities inside the elastic partition is studied by determining airborne sound insulation. Results provided by a single homogeneous layer solution are used as a reference. Features of wave propagation occurring in a single-layered medium and of the scattered field produced by the heterogeneity in sound pressure level are investigated by analyzing the responses provided by different sets of receivers. Next, the problem formulation is briefly described and the procedure used to calculate time domain responses is summarized. Then the description of the simulations and the discussion of the results are presented.

### Problem Formulation

Consider an elastic layer of thickness  $h$  and infinite dimension along the  $x$  and  $z$  directions, dividing an infinite acoustic medium. The acoustic medium has a mass density  $\rho_f$  and a dilatational wave velocity  $\alpha_f$ . The elastic medium, which has a density  $\rho_s$ , allows a compressional wave velocity of  $\alpha_s$  and a shear wave velocity of  $\beta_s$ . The influence of a free heterogeneity in the elastic partition on the sound pressure level is studied by inserting a cylindrical circular inclusion with radius  $R$ , and infinite along the  $z$  direction, inside the elastic layer. The system is excited by cylindrical line loads that act in the acoustic medium at  $(x_0; y_0)$ , and the subsequent incident pressure field at a point  $(x; y)$  of the acoustic medium can be obtained as,

$$\hat{\sigma}^{full}(\omega, x, y, k_z) = \frac{-iA}{2} H_0^{(2)}\left(k_{\alpha_f} \sqrt{(x-x_0)^2 + (y-y_0)^2}\right) e^{-ik_z z}, \quad (1)$$

in which  $A$  is the wave amplitude,  $H_0^{(2)}(\dots)$  are second Hankel functions of order 0,  $k_{\alpha_f} = \sqrt{\omega^2/\alpha_f^2 - k_z^2}$  (with  $\text{Im}k_{\alpha_f} < 0$ ),  $k_z$  is the spatial wavenumber along the  $z$  direction, and  $\omega$  is the excitation frequency.  $k_z = 0$  corresponds to a cylindrical line load.

The two-dimensional scattered field due to the presence of the inclusion is computed using a Boundary Element model, where the discretization of the flat interfaces is avoided since Green's functions for single layered media are used. Thus, only the heterogeneity is discretized, and it is assumed to be free of stresses.

The Green's functions for the layered media used in the BEM model solutions are those derived previously by Tadeu et al. [1]. The technique employed for their derivation is based on the knowledge of the solid layer displacement potentials and the pressure potentials generated by the surfaces (surface terms), which are written as a superposition of plane waves. The two-dimensional field is then calculated by means of a discrete wavenumber representation (after applying a Fourier transform in the  $x$  direction). Details of the procedure can be found in Tadeu et al.[1].

As the formulation of the BEM used in wave propagation problems is widely known [2], the details are not given here. When a free inclusion is modelled, the Boundary Integral Equation is obtained by applying three virtual loads at the boundary in the elastic medium. Considering a virtual point load acting in the  $i$  direction at the point  $x_p$  of the boundary, and defining null stresses at the boundaries, the Boundary Integral equation may be written as:

$$u_i^{inc}(x_0, x_p) = \sum_{j=1}^3 \sum_{Q=1}^N u_j^Q(x_Q) \int_{S_Q} t_{i,j}^*(x_p, x_Q) dS_Q + C_{PQ} u_i(x_p). \quad (2)$$

In the system of equations,  $u_j^Q$  describes displacements at the discretized element  $Q$  in the direction  $j$ ;  $t_{i,j}^*(x_p, x_Q)$  is the Green's tensor for traction components in the single layered media, at the point  $x_Q$  in direction  $j$  caused by a concentrated load acting at the source point  $x_p$  in direction  $i$ ; the subscripts  $i, j=1, 2, 3$  denote the normal, and tangential directions relative to the boundary surface and  $z$  direction;  $c_{P,Q}$  is a constant that equals  $\delta_{PQ}/2$  for a smooth boundary, where the Kronecker delta is represented by  $\delta_{PQ}$ . By applying equation (2) for the three virtual loads at each boundary element a system of  $3 \times N$  equations is obtained where  $N$  is the total

number of boundary elements by which the boundary is discretized. The integrations needed for expression (2) are carried out using a Gaussian quadrature scheme. The BEM algorithm used in this work was implemented and validated by comparing the results with a BEM model where the discretization of the interfaces is required and Green's functions for a full space are used (not displayed). To ensure accurate results a large number of boundary elements was used to discretize the surfaces. Analysis of the results confirms excellent agreement between the two solutions. The internal material loss is also considered by using a complex Young's modulus and complex Lamé's constant. The Young's modulus is computed as  $E = E_r(1 + i\eta)$ , where  $E_r$  corresponds to the classic modulus and  $\eta$  is the loss factor. The complex Lamé's constant can be written in the same form as the Young's modulus.

**Responses in the time domain**

The BEM model described above allows responses to be obtained in the frequency domain. The pressure field in the spatial-temporal domain is obtained using a fast inverse Fourier transform in the frequency and wavenumber domain. The source used to calculate the temporal solution is modelled as a Ricker wavelet whose Fourier transform is

$$U(\omega) = A \left[ 2\sqrt{\pi}t_0 e^{-i\omega t_s} \right] \Omega^2 e^{-\Omega^2}, \tag{3}$$

in which  $\Omega = \omega t_0 / 2$ ;  $A$  is the amplitude;  $t$  denotes time;  $t_s$  is the time when the maximum occurs, and  $\pi t_0$  is the characteristic (dominant) period of the wavelet.

The Fourier transformations are obtained by discrete summations over wavenumbers and frequencies. Mathematically, this is achieved by adding periodic sources at spatial intervals  $L = 2\pi / \Delta k_x$  (in the  $x$  axis), and temporal intervals  $T = 2\pi / \Delta \omega$ , with  $\Delta k_x$ , and  $\Delta \omega$  being the wavenumber and frequency steps, respectively ([3]). The spatial separation,  $L$ , must be large enough to guarantee that the response of the fictitious sources occurs at times later than  $T$ , so that no contamination occurs. Complex frequencies, with a small imaginary part of the form,  $\omega_c = \omega - i\eta$  (with  $\eta = 0.7\Delta\omega$ ), can also be used to improve the accuracy of the response by introducing a significant attenuation, or virtual elimination, of the periodic sources.

**Applications**

The simulations studied refer to a single partition of thickness ,0.20m infinite along the  $x$  and  $z$  direction, and made of concrete ( $\alpha_s = 3498.6$  m/s;  $\beta_s = 2245.0$  m/s;  $\rho_s = 2500.0$  kg/m<sup>3</sup>;  $\eta_s = 4 \times 10^{-3}$ ), which divides an infinite acoustic medium (see Figure 1).

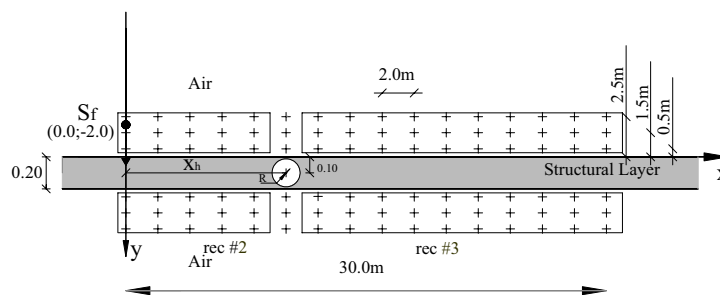


Figure 1 - Geometry of the simulations.

The acoustic medium is air ( $\rho_f = 1.22 \text{ kg/m}^3$  and  $\alpha_f = 340.0 \text{ m/s}$ ). The model is excited by sources placed in the acoustic medium ( $S_f$ ) at position  $(0.0\text{m}; -2.0\text{m})$ . The presence of a heterogeneity inside the single layer is considered by modelling a free circular inclusion of radius  $R = 0.075\text{m}$  placed at  $(10.0\text{m}; 0.10\text{m})$ .

The analysis is performed using a frequency range of  $[2.0; 8192.0\text{Hz}]$  with a frequency step of  $2.0 \text{ Hz}$ . Responses in the time domain are also plotted using a total time given by  $T = \frac{1}{2.0} = 100\text{ms}$ . The spatial distance between the virtual sources was set to  $5 \alpha_s T$ . The source used is a Ricker wavelet pulse with a characteristic frequency of  $2000\text{Hz}$ .

Responses are obtained in the frequency domain by calculating the sound pressure over a grid of receivers equally spaced at distances of  $2.0 \text{ m}$  along the  $x$  direction, as illustrated in Figure 1. The airborne sound insulation was calculated by noting the difference between the average sound pressure level in the medium containing the source (which recorded the incident and reflected pressure field) and that in the receiving medium on a dB scale. Calculations of the average sound insulation are performed considering different sets of receivers: all receivers (labelled in the plots as *rec#1*), receivers placed on the left side of the inclusion (labelled in the plots as *rec#2*) and receivers placed on the right side of the inclusion (labelled in the plots as *rec#3*), as in Figure 2.

The heterogeneity is modelled using constant boundary elements whose number varies with the excitation frequency. The size of each element is one tenth of the wavelength of the incident waves. The minimum number of boundary elements used was always greater than 30.

Figure 2 shows the airborne sound insulation provided by a single concrete structural layer in the presence of the free heterogeneity. Responses provided by the single layer are added as a reference. Figure 2a presents the responses obtained using the sets of receivers *rec#1* and *rec#2*, while Figure 2b plots the results provided using the sets of receivers *rec#1* and *rec#3*.

The curves of airborne sound insulation calculated considering receiver set *rec #1* show some (expected) acoustic features occurring in the single layered medium, and these will be briefly described [4]. Sound insulation increases as the frequency increases and the coincidence effect (labelled as *fc* in the plot) associated with the propagation of guided waves along structural layer is visible. The dip of insulation that is being formed at the end of the response is associated with resonances inside the panel. At higher frequencies the curve is less smooth owing to the interaction between the incident and directly-reflected wave fields, which occur when the difference in the travel paths is a multiple of the wavelength. When the heterogeneity is inserted inside the layer additional reflections occur and the resulting wave field is more complex. Comparison between the curves provided by the single layer and by the same layer with the heterogeneity inserted show that at low and medium frequencies they behave similarly. However at higher frequencies the sound insulation starts to be affected by the inclusion, and at specific frequencies small dips appear which are related to the interaction between pulses which reach the receivers with the same phase. These differences only appear at higher frequencies due to the size of the heterogeneity.

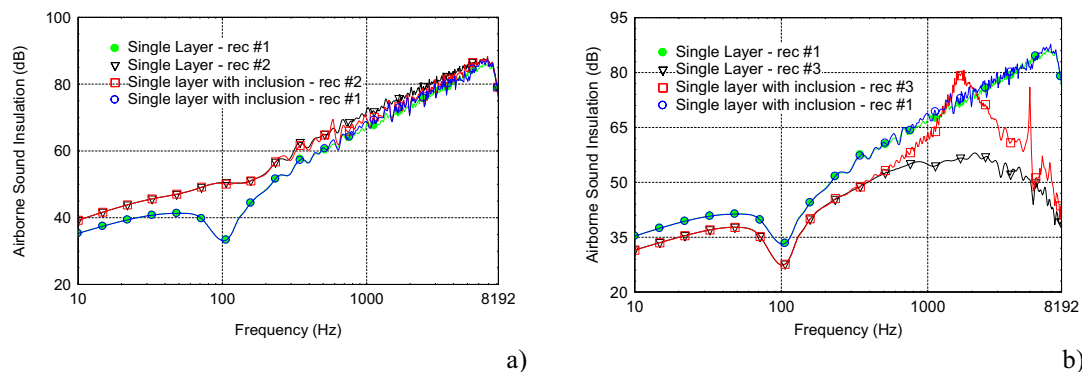


Figure 2 - Frequency domain responses when a cylindrical line source excites a concrete single layer in the presence of a free heterogeneity: a) *rec #1* vs *rec #2*; a) *rec#1* vs *rec #3*.

The average sound insulation curve achieved on the basis of the pressure, taking all receivers into account, does not allow a full description of the sound level in the vicinity of the heterogeneity (the final response is considerably influenced by the higher sound pressure levels, thus hiding wave propagation features occurring at other receivers). Therefore an analysis considering the average, using receiver sets *rec#2* and *rec#3* is performed to study wave propagation better. Figure 2a shows the responses provided by receiver set *rec#2*. Analysis shows that the sound insulation indicated by receiver set *rec#2* is higher than that calculated using all receivers (*rec#1*). This increase in insulation occurs mainly because the coincidence effect does not influence sound level at receivers placed near the source. Furthermore, the incident field is higher at these receivers. The sound insulation indicated by receiver set *rec#2* for the single partition and for the layer in the presence of the heterogeneity at the low and medium frequencies is also very similar. Differences occur at higher frequencies where the sound insulation produced by the layer containing the inclusion decreases and dips at specific frequencies are present (not clearly visible).

Analysis of sound insulation according to the set of receivers *rec#3* (see Figure 2b) shows that the solutions provided by the single layer and by the layer with the heterogeneity present major differences, at higher frequencies. These consist of an increase in sound insulation when the heterogeneity is present. At the end of the response the sound insulation tends to approach that provided by the single layer, due to higher frequency waves that can travel across the gaps between the inclusion and the layer in the elastic medium. Notice that the response calculated using receivers *rec#1* does not these wave propagation features to be observed.

In order to better illustrate the physical phenomena described above, time domain responses were computed for a set of receivers placed 0.50 m away from the layer's surface, in the receiving medium, and these are illustrated in Figure 3. Figure 3a shows the results obtained for the single concrete layer. Figure 3b plots the responses provided by single layer in the presence of the free heterogeneity.

Analysis of Figure 3a reveals a set of pulses which reach the receivers of the single concrete layer model. These are produced by refractions and mode conversions at the layer's surfaces. The first pulses recorded correspond to the refracted dilatational wave pulse (travelling with the compression wave velocity of the concrete and labelled as P in the plot) and to the refracted shear elastic wave pulse (travelling with the shear wave velocity of the concrete and labelled as S in the plot). These are followed by set of dispersive pulses originated in the guided waves that travel along the surfaces at different velocities. The first pack of pulses arriving after the S wave are high frequency waves, and these are followed by successive lower frequency

pulses up to the arrival of the dilatational wave in the fluid, the slowest one (labelled in the plot as  $P_f$ ). When the free heterogeneity is inserted into the single concrete layer, the corresponding plot (see Figure 3b) shows a set of additional high frequency pulses recorded at receivers placed on the left side of the inclusion, and related to reflections produced by the inclusion. At receivers placed on the right side of the inclusion a decrease in the amplitude of higher frequency pulses is recorded. Low frequency waves travel along the layer without being influenced by the presence of the inclusion. These features are in accordance with the frequency domain analysis.

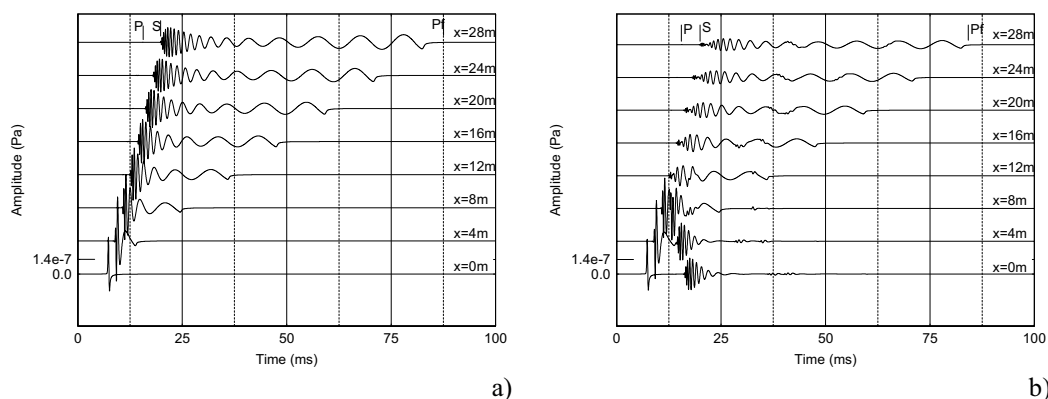


Figure 3 - Time domain responses recorded in the receiving medium for a characteristic frequency of 2000 Hz : a) Single layer model; b) Single layer in the presence of the free heterogeneity.

### Summary

This paper describes a BEM model that is developed and applied to determine the level of airborne sound insulation provided by a single layer which contains a free heterogeneity. Frequency and time domain analysis show that at low and medium frequencies airborne sound insulation is not influenced by the presence of the heterogeneity. For higher frequencies sound insulation decreases at receivers placed on the left side of the inclusion, due to the additional scattered field generated by the inclusion. At receivers placed on the right side of the inclusion an increase in sound insulation is found to occur at a range of higher frequencies. After these, at the end of the analyzed response, the sound insulation tends to approach that provided by the single layer, and this is due to higher frequency waves that can travel in the elastic medium, across the gaps between the inclusion and the layer.

### References

- [1] A. Tadeu and J. António, 2.5D Green functions for elastodynamic problems in layered acoustic and elastic formations. *Journal of Computer Modeling in Engineering and Sciences CMES*, **2**, 477-495 (2002).
- [2] G. Manolis and D. Beskos, *Boundary Element Methods in Elastodynamics*. London: Unwin Hyman (sold to Chapman and Hall) (1988).
- [3] M. Bouchon, K. Aki, Time-domain transient elastodynamic analysis of 3D solid elastic medium, *International Journal of Numerical Methods in Engineering*, **26**, 1709-1728 (1977).
- [4] A. Tadeu, J. António, Acoustic insulation of a single panel walls provided by analytical expressions versus the mass law, *Journal of Sound and Vibration*, **257**(3), 457-475 (2002).

## Boundary Element Acoustic Analysis of Perforated Absorptive Silencers

Zhenlin Ji, Tianyuan Zhang

School of Power Engineering, Harbin Engineering University

Harbin, Heilongjiang 150001, P. R. China

Email: [zhenlinji@yahoo.com](mailto:zhenlinji@yahoo.com)

**Keywords:** Silencer, Sound-absorbing Material, Perforated Screen, Acoustic Attenuation Performance, Boundary Element Analysis.

**Abstract.** A substructure boundary element approach is developed to predict and analyze the acoustic attenuation performance of perforated absorptive silencers. The silencer is divided into a number of acoustic domains with single medium (air or sound absorbing material), and treating the sound absorbing material as an equivalent fluid with complex dynamic density and speed of sound, and then the boundary element method may be applied to each domain leading to a system of equations in terms of sound pressure and particle velocity. Using the perforate impedance boundary conditions, the relationship of acoustic pressures and particle velocities between the inlet and outlet can be obtained and then transmission loss of the silencer can be determined. For a straight-through perforated tube absorptive silencer, the predictions of transmission loss agree reasonably well with experimental results. BEM is then used to investigate the effects of flow-resistivity (or bulk density of sound-absorbing material), porosity of perforation, thickness of sound-absorbing material, as well as the lined inlet/outlet end-plates and chamber on the acoustic attenuation performance of the silencers.

### Introduction

The sound-absorbing materials are widely used to improve the acoustic attenuation performance of silencers at higher frequencies. Craggs [1] applied the finite element method to model the dissipative mufflers with a locally reactive lining, and illustrated that the sound-absorbing materials improve the acoustic attenuation at higher frequencies and changed the transmission loss curve shapes. Astley and Cumming [2] employed the finite element method to investigate the acoustic attenuation in ducts lined with porous materials. Seybert *et al* [3] applied the boundary element method to predict the sound propagation in ducts containing bulk absorbing materials. However, the above studies excluded the presence of perforated tube or screen. Sound-absorbing materials are typically used in combination with perforated tube or screen, resulting in an interaction between them. An accurate approach should consider the interaction between the perforated screen and sound-absorbing materials. Recently, Selamet *et al* [4] developed the one-dimensional analytical approach and three-dimensional boundary element method to predict the acoustic attenuation performance of straight-through perforated tube absorbing silencers. They modified the empirical expression of perforation impedance developed originally by Sullivan and Crocker [5] for perforations in the absence of sound absorbing materials, and extended to the perforations facing sound-absorbing material, in view of the work by Kirby and Cummings [6]. Their studies demonstrated that the three-dimensional approach is needed for accurate prediction of acoustic attenuation performance at higher frequencies, while the one-dimensional analytical approach provides a reasonable accuracy at lower frequencies only.

The present study employs the BEM to determine the transmission loss of the perforated absorptive silencers and to investigate the effects of flow-resistivity of sound absorbing material, porosity of perforation, thickness of sound absorbing material as well as lined end-plates and chamber on the acoustic attenuation performance of the silencers.

### Boundary Element Approach

The silencer configurations considered in the present study are shown in Figure 1. There are two media inside the silencer: the air and sound absorbing material. Assuming homogeneous sound absorbing material and harmonic wave propagation in both media, and treating the sound absorbing material as an equivalent fluid with complex dynamic density and speed of sound, the continuity and momentum equations yield [3,4]

$$\nabla^2 p + k^2 p = 0, \quad (1)$$

where  $p$  is the acoustic pressure,  $k$  is the wavenumber and equals to  $k_0$  for the air and  $\tilde{k}$  for the sound absorbing material, respectively.

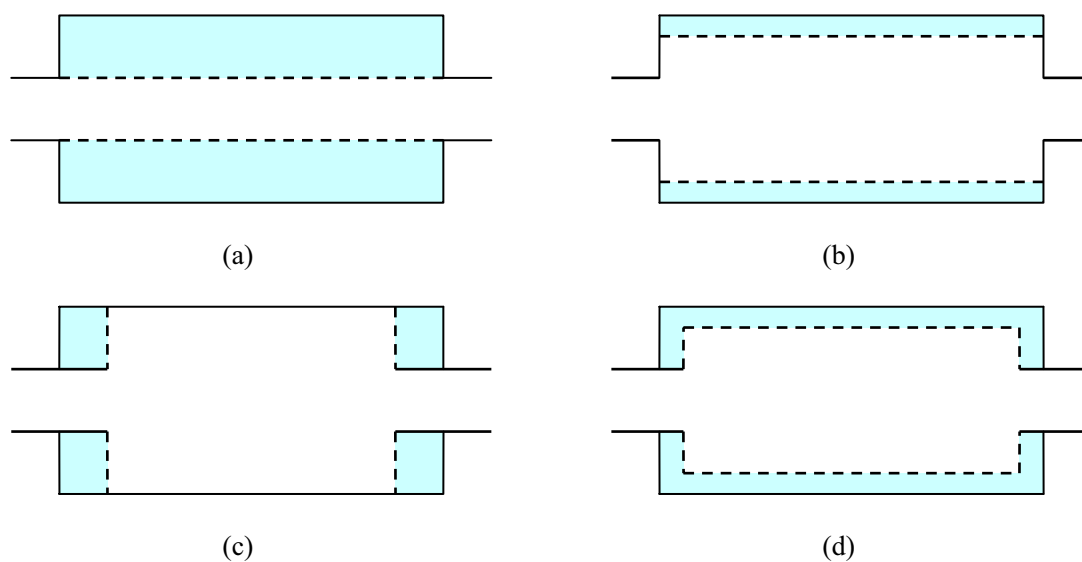


Figure 1. Perforated absorptive silencer configurations

Equation (1) may be represented in the form of the boundary integral expression [7] as

$$C(X)p(X) = - \int_{\Gamma} \left[ jkz\nu(Y)G(X,Y) + p(Y) \frac{\partial G}{\partial n}(X,Y) \right] d\Gamma(Y), \quad (2)$$

where  $\Gamma$  is the boundary surface of the acoustic domain,  $n$  is the unit normal vector on  $\Gamma$  directed away from the domain,  $j$  is the imaginary unit,  $z$  is the characteristic impedance of the medium,  $\nu$  is the outward normal particle velocity, and  $G(X,Y) = \exp(-jkR)/4\pi R$  is the Green's function of free space,  $R$  being the distance between any two points  $X$  and  $Y$  in the domain or on the surface, and  $C(X)$  is a coefficient which depends on the position of point  $X$ .

Numerical solution of the boundary integral equation (2) can be achieved by discretizing the boundary surface of the domain into a number of elements, and then a set of algebraic system of equations may be obtained by using numerical integration, which can be written in matrix form as

$$[H]\{P\} = z[G]\{V\}, \quad (3)$$

where  $[H]$  and  $[G]$  are the coefficient matrices, and  $\{P\}$  and  $\{V\}$  are the vectors whose elements are the sound pressure  $p$  and outward normal particle velocity  $\nu$  on the boundary nodes, respectively. The detailed treatment of the BEM numerical solution procedure is provided elsewhere [7].

To employ the BEM for the prediction of acoustic attenuation performance of the perforated absorptive silencers, a multi-domain approach is needed. The silencer is divided into a number of substructures and then

the BEM is applied to each one of these substructures leading to a system of equations. Continuity of sound pressure and normal particle velocity is then enforced at the interface between any two neighboring substructures. At the perforation, the specific acoustic impedance  $\zeta_p$  is introduced and the boundary conditions may be expressed as

$$v_p^a = -v_p^m, \quad \text{and} \quad p_p^a - p_p^m = z_0 \zeta_p v_p^a, \quad (4, 5)$$

where the superscripts  $a$  and  $m$  represent the air and sound-absorbing material, respectively,  $z_0$  is the characteristic impedance of the air. Using the perforate impedance boundary conditions, the relationship of acoustic pressures and particle velocities between the inlet and outlet can be obtained and then transmission loss of the silencer can be determined. Detailed descriptions of the multi-domain BEM approach for silencer analysis can be found elsewhere [7,8].

### Acoustic Properties of Sound Absorbing Material and Perforates

The present study uses texturized fiberglass roving as the sound absorbing material. The complex acoustic impedance  $\tilde{z}$  and the complex wavenumber  $\tilde{k}$  of the sound absorbing material can be calculated by the following expressions [4]

$$\tilde{z}/z_0 = 1.0 + 0.0954(\rho_0 f/\sigma)^{-0.754} - j0.085(\rho_0 f/\sigma)^{-0.732}, \quad (6)$$

$$\tilde{k}/k_0 = 1.0 + 0.160(\rho_0 f/\sigma)^{-0.577} - j0.189(\rho_0 f/\sigma)^{-0.595}, \quad (7)$$

where  $\rho_0$  is the density of air,  $f$  is the frequency and  $\sigma$  is the flow-resistivity of the material in MKS Rayls/m.

For perforations facing sound absorbing material, Selamet *et al* [4] modified the empirical expression presented by Sullivan and Crocker [5] in view of the work by Kirby and Cummings [6] as

$$\zeta_p = \left[ 0.006 + jk_0 \left\{ t + 0.375d_h \left( 1 + \tilde{z}\tilde{k}/z_0k_0 \right) \right\} \right] / \phi, \quad (8)$$

where  $t$  is the perforated tube or screen wall thickness,  $d_h$  the perforate diameter, and  $\phi$  the porosity of perforation.

### Results and Discussion

For all configurations, the present study considers  $D = 16.44 \text{ cm}$  and  $L = 25.72 \text{ cm}$  for the silencer inner diameter and length, respectively,  $d = 4.90 \text{ cm}$  for the inlet and outlet tube inner diameter,  $t = 0.09 \text{ cm}$  for the perforated tube or screen wall thickness,  $d_h = 0.249 \text{ cm}$  for the hole diameter, and speed of sound in the air is  $c_0 = 344.3 \text{ m/s}$ .

Figure 2 compares the transmission loss predictions and experimental results of straight-through perforated tube silencer (Figure 1a) with 8% porosity for three different filling densities 0, 100 and 200 g/l corresponding to the flow-resistivities 0, 4896 and 17378 MKS Rayls/m, respectively [4]. The BEM predictions show a reasonable agreement with experiments in the entire frequency range of interest. The absorptive silencers improve significantly acoustic attenuation performance compared to the silencer with no filling above 300 Hz. The silencer with no filling has several attenuation domes up to 2000 Hz, resembling the behavior of expansion chamber. The placement of sound absorbing material in the silencer changes the acoustic behavior of the silencer drastically by switching to a single broad peak. Increasing the density of sound absorbing material increases the peak transmission and shifts its location to lower frequency.

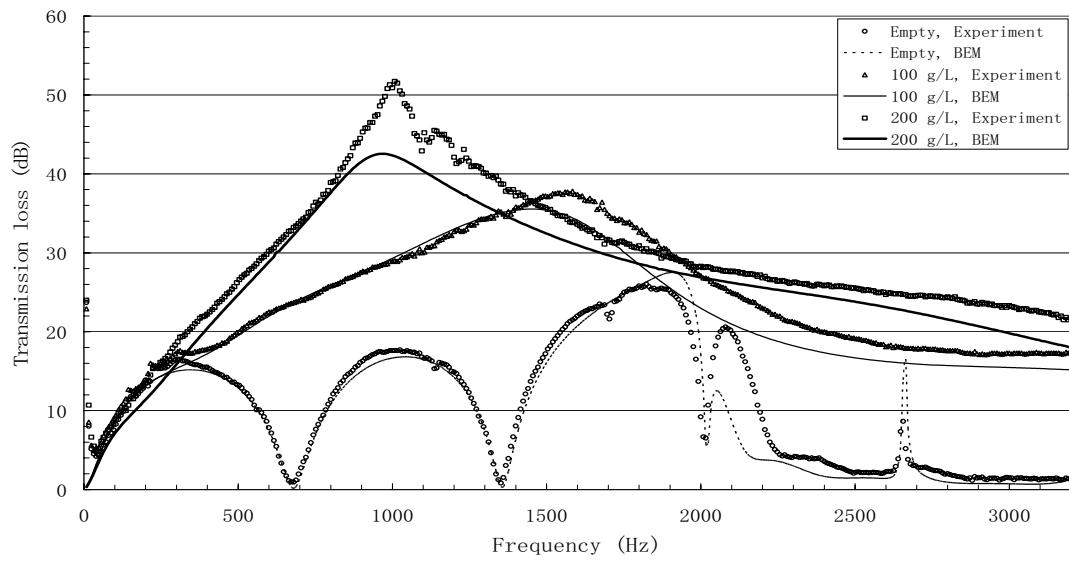


Figure 2. Transmission loss comparison of straight-through perforated tube silencer

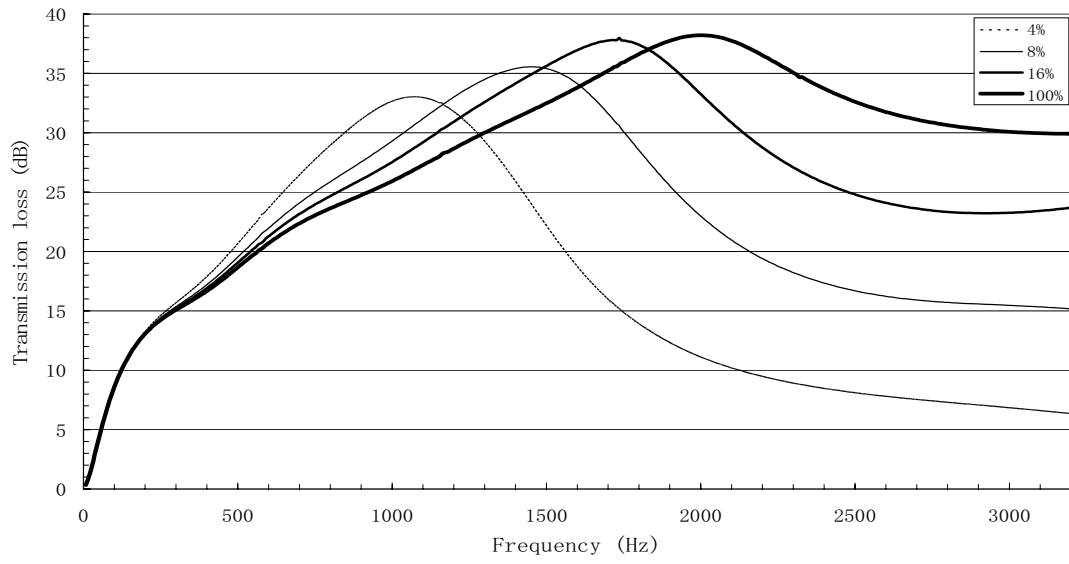


Figure 3. Effect of the porosity on transmission loss of straight-through perforated tube silencer

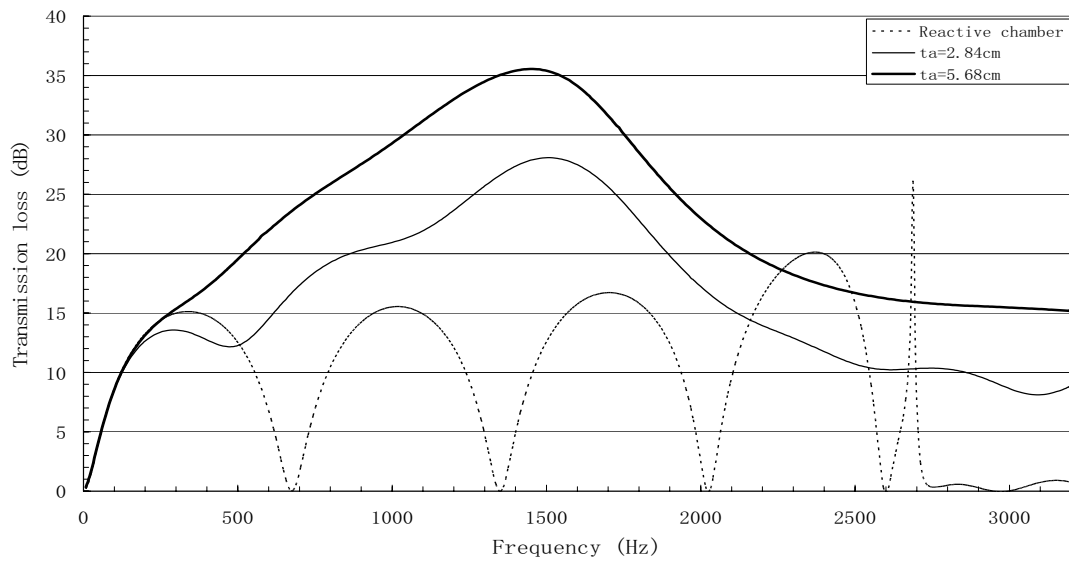


Figure 4. Effect of the lined shell on transmission loss of expansion chamber

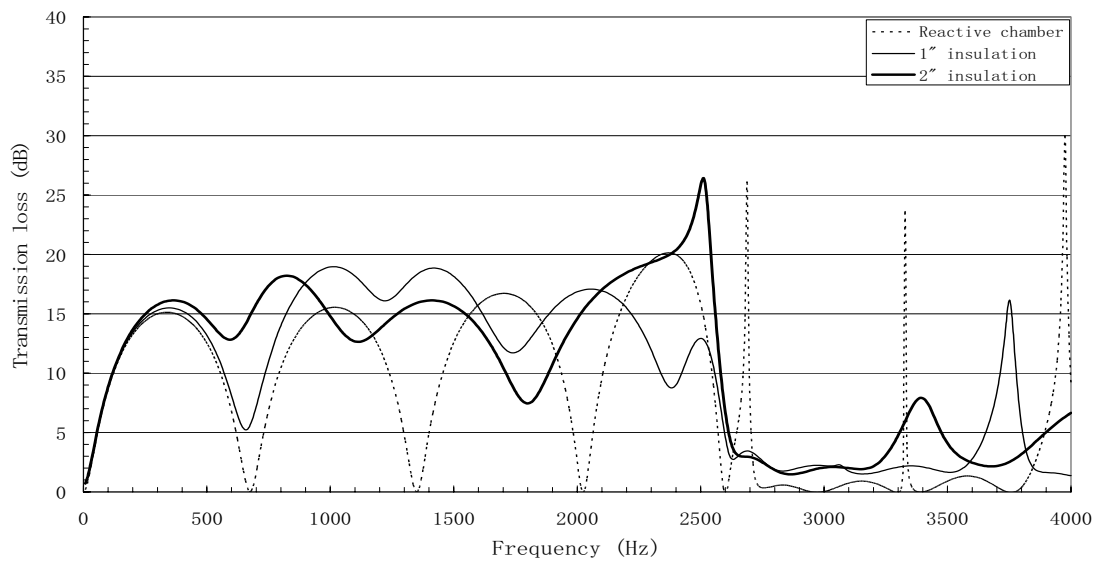


Figure 5. Effect of the lined inlet plate on transmission loss of expansion chamber

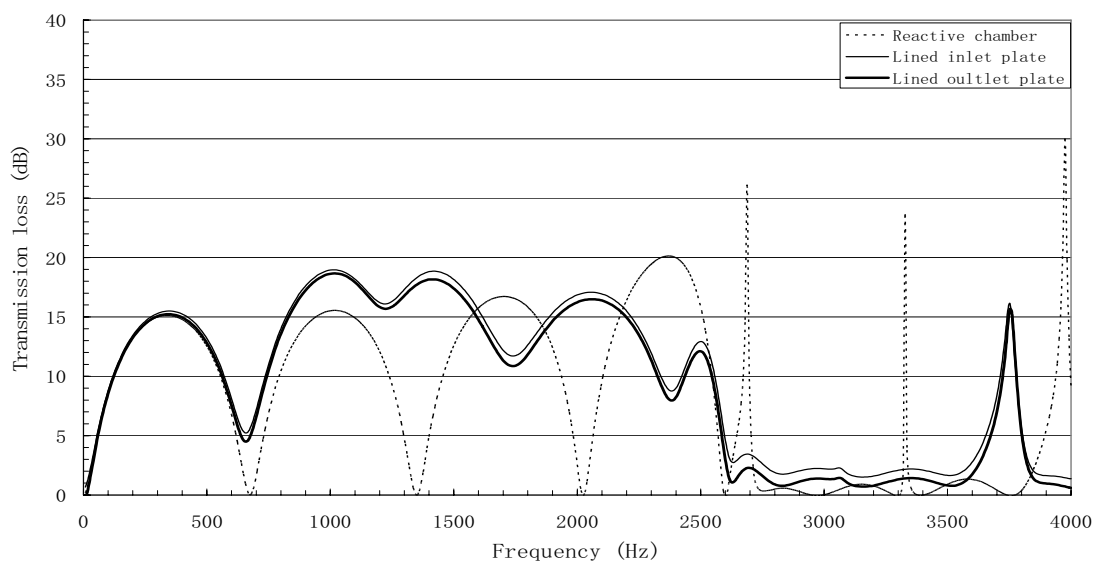


Figure 6. Effect of the lined end-plate on transmission loss of expansion chamber

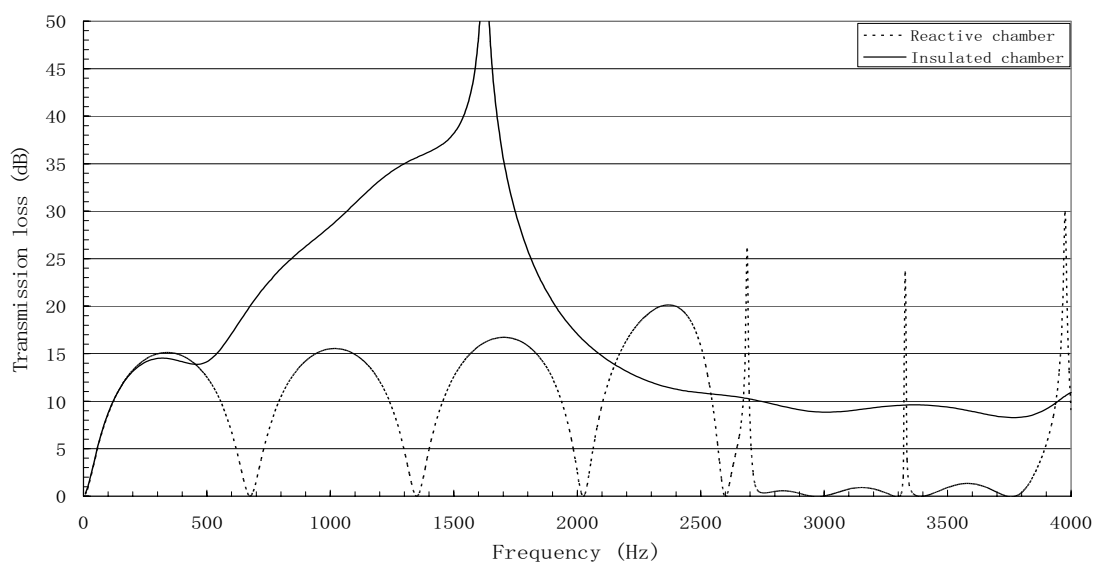


Figure 7. Effect of the full-lined chamber on transmission loss of expansion chamber

Transmission loss predictions of silencers with the filling density 100g/l for three different perforation porosities ( $\phi=4\%$ , 8%, and 16%) are presented in Figure 3, including the limiting case of removed screen ( $\phi=100\%$ ). At relatively high frequencies, the acoustic attenuation is significantly improved with porosity increasing, and the peak is shifted to higher frequencies. Higher perforations, however, tend to yield somewhat lower transmission loss at low frequencies.

The effects of lined chamber-shell and end-plates are examined next. The perforation porosity 8% and filling density 100g/l are chosen as default hereafter in this paper. Numerical results with varying thickness of sound absorbing materials (see configuration 1b) are depicted in Figure 4. Increasing the thickness of sound absorbing material improves the acoustic attenuation particularly at mid to high frequencies. Figures 5 and 6 demonstrated that the lined end-plate (see configuration 1c) improves the acoustic attenuation at most frequencies and lifts the troughs in transmission loss curve of reactive chamber. Increasing the insulation thickness improves the lower frequency attenuation, especially at the first trough. The lined outlet end-plate reveals the similar behavior to the lined inlet end-plate. Figure 7 compared the transmission loss of full lined chamber (see configuration 1d) with 1" thickness insulation and simple expansion chamber with the same diameter and length. Similarly, the full lined chamber improves the acoustic attenuation performance at most frequencies.

### Conclusions

The acoustic attenuation performance of perforated absorptive silencers is investigated numerically. For a straight-through perforated tube silencer, the BEM predictions show good agreement with experimental results. BEM is then used to investigate the effects of flow-resistivity of sound absorbing material, porosity of perforation, thickness of sound absorbing material as well as lined end-plates and chamber-shell on the acoustic attenuation performance of the silencers. In general, the absorbing material enhances the noise reduction of the silencer at mid to high frequencies. Increasing the porosity of perforation improves the high frequency acoustic attenuation performance. The lined end-plates and shell improve the acoustic attenuation at most frequencies, especially lift the troughs in transmission loss of reactive silencers.

### References

1. A. Craggs, "A finite element method for modeling dissipative mufflers with a locally reactive lining", *J. Sound Vib.* 54, 285-296 (1977)
2. R. J. Astley and A. Cummings, "A finite element scheme for attenuation in ducts lined with porous materials: Comparison with experiment", *J. Sound Vib.* 116, 239-263 (1987)
3. A. F. Seybert, R. A. Seman and M. D. Lattuca, "Boundary element prediction of sound propagation in ducts containing bulk absorbing materials", *J. Vib. Acous.* 120, 976-981 (1998)
4. A. Selamet, I. J. Lee, Z. L. Ji and T. Huff, "Acoustic attenuation performance of perforated absorbing silencers", *SAE Paper 2001-01-1435*, Michigan, USA (2001).
5. J. W. Sullivan and M. J. Crocker, "Analysis of concentric tube resonators having unpartitioned cavities", *J. Acoust. Soc. Am.* 64, 207-215 (1978)
6. R. Kirby and A. Cummings, "The impedance of perforated plates subjected to grazing gas flow and backed by porous media", *J. Sound Vib.* 217, 619-636 (1998)
7. Z. L. Ji, Q. Ma and Z. H. Zhang, "Application of the boundary element method to predicting acoustic performance of expansion chamber mufflers with mean flow", *J. Sound Vib.* 173, 57-71 (1994)
8. Z. L. Ji and A. Selamet, "Boundary element analysis of three-pass perforated duct mufflers", *Noise Control Eng. J.* 48, 151-156 (2000).

## Dual Reciprocity BEM for the Transient Nonlinear Heat Conduction Problem via Time-Stepping Scheme

Masataka Tanaka<sup>1</sup>, Toshiro Matsumoto<sup>2</sup> and Susumu Takakuwa<sup>3</sup>

<sup>1</sup>Department of Mechanical Systems Engineering, Shinshu University, Nagano, 380-8553 Japan  
E-mail: dtanaka@gipwc.shinshu-u.ac.jp

<sup>2</sup>Department of Mechanical Science and Engineering, Nagoya University, Nagoya, 464-8603 Japan

<sup>3</sup>Fuji Heavy Industries, Ltd.

**Keywords:** Computational Mechanics, Time-Stepping Boundary Element Method, Dual Reciprocity Method, Transient Heat Conduction, Temperature-Dependent Material

**Abstract.** This paper presents a dual reciprocity boundary element method (DRBEM) applied to the transient heat conduction problem in temperature dependent materials. The integral equation formulation employs the fundamental solution of the Laplace equation for homogeneous materials, and hence a domain integral arises in the boundary integral equation. This domain integral is transformed into boundary integrals by using a radial basis function. The domain integral corresponding to the so-called “pseudo” initial condition at each time step is also transformed into boundary integrals via the same dual reciprocity method. The usefulness of the present DRBEM is demonstrated through numerical computation.

### Introduction

This paper is concerned with a dual reciprocity boundary element method (DRBEM) [1, 2, 3, 4] for solving the transient heat conduction problems in homogeneous media. The time-stepping scheme is employed to approximate time derivative in the governing equation. The reduced differential equation thus obtained is transformed into the boundary integral equation in the usual manner using the fundamental solution of Laplace equation. The resulting boundary integral equation includes domain integrals related to the “pseudo” initial condition.

In the authors' previous papers [5, 6], these domain integrals are evaluated by introducing a cell division of the domain. The present paper aims at a more effective solution procedure based on dual reciprocity method. At this end, the dual reciprocity method can be applied to transforming the domain integrals into boundary integrals. The authors have reported successful applications of DRM to

the steady-state heat conduction problems [7]. The idea of DRM could also be successfully applied to the present time-dependent problems.

The present paper describes in detail how to apply the DRM to the solution of the boundary integral equation including domain integrals related to the pseudo initial condition. Numerical computation is carried out to demonstrate the usefulness and versatility of the proposed method of solution.

## Theory

**Governing Equation.** The present paper is concerned with the unsteady-state heat conduction problem in nonlinear materials which are dependent on the temperature. Under the assumption of no heat source in the domain, the governing differential equation can be expressed by

$$\nabla\{\lambda(u)\nabla u(x,t)\} = \rho c \dot{u}(x,t) \quad (1)$$

where  $u(x,t)$  is the temperature,  $\lambda(u)$  the heat conductivity coefficient which varies depending on the temperature,  $\rho$  the density of mass, and  $c$  the specific heat. In addition,  $\nabla$  is the gradient operator and the dot ( $\cdot$ ) denotes the time derivative.

It is assumed that the governing differential equation (1) is subject to the following boundary and initial condition:

$$\begin{aligned} u(x,t) &= \bar{u}, & x \in \Gamma_u \\ q(x,t) &= \frac{\partial u(x,t)}{\partial n} = \bar{q}, & x \in \Gamma_q \\ \lambda(u) \frac{\partial u(x,t)}{\partial n} + h\{u(x,t) - u_a\} &= 0, & x \in \Gamma_a \\ u(x,0) &= u_0, \end{aligned} \quad (2)$$

where  $n$  is the outward unit normal to the boundary  $\Gamma$  and  $\partial u(x,t)/\partial n$  denotes the normal derivative of  $u(x,t)$ . The boundary portions in which the temperature, heat flux and heat transfer condition are given are denoted by  $\Gamma_u$ ,  $\Gamma_q$  and  $\Gamma_a$ , respectively. Furthermore,  $\bar{u}$  and  $\bar{q}$  are the prescribed temperature and the heat flux, respectively, whereas  $h$  is the heat transfer coefficient,  $u_a$  the ambient temperature, and  $u_0$  the initial temperature.

The governing differential equation (1) can be rewritten as follows:

$$\nabla^2 u(x,t) = \frac{-1}{\lambda(u)} \left\{ \nabla \lambda(u) \nabla u(x,t) - \rho c \dot{u}(x,t) \right\} \quad (3)$$

**Application of Dual Reciprocity Method.** The fundamental solution of the Laplace equation is applied to the integral equation formulation of the problem, and then the boundary integral equation is obtained. This boundary integral equation includes not only the boundary integrals, but also domain integrals. To solve

such a boundary integral equation, the boundary-domain element method[8] has been proposed, in which the boundary is discretized into boundary elements and the domain into finite elements. It is true, however, that the method is robust, but the main advantage of BEM, the “boundary-only solution”, is missed. In this paper, the dual reciprocity method in terms of the radial basis function is used as a “meshless” approach to evaluate the domain integrals.

First, the right-hand side of Eq.(3) is approximated as follows:

$$\frac{-1}{\lambda(u)} \left\{ \nabla \lambda(u) \nabla u(x, t) - \rho c \dot{u}(x, t) \right\} = \sum_{\ell=1}^{N+L} \alpha^\ell f(x, z^\ell) \quad (4)$$

where  $N$  is the number of nodes on the boundary,  $L$  the number of collocation points in the domain,  $\alpha^\ell$  the unknown coefficients,  $f(x, z^\ell)$  the approximate radial-basis function, and  $z^\ell$  a collocation point.

Now, we introduce a particular solution which satisfies the following differential equation:

$$\nabla^2 \hat{u}(x, z^\ell) = f(x, z^\ell) \quad (5)$$

Using this particular solution  $\hat{u}(x, z^\ell)$ , we can express the governing differential equation (3) in terms of unknown coefficient  $\alpha^\ell$ . Finally, the boundary integral equation can be expressed as follows:

$$\begin{aligned} & c(y)u(y, t) + \int_{\Gamma} q^*(x, y)u(x, t)d\Gamma - \int_{\Gamma} u^*(x, y)q(x, t)d\Gamma \\ & = \sum_{\ell=1}^{N+L} \alpha^\ell \left\{ c(y)\hat{u}(y, t) + \int_{\Gamma} q^*(x, y)\hat{u}(x, z^\ell)d\Gamma - \int_{\Gamma} u^*(x, y)\hat{q}(x, z^\ell)d\Gamma \right\} \end{aligned} \quad (6)$$

where  $\hat{q}(x, z^\ell)$  is the normal derivative of the particular solution  $\hat{u}(x, z^\ell)$ . It is interesting to note that the right-hand side of Eq.(6) includes only the boundary integrals with  $N + L$  unknown coefficients  $\alpha^\ell$ . In the integral equation (6), we place the source point  $y$  at each node on the boundary and also at each collocation point in the domain  $\Omega$ . Then, we can have the system of  $N + L$  equations, which can be expressed as

$$\mathbf{H}\mathbf{u} - \mathbf{G}\mathbf{q} = [\mathbf{H}\hat{\mathbf{U}} - \mathbf{G}\hat{\mathbf{Q}}]\boldsymbol{\alpha} \quad (7)$$

The radial basis functions to be used in the DRM are available in the literature[1][2]. In this study, we shall employ the following function:

$$f(x, z^\ell) = \begin{cases} (1 - r^\ell/a)^4(4r^\ell/a + 1), & 0 \leq r^\ell \leq a \\ 0, & r^\ell \geq a \end{cases} \quad (8)$$

**Unknown Coefficients.** The unknown coefficients  $\alpha^\ell$  in Eq.(4) can be determined if Eq.(4) holds at each collocation point in the domain and on the boundary. They are expressed in the following matrix form:

$$\boldsymbol{\alpha} = \mathbf{F}^{-1}[\mathbf{K}_1\mathbf{u}_{x_1} + \mathbf{K}_2\mathbf{u}_{x_2} + \mathbf{K}_3\mathbf{u}_{x_3} - \mathbf{K}_t\dot{\mathbf{u}}] \quad (9)$$

For the time derivative of temperature we apply the time-stepping scheme: For the first time step from the initial state we use a backward finite difference based on linear approximation; For the subsequent time steps we use another backward finite difference of quadratic variation in time. The variables at one- and two-previous time steps are treated as the ‘‘pseudo initial condition’’.

We can finally express the discretized set of equations in the following matrix form:

$$\mathbf{H}\mathbf{u} - \mathbf{G}\mathbf{q} = [\mathbf{H}\hat{\mathbf{U}} - \mathbf{G}\hat{\mathbf{Q}}][\mathbf{R}\mathbf{u} - \mathbf{T}_0] \quad (10)$$

where

$$\mathbf{R} = \mathbf{F}^{-1} \left[ \left\{ (\mathbf{K}_1\mathbf{F}_{x_1} + \mathbf{K}_2\mathbf{F}_{x_2} + \mathbf{K}_3\mathbf{F}_{x_3})\mathbf{F}^{-1} - \mathbf{K}_p \right\} \right] \quad (11)$$

$$\mathbf{T}_0 = \mathbf{F}^{-1}\mathbf{t}_0 \quad (12)$$

Since  $\mathbf{R}$  and  $\mathbf{T}_0$  include the unknown temperature, the above set of equations are nonlinear, and hence we shall use an iterative solution procedure. First, we assume the one-step previous temperature for calculation of  $\mathbf{R}$  and  $\mathbf{T}_0$ . Then, Eq.(10) is solved to update the temperature. The temperature thus obtained is assumed for the next iteration. The process of the above computation is repeated until convergence is realized.

## Numerical Results and Discussion

We now show numerical results of some examples to demonstrate the validity of the present solution procedure.

Numerical computation is carried out for the parallelepiped shown in Fig. 1. The boundary is divided into rectangular boundary element with quadratic interpolations, and the total numbers of boundary elements and nodes are 40 and 122, respectively. The collocation points in the inner domain are located uniformly: 7 points in the axis  $x_1$  and 3 points in the axes of  $x_2$  and  $x_3$ .

The boundary conditions are assumed as follows: The planes perpendicular to the axis  $x_1$  are subject to a heat transfer condition with the heat transfer coefficient 2000 [W/m<sup>2</sup>K] where the ambient temperature is 500 [°C]. The other planes are subject to the adiabatic condition 0 [W/m<sup>2</sup>].

It is assumed that at the initial state the temperature is uniformly 100 [°C]. Furthermore, we assume that the density of mass is 7800 [kg/m<sup>3</sup>] and the specific

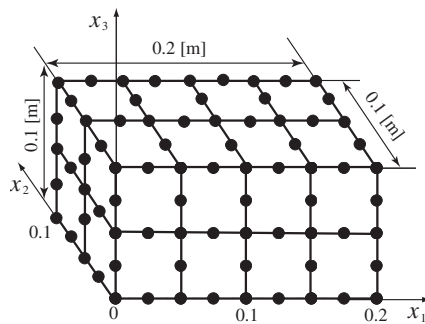


Figure 1 Analysis model and discretization

heat is 440 [J/kgK]. The heat conductivity  $\lambda$  [W/mK] is assumed to be a function of temperature given by

$$\lambda(u) = 98.43 - 0.09155u + 0.2554 \times 10^{-4}u^2 \quad (13)$$

Now, we shall show the numerical results obtained using the time-step width 10 [s] and assuming the support radius as  $a = 1.0, 0.2$  and  $0.1$  [m].

In Fig.2 are shown the temperature distributions on the axis  $x_1$  for various times. Agreeable results are obtained for the two cases of  $a = 1.0$  and  $a = 0.2$ , whereas the case of  $a = 0.1$  does not provide good agreement with the other two cases. As the support radius is reduced, the number of collocation points becomes smaller and numerical accuracy becomes worse. Therefore, it is concluded that a larger support radius provides more accurate numerical results, when an appropriate number of collocation points are assumed.

### Concluding Remarks

A dual reciprocity method has been applied to the time-stepping BEM for the transient heat conduction problem in nonlinear time-dependent materials. The validity of the present method was demonstrated through numerical computation of a simple 3-D example. Further investigation of numerical properties of the present method is required for more complicated 3-D models to make clear the numerical aspects of the method.

**Acknowledgements.** Parts of this work were financially supported by the Ministry of Education, Science, Sports and Culture, Japan, Grant-in-Aid for Scientific Research (C), No. 16560066, 2004, granted the first author (MT). This financial support is gratefully acknowledged.

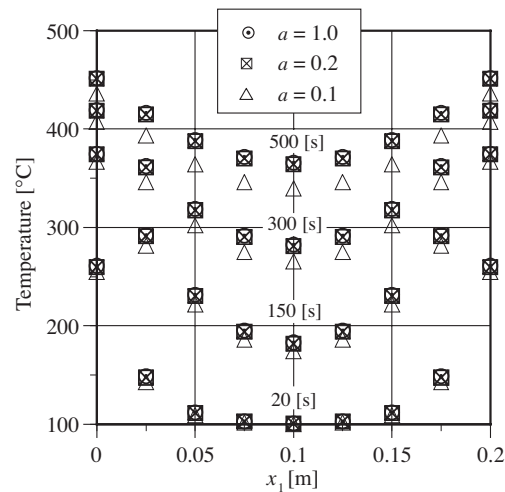


Figure 2 Temperature distribution along axis  $x_1$

## References

- [1] P. W. Partridge, C. A. Brebbia and L. C. Wrobel. *The Dual Reciprocity Boundary Element Method*, Computational Mechanics Publications, (1992).
- [2] P. W. Partridge. Towards criteria for selecting approximation function in the dual reciprocity method, *Engineering Analysis with Boundary Elements*, **24**, pp. 519-529, (2000).
- [3] C. S. Chen, C. A. Brebbia and H. Power. Dual reciprocity method using compactly supported radial basis functions, *Commun. Numer. Meth. Engng.*, **15**, pp.137-150, (1999).
- [4] P. A. Ramachandran and K. Balakrishnan. Radial basis function as approximate particular solutions : Review of recent progress, *Engineering Analysis with Boundary Elements*, **24**, pp. 575-582, (2000).
- [5] Masa. Tanaka, T. Matsumoto and Q.-F. Yang. Time stepping boundary element method applied to 2-D transient heat conduction problems, *Applied Mathematical Modelling*, **18**, pp. 569-576, (1994).
- [6] Masa. Tanaka, T. Matsumoto and Q.-F. Yang. A time-stepping boundary element method for transient heat conduction in orthotropic bodies, *Engineering Analysis with Boundary Elements*, **12**, pp. 85-91, (1993).
- [7] Masa. Tanaka, T. Matsumoto and Y. Suda. A dual reciprocity boundary element method applied to the steady-state heat conduction problem of functionally gradient materials (Study on two-dimensional problems), *Transactions of Japan Soc. Mech. Engrs.*, **67**-662, Ser. A, pp.1589-1594, (2001).
- [8] Masa. Tanaka, T. Matsumoto and A. Shiozaki. Application of boundary-domain element method to the free vibration problem of plate structures, *Computers and Structures*, **66**, pp.725-73, (1998).

## Parameter Optimisation in Ewald's Method Applied to Shallow Water Acoustic Wave Propagation

J. A. F. Santiago<sup>1</sup> and L. C. Wrobel<sup>2</sup>

<sup>1</sup> COPPE/UFRJ – Programa de Engenharia Civil, Caixa Postal: 68506,  
21945-970 Rio de Janeiro, RJ, Brazil, email: Santiago@pec.coppe.ufrj.br

<sup>2</sup> Brunel University – School of Engineering and Design, Uxbridge, Middlesex  
UB8 3PH, England, email: Luiz.Wrobel@brunel.ac.uk

**Keywords:** Shallow Water Acoustics, Wave Propagation, Ewald's Method

**Abstract.** This article deals with the study of a fitting function for the parameter  $b$  in Ewald's representation of the Green's function used in the numerical simulation of acoustic wave propagation in shallow water by the boundary element method. It is assumed that the problem is two-dimensional, the source of acoustic disturbance is time-harmonic, the velocity of sound is constant and the medium in the absence of perturbations is quiescent. The Green's functions employed directly satisfy the boundary conditions on the free surface and the horizontal parts of the bottom boundary.

### Introduction

A popular alternative to improving the convergence of the series generally used to represent the Green's function for shallow water acoustics is to construct it in the form of eigenfunction expansions, the normal mode solution, which involves the sum of an infinite number of terms; however, if the evanescent modes are ignored and only the propagating modes are retained, the number of terms in the series becomes finite [1]. In spite of that, convergence problems still remain when the source and field points are located along the same vertical line [2,3].

Recent papers by Linton [4,5] and Papanicolaou [6] discuss numerous mathematical techniques for accelerating slowly convergent series. They show that one powerful technique is the method of Ewald [7], which is capable of providing dramatic improvements in the speed of convergence. This method has been successfully implemented in the BEM context by Venakides *et al.* [8], for the calculation of electromagnetic scattering of photonic crystals.

In the present article, a two-dimensional model is studied as representative of coastal regions, which have little variation in the long shore direction. The Ewald's method was derived and implemented for speeding-up the calculations of the eigenfunction expansion of the Green's function. The accuracy of both forms of the Green's function obtained by the techniques above mentioned are compared with respect to the number of iterations, particularly close to singularities. The comparison accounts for source points located at a fixed position and field points moving along different vertical and horizontal lines.

### Governing equations of the problem

Consider the problem of acoustic wave propagation in a region  $\Omega$  of infinite extent with irregular seabed topography [3], shown in Fig. 1.

If the medium in the absence of perturbations is quiescent, the velocity of sound is constant and the source of acoustic disturbance is time-harmonic, the problem is governed by the Helmholtz equation [9]

$$\nabla^2 \varphi + k^2 \varphi = - \sum_{\alpha=1}^{Nes} B_{\alpha} \delta(\mathbf{E}_{\alpha}, \mathbf{S}) \quad \text{in } \Omega \quad (1)$$

where  $\varphi$  is the velocity potential,  $B_\alpha$  is the magnitude of the sound source  $\mathbf{E}_\alpha$  located at  $(x_{e_\alpha}, y_{e_\alpha})$ ,  $\mathbf{S}$  is the source point, located at  $(u, v)$ ,  $N_{es}$  is the number of sound sources,  $\delta(\mathbf{E}_\alpha, \mathbf{S})$  is the Dirac delta generalised function and  $k = \omega/c$  is the wave number, with  $\omega$  the natural frequency and  $c$  the velocity of sound in the medium.

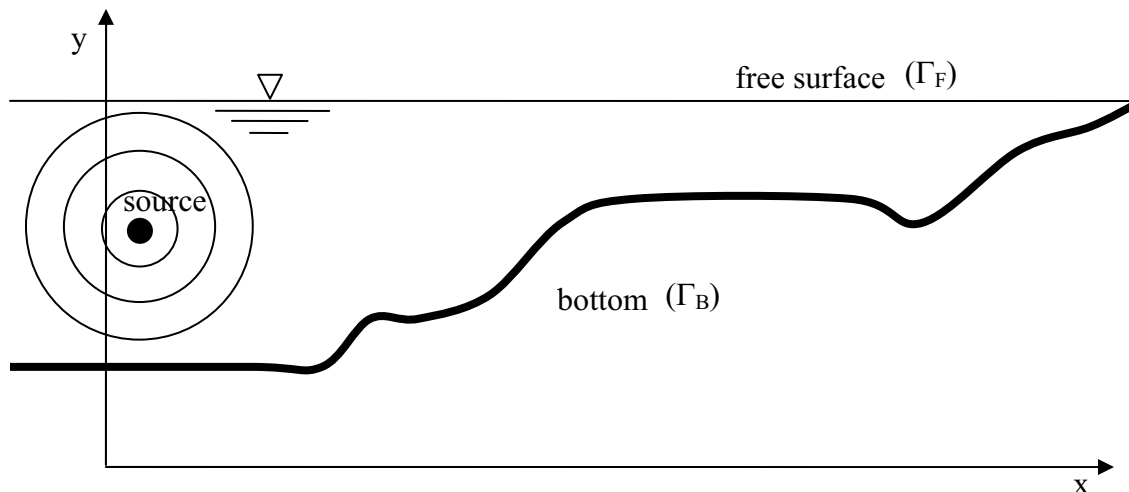


Figure 1: General ocean section for two-dimensional acoustic propagation problems in shallow water

The problem is subject to the following boundary conditions:

$$\text{- at } \Gamma_F: \quad \varphi(\mathbf{X}) = 0 ; \quad \text{at } \Gamma_B: \quad \frac{\partial \varphi}{\partial n}(\mathbf{X}) = 0 \quad (2a)$$

$$\text{- Sommerfeld radiation condition at infinity:} \quad \frac{\partial \varphi}{\partial n}(\mathbf{X}) = ik\varphi(\mathbf{X}) \quad (2b)$$

in which  $\mathbf{X}$  is the field point, located at  $(x, y)$ ,  $n$  is the outward normal and  $i = \sqrt{-1}$ .

According to Green's second identity, Equation (1) can be transformed into the following boundary integral equation [10]

$$C(\mathbf{S})\varphi(\mathbf{S}) = \int_{\Gamma} G(\mathbf{S}, \mathbf{X}) \frac{\partial \varphi}{\partial n}(\mathbf{X}) d\Gamma - \int_{\Gamma} \frac{\partial G}{\partial n}(\mathbf{S}, \mathbf{X}) \varphi(\mathbf{X}) d\Gamma + \sum_{\alpha=1}^{N_{es}} B_\alpha \delta(\mathbf{E}_\alpha, \mathbf{S}) \quad (3)$$

where  $\Gamma$  is equal to  $\Gamma_F \cup \Gamma_B$  and  $G(\mathbf{S}, \mathbf{X})$  is the Green's function. The function  $\partial \varphi / \partial n(\mathbf{X})$  represents the normal derivative of the velocity potential. The coefficient  $C(\mathbf{S})$  depends on the boundary geometry at the source point  $\mathbf{S}$ . It is noted that the Green's function implicitly satisfies the Sommerfeld condition, therefore no discretization of the boundary at infinity is necessary.

Instead of using the Green's function  $G(\mathbf{S}, \mathbf{X})$  of the Helmholtz equation for a line source in a plane geometry, it is possible to adopt Green's functions which directly satisfy the boundary conditions on  $\Gamma_F$  and horizontal parts of  $\Gamma_B$ . Therefore, only the irregular parts of the bottom boundary need to be discretized.

### Fundamental solutions

**Eigenfunction expansion.** The Green's function  $G_M(\mathbf{S}, \mathbf{X})$  exactly satisfies the boundary conditions on the free surface and the bottom boundaries. This series, in terms of normal modes, can be written as [9]:

$$G_M(\mathbf{S}, \mathbf{X}) = \frac{1}{H} \sum_{m=1}^{\infty} \left\{ \sin[k_{ym}(Y_F - v)] \sin[k_{ym}(Y_F - y)] \frac{e^{-\sqrt{-k_{xm}}|x-u|}}{\sqrt{-k_{xm}}} \right\} \quad (4)$$

where  $H$  is the depth of the free surface ( $Y_F - Y_B$ );  $Y_F$  and  $Y_B$  are the  $y$  co-ordinate of the free surface and bottom, respectively and the parameters  $k_{xm}$  and  $k_{ym}$  are horizontal and vertical wavenumbers, respectively:

$$k_{ym} = \left(m - \frac{1}{2}\right) \frac{\pi}{H} \quad k_{xm} = k^2 - k_{ym}^2 \quad (5)$$

**Ewald's method.** An alternative form of representing Equation (4) is [11]

$$G_E(\mathbf{S}, \mathbf{X}) = \frac{2}{H} \sum_{m=1}^{\infty} \sin[k_{ym}(Y_F - v)] \sin[k_{ym}(Y_F - y)] \int_0^{\infty} \frac{e^{k_{xm}t - \frac{(x-u)^2}{4t}}}{\sqrt{4\pi t}} dt \quad (6)$$

The underlying idea of Ewald's representation is to split the integral in Equation (6) into two parts [6],

$$G_{E1}(\mathbf{S}, \mathbf{X}) = \frac{2}{H} \int_0^{b^2} \frac{1}{\sqrt{4\pi t}} \sum_{m=1}^{\infty} e^{k_{xm}t - \frac{(x-u)^2}{4t}} \sin[k_{ym}(Y_F - v)] \sin[k_{ym}(Y_F - y)] dt \quad (7a)$$

$$G_{E2}(\mathbf{S}, \mathbf{X}) = \frac{2}{H} \sum_{m=1}^{\infty} \sin[k_{ym}(Y_F - v)] \sin[k_{ym}(Y_F - y)] \int_{b^2}^{\infty} \frac{e^{k_{xm}t - \frac{(x-u)^2}{4t}}}{\sqrt{4\pi t}} dt \quad (7b)$$

where the parameter  $b$ , which divides the integral in Equation (7), is chosen appropriately, taking account of the position of the source and field points. This parameter was chosen by the following function (when source and field points are located at the same vertical line):

$$b(r) = \frac{\alpha}{2} \left\{ 1 + \cos \left[ \frac{\pi(r + \gamma)}{\gamma} \right] \right\} \quad 0 \leq r \leq \gamma \quad (8)$$

$$b(r) = \alpha \quad r > \gamma$$

where  $\alpha$  and  $\gamma$  are constants and  $r$  is the distance between  $\mathbf{S}$  and  $\mathbf{X}$ .

In the present paper the constants  $\alpha$  and  $\gamma$  are taken to be 0.1 and 1.0 m, respectively. The corresponding function  $b(r)$  obtained with these values is shown in Fig. 2.

Therefore, the final expression of Ewald's representation of the Green's function (6) is:

$$G_E(\mathbf{S}, \mathbf{X}) = \frac{C_n}{4\pi} + \sum_{m=1}^{\infty} \left\{ \frac{\sin[k_{ym}(Y_F - v)] \sin[k_{ym}(Y_F - y)]}{2H\sqrt{-k_{xm}}} \left\{ e^{(x-u)\sqrt{-k_{xm}}} \operatorname{erfc} \left[ b\sqrt{-k_{xm}} + \frac{(x-u)}{2b} \right] + e^{-(x-u)\sqrt{-k_{xm}}} \operatorname{erfc} \left[ b\sqrt{-k_{xm}} - \frac{(x-u)}{2b} \right] \right\} + \frac{\cos(\pi m)}{4\pi} \sum_{n=0}^{\infty} \frac{k^{2n} b^{2n}}{n!} \left[ \sum_{j=1}^4 (-1)^j E_{n+1} \left( \frac{a_{jm}}{b^2} \right) \right] \right\} \quad (9)$$

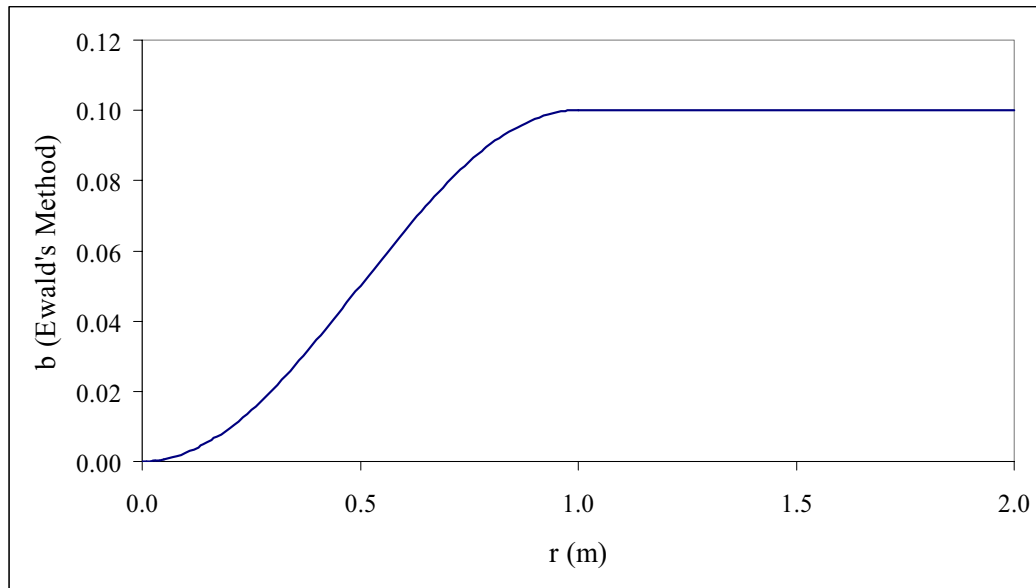


Figure 2: Function used as parameter  $b$  in Ewald's Method

where  $E_{n+1}$  is the exponential integral function,  $erfc(z)$  is the complementary error function and the coefficients  $C_n$ ,  $a_1$ ,  $a_2$  and  $a_{jm}$  are defined in the form:

$$C_n = \sum_{n=0}^{\infty} \frac{k^{2n} b^{2n}}{n!} \left[ E_{n+1} \left( \frac{a_1}{b^2} \right) - E_{n+1} \left( \frac{a_2}{b^2} \right) \right] \quad (10)$$

$$\begin{aligned} a_1 &= \frac{(x-u)^2 + (v+y)^2}{4} & a_2 &= \frac{(x-u)^2 + (-Y_F + v + y)^2}{4} \\ a_{1m} &= \frac{(x-u)^2 + (2Hm - 2Y_F + v + y)^2}{4} & a_{2m} &= \frac{(x-u)^2 + (2Hm + v - y)^2}{4} \\ a_{3m} &= \frac{(x-u)^2 + (-2Hm - 2Y_F + v + y)^2}{4} & a_{4m} &= \frac{(x-u)^2 + (2Hm - v + y)^2}{4} \end{aligned} \quad (11)$$

### Example

A problem of acoustic wave propagation from a region of depth  $h = 2.0 \text{ m}$  to a region of depth  $h = 10.0 \text{ m}$  was studied in order to verify the performance of the function  $b(r)$  in the Ewald series. Different situations were considered, in which the position of the source point  $\mathbf{S}$  was fixed and the field point  $\mathbf{X}$  varied along a vertical and a horizontal line. The sound velocity and frequency are taken to be  $1500 \text{ m/s}$  and  $1000 \text{ Hz}$ , respectively (see reference [11]).

Figures 3 and 4 show the behaviour of the real part of the functions  $G_M [\text{Re}(\text{GM})]$  and  $G_E [\text{Re}(\text{GE})]$ , in a region of constant depth of  $10.0 \text{ m}$ , for source points placed at the fixed positions  $(1.0, 8.0) \text{ m}$  and  $(1.0, 5.0) \text{ m}$ , respectively. The field points are located along the vertical line passing through the source point.

It is noticed that, for the present case, the real part of the functions  $G_M(\mathbf{S}, \mathbf{X})$  and  $G_E(\mathbf{S}, \mathbf{X})$  produced virtually the same results, confirming the validity of Ewald's representation.

Figure 5 presents the number of iterations necessary for the functions  $G_M$  (NiGM) and  $G_E$  (NiGE) to converge, for a source point  $\mathbf{S}$  located at the positions  $(1.0, 8.0) \text{ m}$  and a field point  $\mathbf{X}$

moving along the same vertical line in which the source point is located, from  $y = 0.0$  to  $y = 10.0$  m. It can be seen that a much faster convergence is produced by the function  $G_E$  (number of iterations around 60).

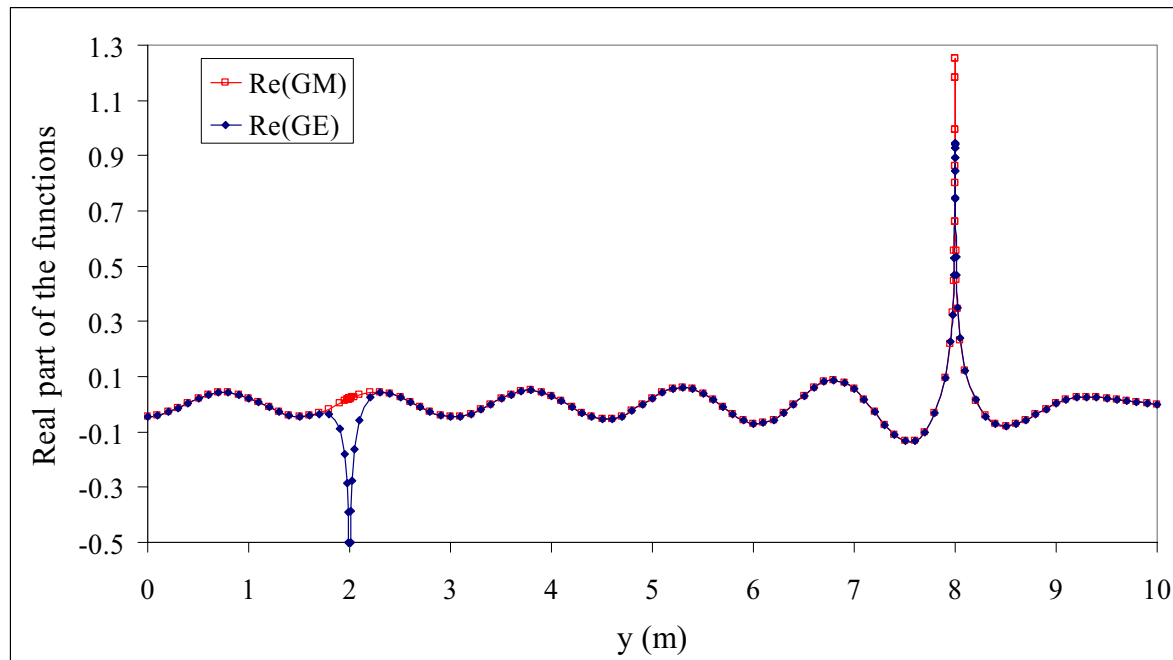


Figure 3: Real part of the functions  $GM(\mathbf{S}, \mathbf{X})$  and  $GE(\mathbf{S}, \mathbf{X})$  along of a vertical line for  $\mathbf{S}$  located at  $(1.0, 8.0)$

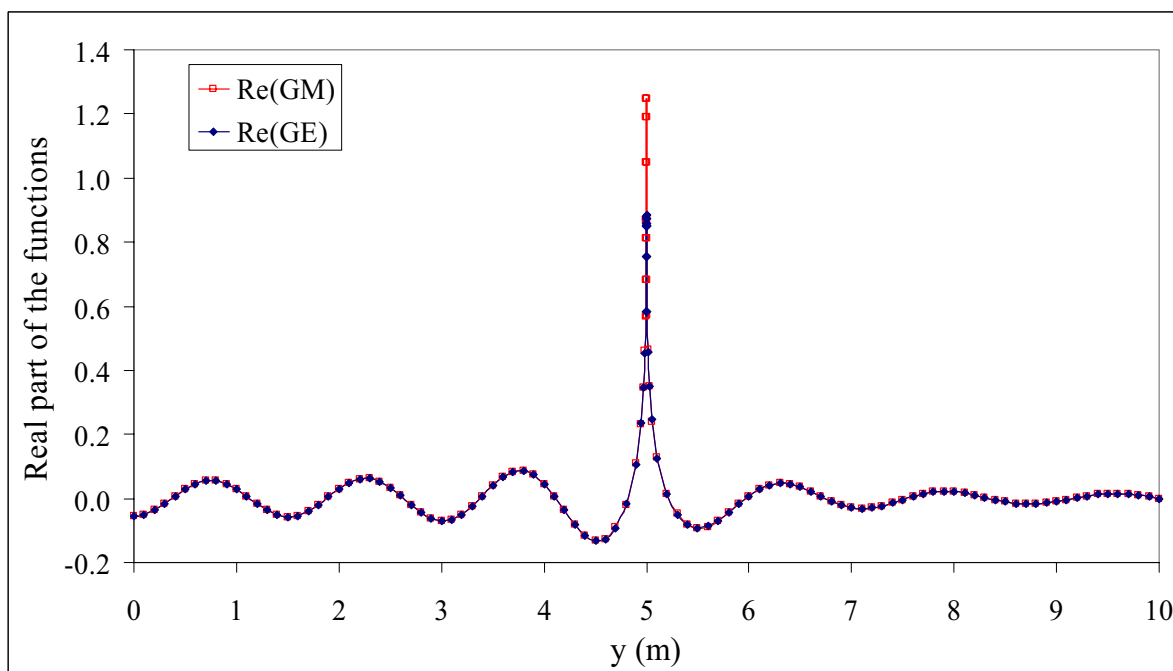


Figure 4: Real part of the functions  $GM(\mathbf{S}, \mathbf{X})$  and  $GE(\mathbf{S}, \mathbf{X})$  along of a vertical line for  $\mathbf{S}$  located at  $(1.0, 5.0)$

## Conclusions

The Ewald's method was derived in this paper for speeding-up the calculations of the eigenfunction expansion of the Green's function for underwater acoustics used by the BEM. It was shown that Ewald's representation is accurate and efficient method when the source and field points are located along the same

vertical line or otherwise. The influence of the parameter  $b$  used to split the infinite integral was investigated, as well as the singular integral generated by the infinite series obtained by the Ewald's method.

According to this preliminary study, the proposed function  $b(r)$  employed as parameter in the Ewald's method presented a good performance. Higher values of  $b$  improve the speed of convergence of the series for source and field points placed along the same vertical line, while the accuracy near singularities is improved by using lower values of  $b$ .

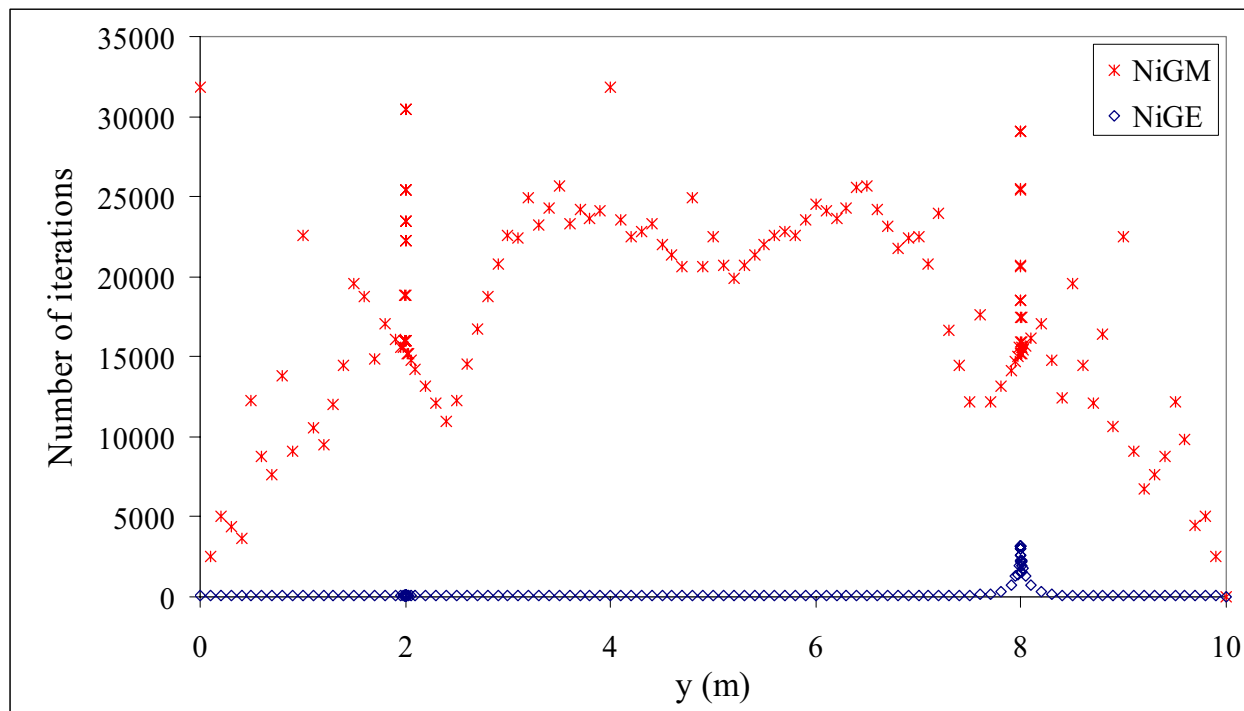


Figure 5: Number of iterations of the functions  $GM(\mathbf{S}, \mathbf{X})$  and  $GE(\mathbf{S}, \mathbf{X})$  along of a vertical line

## References

- [1] T.W. Wu, On computational aspects of the boundary element method for acoustic radiation and scattering in a perfect waveguide, *J. Acoust. Soc. Am.*, **96**, 3733-3743, 1994.
- [2] T.W. Dawson and J.A. Fawcett, A boundary integral equation method for acoustic scattering in a waveguide with nonplanar surfaces, *J. Acoust. Soc. Am.*, **87**, 1110-1125, 1990.
- [3] J.A.F. Santiago and L.C. Wrobel, A boundary element model for underwater acoustics in shallow waters, *Computer Modeling in Engineering & Science*, **1**, 73-80, 2000.
- [4] C.M. Linton, The Green's function for the two-dimensional Helmholtz equation in periodic domains, *Journal of Engineering Mathematics*, **33**, 377-402, 1998.
- [5] C.M. Linton, Rapidly convergent representations for Green's functions for Laplace's equation, *Proc. Royal Society A*, **455**, 1767-1797, 1999.
- [6] V. Papanicolaou, Ewald's method revisited: Rapidly convergent series representation of certain Green's functions, *J. Comput. Anal. Appl.*, **1**, 105-114, 1999.
- [7] P.P. Ewald, Die Berechnung optischer and elektrostatischen Gitterpotentiale, *Ann. Phys.*, **64**, 253-268, 1921.
- [8] S. Venakides, M.A. Haider and V. Papanicolaou, Boundary integral calculations of two-dimensional electromagnetic scattering by photonic crystal Fabry-Perot structures, *SIAM J. Appl. Math.*, **60**, 1686-1706, 2000.
- [9] L.E. Kinsler, A.R. Frey, A.B. Coppens and J.V. Sanders, *Fundamentals of Acoustics*, 3rd edition, Wiley, New York, 1982.
- [10] L.C. Wrobel and M.H. Aliabadi, *The Boundary Element Method*, Wiley, Chichester, 2002.
- [11] J.A.F. Santiago and L.C. Wrobel, Modified Green's Functions for Shallow Water Acoustic Wave Propagation, *Engineering Analysis with Boundary Elements*, **28**, 1375-1385, 2004.

## Application of Boundary Element Method to Modeling of Hydrodynamic Forces and Experimental Validation

Paola Gardano<sup>1</sup>, Peter Dabnichki<sup>2</sup> and Ferri Aliabadi<sup>3</sup>

<sup>1</sup>Department of engineering, Queen Mary, University of London, Mile End Road, London, E1 4NS, UK p.gardano@qmul.ac.uk

<sup>2</sup> Department of engineering, Queen Mary, University of London, Mile End Road, London, E1 4NS, UK p.dabnichki@qmul.ac.uk

<sup>3</sup> Department of Aeronautics, Imperial College, Prince Consort Road, London, SW7 2BY, UK, m.h.aliabadi@imperial.ac.uk

**Keywords:** Boundary Element Methods; Stokes equation; flow visualization;

**Abstract** The present work aimed to identify different mechanisms of propulsive force generated by the flow around a moving arm and to identify the unsteady effects generated by the crawl stroke in quasi static condition. Boundary Element Method was utilized to produce benchmark data for the magnitude of the propulsive force in ideal conditions free of turbulence and unsteady effects. Interestingly, the steady flow produced hydrodynamic force patterns that compare well with the quasi-static ones obtained on a prosthetic arm model in a low speed wind tunnel where both unsteady effects and turbulence were evident. Flow visualization was undertaken to illustrate such unsteady effects as wake and vortex formation and underline mechanism of unsteady flow generation due to the arm geometry.

### Introduction

Front crawl is the fastest and most effective swimming style. The arm movement in freestyle is alternating; one arm is pushing/pulling while the other is recovering. The arm stroke is the greatest contributor to the forward movement of the swimmer. Propulsion is one of the key factors determining performance in human competitive swimming. In literature two different hypotheses suggested the propulsion generation. One of them affirms that the dominant mean of the propulsion is the lift generated by the difference of pressure between the front and the back of the hand, comparing swimmer's hand to a foil. As curved a pressure difference between the two sides is created and this, according to Bernoulli's principle, creates lift. The other opinion about propulsion is that the drag is the dominant propulsive force in freestyle swimming and that much of the total propulsive force comes from the forearm.

Swimming research was initially confined to steady analysis. Berger et al. [2] obtained experimentally quasi-steady forces for a comparison with Schleihau [11] results. Unsteady effects were introduced and analyzed in terms of kinematic analysis of hand's trajectory (Berger et al., Pay and Hay [4, 7]). But all these works underlined the difficulties to find purely experimental explanation to propulsive force generation.

An alternative method is the use of computational fluid dynamic (CFD) to obtain the solution and avoid most of the problems that typically affect the experiment. Bixler and Riewald [4] used the CFD to calculate steady-state force coefficients for validation technique of the results obtained experimentally.

The aim of this project is to asses the influence of the unsteady effects on the magnitude of the propulsive forces trough the estimation of the two contributes (Lift and Drag) with Boundary Element technique and the comparison with experimental results and flow visualization.

### Method

The velocity, pressure and stress Green's function of three-dimensional Stokes flow, denoted respectively by  $G_{ij}$ ,  $p_{ij}$  and  $T_{ijk}$ , where the indices  $i, j, k$  correspond to  $x, y$  and  $z$ , are defined

such that the velocity field at the field point  $\bar{x} = (x, y, z)$  induced by a three-dimensional point force with strength  $\bar{b}$  placed at the singular point  $\bar{x}_o = (x_o, y_o, z_o)$  is given by

$$u_i(\bar{x}) = \frac{1}{8\pi\mu} G_{ij}(\bar{x}, \bar{x}_o) b_j = \frac{1}{8\pi\mu} G_{ji}(\bar{x}_o, \bar{x}) b_j \quad (1)$$

where  $\mu$  is the fluid viscosity. The pressure and stress fields are

$$p(\bar{x}) = \frac{1}{8\pi} p_j(\bar{x}, \bar{x}_o) b_j \quad (2)$$

and

$$\sigma_{ik}(\bar{x}) = \frac{1}{8\pi} T_{ijk}(\bar{x}, \bar{x}_o) b_j \quad (3)$$

From the Newtonian constitutive equation, we have

$$T_{ijk} = \delta_{ik} p_j + \frac{\partial G_{ij}}{\partial x_k} + \frac{\partial G_{kj}}{\partial x_i} \quad (4)$$

From the continuity equation and the Stokes equation we obtain that the velocity, the pressure and the stress Green's function satisfy the following equation

$$\frac{\partial G_{ij}}{\partial x_i} = 0 \quad (5)$$

$$-\frac{\partial p_j}{\partial x_i} + \left( \frac{\partial^2 G_{ij}}{\partial x^2} + \frac{\partial^2 G_{ij}}{\partial y^2} + \frac{\partial^2 G_{ij}}{\partial z^2} \right) = -8\pi \delta_{ij} \delta_3(\bar{x} - \bar{x}_o) \quad (6)$$

$$\frac{\partial T_{ijk}}{\partial x_k} = \frac{\partial T_{kji}}{\partial x_k} = -8\pi \delta_{ij} \delta_3(\bar{x} - \bar{x}_o) \quad (7)$$

The boundary element procedure was applied to compute the flow past a body in an infinite domain. The fluid velocity  $\bar{u}$  is composed solely by incident component  $\bar{u}^\infty$ , the expression of the flow sufficiently far from the body along the x-axis. The boundary-integral representation for the velocity of a three-dimensional Stokes flow is

$$u_j(\bar{x}_o) = \bar{u}_j^\infty(\bar{x}_o) - \frac{1}{8\pi\mu} \int_D G_{ij}(\bar{x}, \bar{x}_o) f_i(\bar{x}) dS(\bar{x}) \quad (8)$$

where  $\mu$  is the fluid viscosity,  $D$  is the particle surface,  $\bar{n}$  is the unit normal vector pointing into the fluid, and  $G_{ij}$  is the velocity Green's function. By taking the limit as the point  $\bar{x}_o$  approaches the body surface, an integral equation of the first kind for the boundary distribution of the traction over the body surface is obtained. The program computes then the Forces acting along the x-axis (Drag Force) and y-axis (Lift Force).

The analysed body is a three dimensional model of a human arm performing front crawl stroke. The arm shape has been obtained from an ellipsoid volume by applying some geometrical modifications,

contractions and dilations, in precise point of the surface. In order to simplify the model the hand is modelled as a dome as this is the shape assumed by swimmers.

The body surface was discretized into a collection of six-node triangular rigid shell elements. The angle between the x-axis along the model and the flow direction, the angle of attack is the stroke kinematic variable. The range was  $0^\circ$  -  $130^\circ$  in increments of  $10^\circ$ . The elbow angle was changed and different tests were carried on for elbow angle of  $180^\circ$  and  $135^\circ$ .

The most effective method to evaluate the accuracy and reliability of numerical data on the propulsive forces generated by the hand, forearm and upper arm directly is to carry out some experiments in a close-return low-speed wind tunnel. A prosthetic arm with identical human shape and dimensions was used (Figure 1). Thanks to a Kistler force plate, Drag and Lift contributions for different configurations and speeds were analyzed. The angle of attack of the model, the shoulder rotation if we consider the real swimmer movement, was varied from  $\alpha = 0^\circ$  to  $\alpha = 140^\circ$  in increments of  $10^\circ$ . The angle between upper arm and forearm of the model was fixed in values of  $180^\circ$  and  $135^\circ$ . The speed of the flow was varied according to the hand velocity of the swimmer in water (from 1.6m/s to 4.5m/s) with a suitable conversion to the air values (15m/s to 35m/s). To have a better understanding of the circulation and the turbulence phenomena we analysed the flow around the arm with a flow visualization technique that makes use of cotton or wool yarns on the region of interest on the model. These tufts and their movements are the direct response to the aerodynamic force that aligns the yarn to the fluid lines.

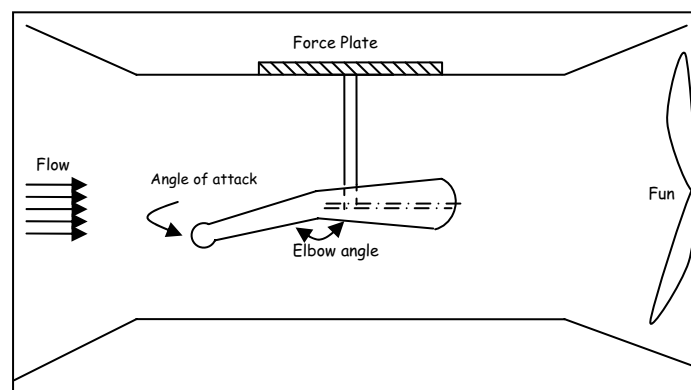


Fig. 1 Schematic drawing of the prosthetic arm fixed to the Force Plate on the roof of a low speed wind tunnel. The flow direction is indicated.

## Results

Drag Force measured with BEM as function of the angle of attack and angle of elbow  $180^\circ$  showed a perfect sine-wave development with a minimum near to  $0^\circ$  and a peak value of 30N in the shoulder position  $85^\circ$  (Fig. 2). For the configuration elbow  $135^\circ$  the trend is still sine-wave with a minimum in proximity of zero and a maximum around  $90^\circ$  (Fig. 3). The trend is very similar to that obtained from the experimental results with a difference in terms of value due to the different speeds. The Lift Force in the configuration angle of the elbow  $180^\circ$  showed two peaks in correspondence of  $40^\circ$  and  $135^\circ$  and a minimum for the angle of attack  $90^\circ$  (Fig. 4). In the configuration with angle between upper arm and forearm  $135^\circ$  the Lift path showed two peaks in the shoulder position  $60^\circ$  and  $140^\circ$  and a minimum in  $100^\circ$  (Fig. 5). The trends follow quite regularly the experimental results. Figure 6 and 7 show trends for Lift and Drag together in all the analyzed configurations.

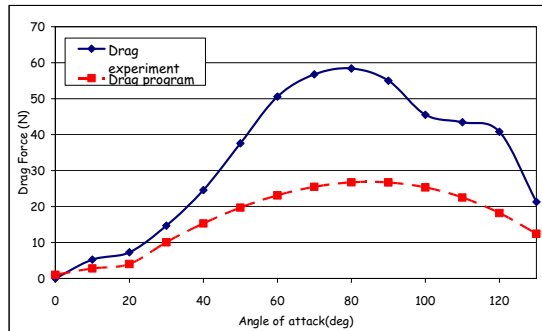


Fig. 2 Drag Force in the configuration elbow 180 degree comparison experimental and computational arm

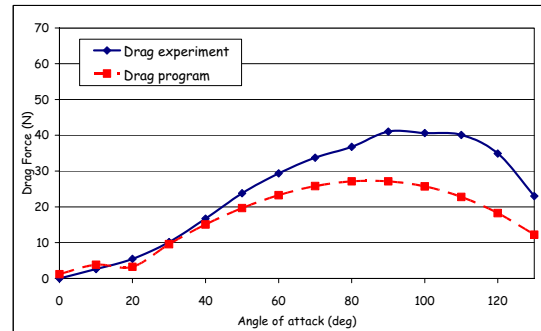


Fig. 3 Drag Force in the configuration elbow 135 degree comparison experimental and computational arm

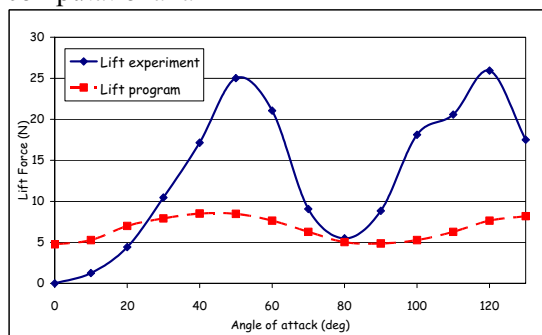


Fig. 4 Lift Force in the configuration elbow 180 degree comparison program and experimental arm

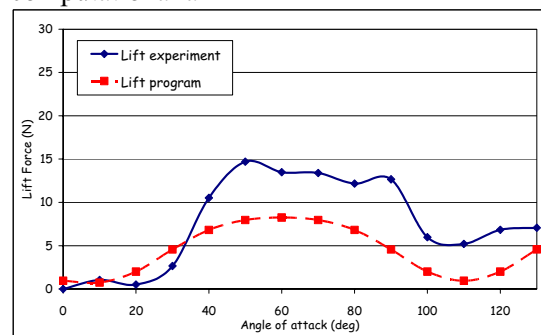


Fig. 5 Lift Force in the configuration elbow 135 degree comparison program and experimental arm

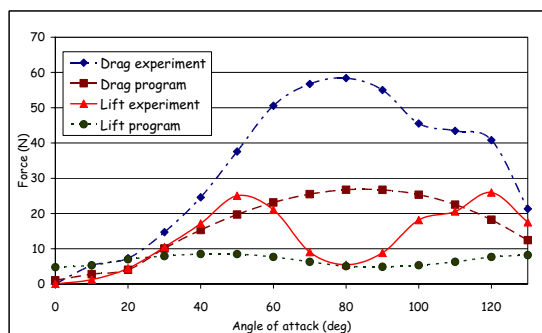


Fig. 6 Comparison Drag and Lift Force in the configuration elbow 180 degree for program and experimental arm

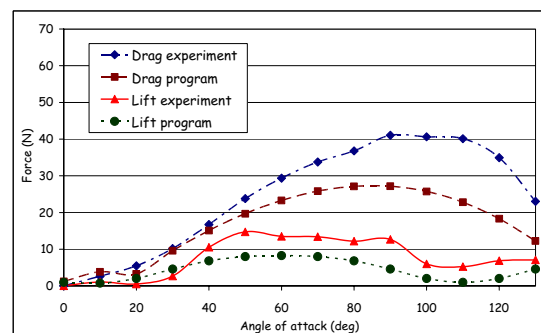


Fig. 7 Comparison Drag and Lift Force in the configuration elbow 135 degree for program and experimental arm

### Discussion

To validate the Boundary Element Method, the propulsive steady forces during the front stroke calculated with this technique were compared to the experimental ones obtained from a prosthetic arm in a wind tunnel. We considered two elbow configurations. The first one is with straight arm and angle between forearm and upper arm  $180^\circ$  and the second with an elbow angle close to  $135^\circ$ . Even if the Drag trends are similar for experimental data and computational ones, there is a divergence in terms of values due to the difference of approach. In the program we solved a Stokes flow, steady and ideal fluid. The speed is always the same and the only variable is the angle of attack. This is clearly visible from the perfect sine-wave pattern of the Drag Force. Otherwise the measurement of the experimental Drag has a dependency on the speed too. For every single angle of attack the velocity of the flow has been changed according to a quasi-static approach. In this way we can underline the importance of the time dependency introduction in the BE technique in order to analyze the effect of the acceleration of the arm during the front stroke. The acceleration and deceleration effect is important to explain the effect of the added mass of water and the increment of the resultant Force.

The Lift trends for experimental and computational arm show peaks and minimum of value in the same position but with a discrepancy in terms of strength of Force. This is due to the fact that the Lift is given predominantly by the hand, its curvature and by the asymmetry of the body. The model used in the BEM simulation was perfectly symmetric and the hand a dome without any curvature between palm and back that is the main source for the Lift.

The flow visualization analysis has resulted a good validation way of the previous set of the experiments on the arm. When the air invests the arm a difference of pressure from the two different sides of the model is generated. This causes a movement of the air from the high pressure area to low pressure air and a consequent curl up of the stream lines (Fig. 8). This starts the wake vortex and small vortices ready to develop from that. Shedding of each vortex produces circulation and gives rise to a lateral force on the arm. For the position from 50 to 90 degree the tufts movement showed a circulation around the forearm and the hand with a big depression in the internal part of the arm and the consecutive creation of the propulsive force. In this way it's clear that the most of the thrust is given from forearm and hand.

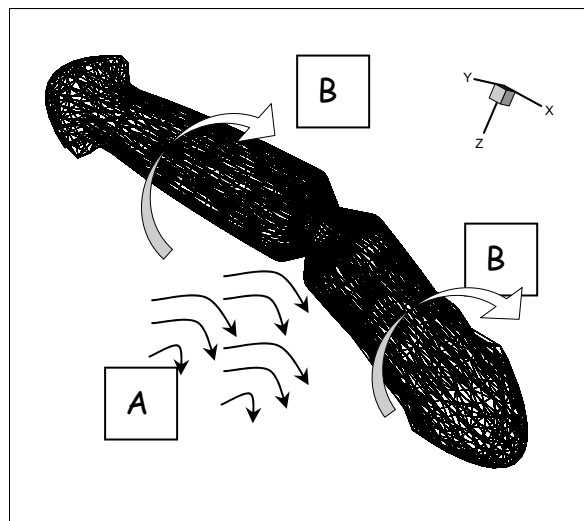


Fig. 8 BEM surface mesh of hand and arm model with draw vortices in proximity of the elbow (zone A) and circulation around the arm (zone B)

### Conclusions

The BEM was selected for the computational study because of its effectiveness to obtain a unique solution. The method allows to avoid detailed modelling of the flow pattern without sacrificing the accuracy of the estimated Drag and Lift development along the three dimensional arm for different configurations with respect to the angle of attack.

Even if the obtained Stokes flow results are surprisingly good in terms of Drag force development during the stroke, the Stokes flow is quite far from the real condition in which the arm has to work during the front crawl. So the next step as future project in the computational field will be to find the solution to Navier-Stokes equation and consider in the flow analysis also the effect of the acceleration, turbulence and vortices generation.

### References

- [1] Aliabadi, M. H. *The Boundary Element Method. Vol.2. Applications in solids and structures.* (2002).
- [2] Berger, M. A., de Groot, G., Hollander A. P. *Hydrodynamic drag and lift forces on human hand arm models. Journal of Biomechanics* 28, 125-133 (1995).
- [3] Berger, M. A. M., Hollander and A. P., De Groot, G. *Determining propulsive force in front crawl swimming: A comparison of two methods. Journal of Sports Sciences* 17, 97-105 (1999).
- [4] Bixler, B. and Riewald, S. *Analysis of a swimmer's hand and arm in steady flow conditions using computational fluid dynamics. Journal of Biomechanics* 35, 713-717 (2002).

- [5] Brown, R. M. and Counsilman, J. E. *The role of lift in propelling swimmers. In J.M. Cooper, Biomechanics of Swimming* 59-71 (1971).
- [6] Counsilman, J.E. *Science of Swimming* (1968).
- [7] Pai, Y. and Hay, J.G. *A hydrodynamic study of the oscillation motion in swimming. International Journal of Sport Biomechanics* 4, 21-37 ( 1988).
- [8] Pozrikidis, C. 2002. *A practical guide to the Boundary Element Method with the software library BEMLIB* (2002).
- [9] Pozrikidis, C. *Introduction to Theoretical and Computational Fluid Dynamics* (1997).
- [10] Schleihauf, R.E. *A hydrodynamic analysis of swimming propulsion. J. Terauds, & E.W. Bedingfield (Eds.), Swimming III* 70-109 (1979).

## **A Boundary Element Model for Drop Deformation in Slow Viscous Flows through a Constriction**

Claire Das Bhaumik and Luiz C. Wrobel

School of Engineering and Design, Brunel University,  
Uxbridge UB8 3PH, Middlesex, UK

Keywords: Stokes flow, drop deformation, converging channels

**Abstract.** This work presents a direct BEM formulation for drop deformation in a Stokes flow on a converging channel. Parametric studies are conducted to investigate the effects, on drop deformation, caused by changing the channel's convergence ratio, the drop-fluid viscosity ratio and the initial drop position.

### **Introduction**

Suspensions of particles, drops and bubbles in viscous fluids occur in many biological systems, industrial applications and processes including pharmaceutical manufacturing, food processing, chemical processing, blood flow and viscous sintering. It is important to understand the properties of these fluids in order to gain a better understanding of their behaviour in these systems and processes. This knowledge can then be used to predict fluid behaviour and improve industrial processes.

The study of the motion of particles, drops and bubbles in viscous fluids at low Reynolds number dates at least to 1851, when Stokes [1] published a paper on the problem of a rigid sphere translating through a fluid at zero Reynolds number. Since then, there has been much research in this area, both experimental and theoretical. Main areas of study include flow with rigid boundaries, such as solid inclusions and plane walls, and flows involving deformable interfaces, for example flows containing viscous liquid drops or gas bubbles.

The BEM is an efficient technique for problems involving deforming boundaries such as fluid-fluid interfaces. In these problems, the position of the interfaces must be determined as part of the solution. The BEM enables direct calculation of the interface velocity. Numerical techniques for ODEs can then be used to find new nodal positions. The BEM also has the ability to deal with large surface deformations and other surface effects, such as surface tension, can be easily incorporated.

### **Integral Equation Formulation for Drop Deformation in Stokes Flow**

For problems involving drops of a viscous fluid in another carrying fluid, the region of interest will only be piecewise homogeneous. In this case the BEM must first be applied to each homogenous region individually and the final system produced by considering compatibility and equilibrium conditions on the interfaces.

The relevant compatibility conditions at the interface between drop and bulk fluid are:

$$u_i^f(x) - u_i^d(x) = 0 \quad (1)$$

where  $u_i^f$  is the interface velocity of the bulk fluid and  $u_i^d$  is the velocity at the drop surface. This equation represents continuity of velocity.

The relevant equilibrium conditions are

$$t_i^f(x) - t_i^d(x) = \gamma \kappa(x) n_i(x) \quad (2)$$

where  $t_i$  is the traction,  $t_i = \sigma_{ij} n_j$ ,  $\gamma$  is the surface tension coefficient,  $n_i$  is the unit outward normal vector and  $\kappa$  is the surface curvature. The difference between the tractions  $t_i^f$  and  $t_i^d$  is due to the existence of surface tension.

The velocity field for a point  $x'$  in Stokes flow can be written as [2]

$$c_{ij}(x') u_j(x') = \frac{1}{\mu} \int_S u_{ij}^*(x', x) t_j(x) dS - \int_S p_{ij}^*(x', x) u_j(x) dS \quad (3)$$

where  $\mu$  is the fluid viscosity and  $u_{ij}^*$  is the velocity field of the fundamental solution with traction  $p_{ij}^*$ , given by:

$$u_{ij}^*(x', x) = \frac{1}{4\pi} [-\ln(r) \delta_{ij} + r_{,i} r_{,j}] \quad (4)$$

$$p_{ij}^*(x', x) = \frac{r_{,i} r_{,j} r_{,k}}{\pi r} n_k = \frac{r_{,i} r_{,j}}{\pi r} \frac{\partial r}{\partial n} \quad (5)$$

and  $c_{ij}(x') = \theta(x') \delta_{ij}$ ,  $\theta(x')$  being the internal angle at the point  $x'$ .

For the problem of a drop surrounded by a carrying fluid, the boundary integral equation (3) can be written

$$\begin{aligned} c_{ij}(x') u_j(x') = & \frac{1}{\mu_f} \int_S u_{ij}^*(x', x) t_j(x) dS_e - \int_S p_{ij}^*(x', x) u_j(x) dS_e + \\ & \frac{1}{\mu_f} \int_S u_{ij}^*(x', x) t_j(x) dS_i - \int_S p_{ij}^*(x', x) u_j(x) dS_i \end{aligned} \quad (6)$$

for source points belonging to the bulk fluid, and

$$c_{ij}(x') u_j(x') = -\frac{1}{\mu_d} \int_S u_{ij}^*(x', x) t_j(x) dS_i - \int_S p_{ij}^*(x', x) u_j(x) dS_i \quad (7)$$

for source points belonging to the drop, where  $\mu_f$  is the bulk fluid viscosity and  $\mu_d$  is the drop viscosity;  $S_e$  is the external boundary and  $S_i$  is the drop boundary. The change of sign in equation (7) is due to the change in normal direction for points on the drop surface when they are considered as belonging to the different subregions.

Since we are only concerned with the evolution of the drop boundary, and not with the calculation of the tractions on the drop boundary, it is possible to combine equations (6) and (7) in order to eliminate the interface tractions by using the equilibrium equation (2).

If the viscosity ratio is defined as  $\lambda = \frac{\mu_d}{\mu_f}$ , equation (7) can be written as

$$c_{ij}(x')u_j(x') = -\frac{1}{\lambda\mu_f} \int_S u_{ij}^*(x',x)t_j(x)dS_i + \int_S p_{ij}^*(x',x)u_j(x)dS_i \quad (8)$$

and multiplying by  $\lambda$  gives

$$\lambda c_{ij}(x')u_j(x') = -\frac{1}{\mu_f} \int_S u_{ij}^*(x',x)t_j(x)dS_i + \lambda \int_S p_{ij}^*(x',x)u_j(x)dS_i \quad (9)$$

Adding equations (6) and (9) produces

$$\begin{aligned} c_{ij}(x')u_j(x') &= \frac{1}{\mu_f} \int_S u_{ij}^*(x',x)t_j(x)dS_e - \int_S p_{ij}^*(x',x)u_j(x)dS_e + \\ &\frac{1}{\mu_f} \int_S u_{ij}^*(x',x)[t_j^f(x) - t_j^d(x)]dS_i - \int_S p_{ij}^*(x',x)[u_j^f(x) - \lambda u_j^d(x)]dS_i \end{aligned} \quad (10)$$

for source points belonging to the bulk fluid, and

$$\begin{aligned} (1 + \lambda)c_{ij}(x')u_j(x') &= \frac{1}{\mu_f} \int_S u_{ij}^*(x',x)t_j(x)dS_e - \int_S p_{ij}^*(x',x)u_j(x)dS_e + \\ &\frac{1}{\mu_f} \int_S u_{ij}^*(x',x)[t_j^f(x) - t_j^d(x)]dS_i - \int_S p_{ij}^*(x',x)[u_j^f(x) - \lambda u_j^d(x)]dS_i \end{aligned} \quad (11)$$

for source points belonging to the drop. Taking into account the compatibility and equilibrium conditions, equations (1) and (2), the above equations become

$$\begin{aligned} c_{ij}(x')u_j(x') &= \frac{1}{\mu_f} \int_S u_{ij}^*(x',x)t_j(x)dS_e - \int_S p_{ij}^*(x',x)u_j(x)dS_e + \\ &\frac{\gamma}{\mu_f} \int_S u_{ij}^*(x',x)\kappa(x)n_j(x)dS_i - (1 - \lambda) \int_S p_{ij}^*(x',x)u_j(x)dS_i \end{aligned} \quad (12)$$

for source points on the solid boundary, and

$$\begin{aligned} (1 + \lambda)c_{ij}(x')u_j(x') &= \frac{1}{\mu_f} \int_S u_{ij}^*(x',x)t_j(x)dS_e - \int_S p_{ij}^*(x',x)u_j(x)dS_e + \\ &\frac{\gamma}{\mu_f} \int_S u_{ij}^*(x',x)\kappa(x)n_j(x)dS_i - (1 - \lambda) \int_S p_{ij}^*(x',x)u_j(x)dS_i \end{aligned} \quad (13)$$

for source points on the drop.

### Numerical Simulations

An initially circular drop is placed in a channel and released, when it instantaneously becomes subject to the suspending fluid motion. The fluid in the channel flows due to a pressure difference between inlet and outlet.

The channel used is 310mm long, with a convergence ratio equal to 10. The channel has an inlet width 140mm, converging to an outlet width of 14mm. The elliptical convergence starts at a distance 140mm from the entrance. The drop diameter is 10mm. The discretisation involves 196 elements on the external surface and 30 elements on the drop surface.

In order to investigate the effect of drop-fluid viscosity ratio on drop deformation, viscosity ratio values of 0.5, 4.0 and 10.0 are used.

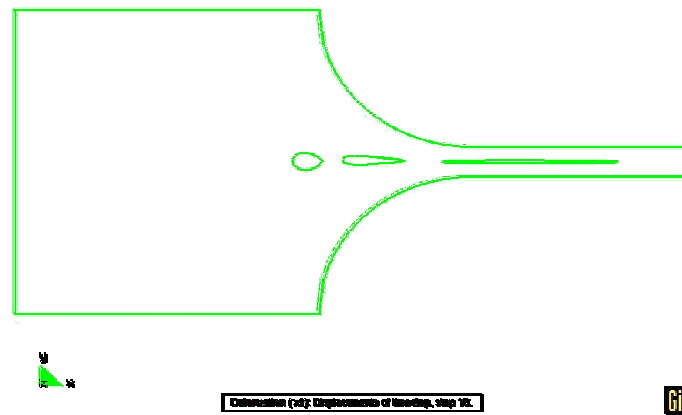


Figure 1 – Drop evolution in channel with convergence ratio = 10, viscosity ratio = 0.5.

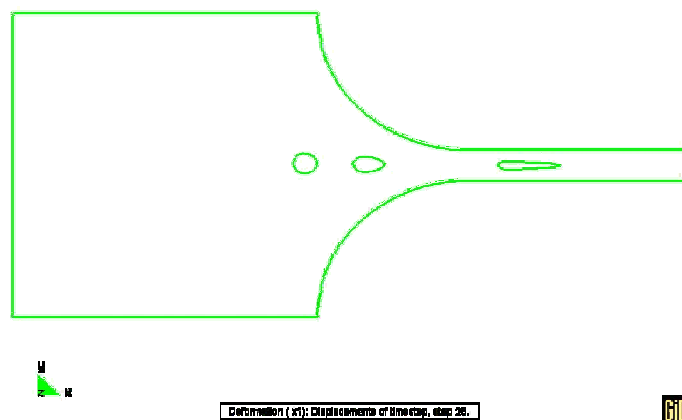


Figure 2 – Drop evolution in channel with convergence ratio = 10, viscosity ratio = 4.

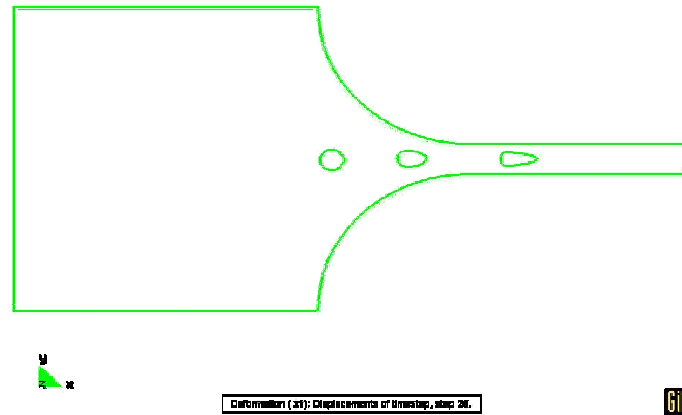


Figure 3 – Drop evolution in channel with convergence ratio = 10, viscosity ratio = 10.

The evolution of the drop geometry is shown after 200, 360 and 500 time steps in figures 1 and 2, and after 280, 420 and 500 time steps in figure 3. The change in drop area was less than 2% for a viscosity ratio of 0.5, 1% for a viscosity ratio of 4 and 0.2% for a viscosity ratio of 10. It can be seen that once the drop has entered the constricted part of the channel, it takes on an elongated shape due to elongational and shear effects.

The drop relative deformation,  $\alpha(t) = [P(t) - P_0] / P_0$ , is used as an indicator of the amount of deformation the drop undergoes. In this equation,  $P(t)$  is the drop perimeter at time step  $t$  and  $P_0$  is the initial drop perimeter. The conservation of the drop area was used to verify the accuracy of the calculations. The drop relative deformation is shown in figure 4.

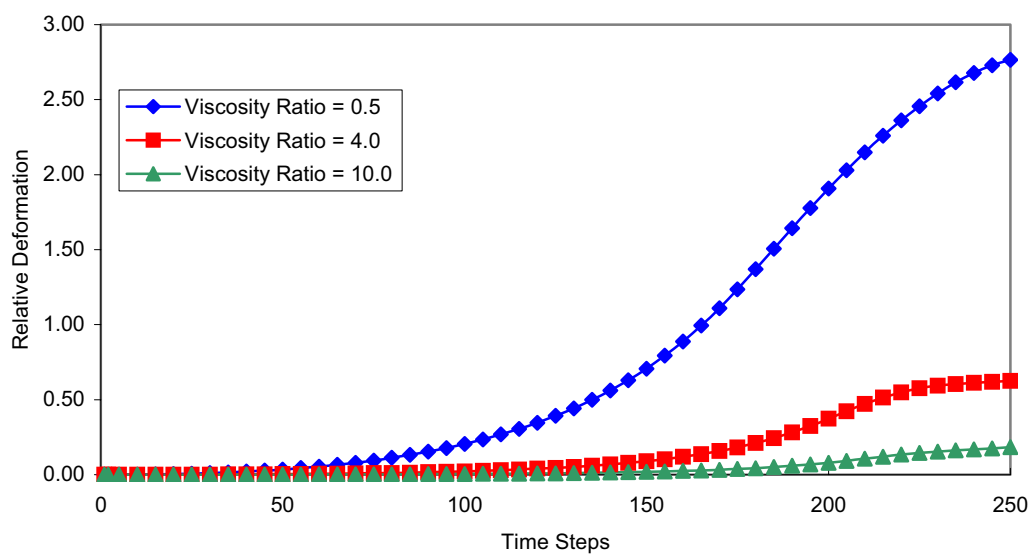


Figure 4 – Relative deformation for drop in converging channel with convergence ratio = 10.

Figure 5 shows the evolution of a drop initially displaced by 0.03mm from the channel centre, for a channel with convergence ratio of 3 and drop–fluid viscosity ratio of 0.5. The drop position is shown after 120, 260, 420, 580 and 800 time steps. It can be seen that the drop elongates and also shears due to the presence of the wall. The drop discretisation after 800 time steps can be seen in figure 6, showing that the elements become concentrated at the pointed ends of the drop. There is a gradual decrease in the length of the elements approaching drop ends.

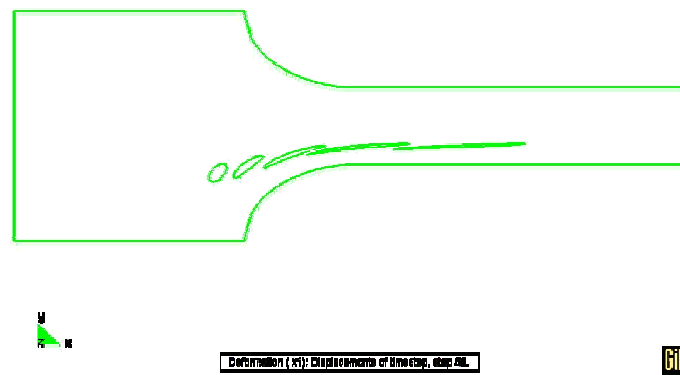


Figure 5 – Evolution of off-centred drop in channel with convergence ratio = 3.

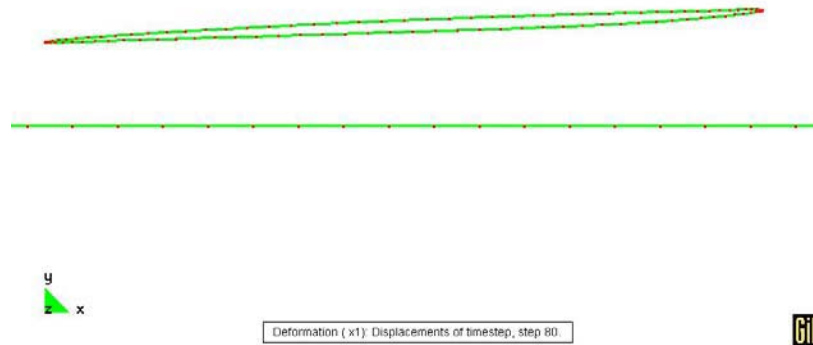


Figure 6 – Drop discretisation after 800 time steps.

## References

- [1] G.G. Stokes, *Transactions of the Cambridge Philosophical Society*, **9**, 8 (1851).
- [2] H. Power and L.C. Wrobel, *Boundary Integral Methods in Fluid Mechanics*, Computational Mechanics Publications (1995).

## The Laplace transform dual reciprocity boundary element method for electromagnetic heating problems

D Crann\*, A J Davies\* and B Christianson†

\*Department of Physics Astronomy and Mathematics, †Department of Computer Science,  
University of Hertfordshire, UK.

**Keywords:** boundary element method, Laplace transform, dual reciprocity method, ohmic heating.

**Abstract.** There are many situations in applied science and engineering where materials are heated electrically via the so-called ohmic heating, or Joule heating, process. In this process the heating occurs throughout the volume as compared with the surface heating in conventional processes. The technique is frequently used as a method of food sterilisation in the food processing industry. It is important to know both that the food material itself is not degraded and that the temperatures reached are sufficient to kill bacteria. These problems exhibit significant non-linearities since, for food materials, the electrical and thermal properties are dependent on the temperature. When the electrical and the thermal conductivity depend on the temperature the resulting model of the ohmic heating process comprises a pair of non-linear coupled partial differential equations. The time dependence can be handled using the Laplace transform by first linearising the equations and solving the system iteratively. The resulting linearised equations may, after taking the Laplace transform, be written in Poisson-type form and as such are ideally-suited to a solution using the dual reciprocity boundary element method. The Laplace transform has been shown to be well-suited to the solution of problems, such as diffusion-type problems, which are parabolic in time. They are transformed to elliptic problems in the space variables and any suitable solver may be used. We shall use the dual reciprocity boundary element method. A numerical inversion of the transform is required and the Stehfest method has been shown to be robust, easy to implement and accurate and that is the approach adopted.

### Introduction

For parabolic problems the most common numerical approach to the solution is to use a finite difference time-stepping process. The Laplace transform in time provides an alternative approach. In both cases the parabolic problem is reduced to an elliptic problem in the space variables and any suitable solver may be used. Rizzo and Shippy [1] first used the Laplace transform in conjunction with the boundary integral equation method using an inversion process in terms of a Prony series of negative exponentials in time. Stehfest's method [2, 3], which is much simpler to apply, was first used by Moridis and Reddell [4]. The solution is developed directly at one specific time value without the necessity of intermediate values. Once the elliptic problem has been solved it remains to invert the Laplace transform. The Stehfest method, as used by Moridis and Reddell [4], is recommended by Davies and Martin [5] in their study of a variety of numerical Laplace transform inversion methods as being simple to use and provides accurate result. Subsequently it has been used in a variety of circumstances by the current authors [6, 7, 8]. A very good account of the Laplace transform technique in a boundary element context is given by Zhu [9]. We describe the use of the Laplace transform with the dual reciprocity boundary element method to solve Poisson-type problems which occur in the ohmic heating of food materials. Satravaha and Zhu [10] describe a similar approach to solve the Poisson-type problem which occurs in the microwave heating of food materials.

### The ohmic heating problem

In the ohmic heating process an electric current generates heat via resistive dissipation in the material. Diffusion and advection provide heat balance with this electrical input. We shall consider problems in a two-dimensional region,  $\Omega$ , bounded by the closed curve  $\Gamma$ .

The underlying equations are described by Please *et al.* [11]:

- (i) the reactive advection-diffusion equation describing heat flow in  $\Omega$ ,

$$\nabla \cdot (k \nabla u) = \frac{\partial}{\partial t} (\rho c u) + \mathbf{v} \cdot \nabla (\rho c u) - \sigma |\nabla \phi|^2, \quad (1)$$

(ii) the generalised Laplace equation describing the electric potential in  $\Omega$ ,

$$\nabla \cdot (\sigma \nabla \phi) = 0, \quad (2)$$

together with suitable boundary conditions on  $\Gamma$ .

At any point  $(x, y)$  and time  $t$ , the dependent variables are the temperature,  $u$  and the electric potential,  $\phi$ . The material parameters are the thermal conductivity,  $k$ , electrical conductivity,  $\sigma$ , the density,  $\rho$ , the specific heat,  $c$  and the velocity of advection,  $\mathbf{v}$ .

The pair of coupled nonlinear partial differential eqs. (1) and (2) has been solved using a finite difference approach by Please *et al.* [11] and a finite element solution is described by de Alwis and Fryer [12] and Elliot and Larsson [13].

The boundary element method provides an alternative to finite differences with the dual reciprocity method to handle the nonlinearities. Equations of the form (1) and (2) have been shown by Partridge *et al.* [14] and by Davies *et al.* [15] to be suitable for a dual reciprocity approach and we shall use the method to solve the coupled problems.

We shall assume that  $\rho$  and  $c$  are constant and that  $k$  and  $\sigma$  depend on  $x, y$  and  $u$ . We re-write the equations as

$$\nabla^2 u = \frac{1}{k} \left( -\nabla k \cdot \nabla u + \rho c \mathbf{v} \cdot \nabla (u) - \sigma |\nabla \phi|^2 + \rho c \frac{\partial u}{\partial t} \right), \quad (3)$$

$$\nabla^2 \phi = \frac{1}{\sigma} (-\nabla \sigma \cdot \nabla \phi). \quad (4)$$

which allows us to use the fundamental solution,  $-\frac{1}{2\pi} \ln R$ , for the Laplacian operator.

### The Laplace transform method

Consider the coupled problem (3) and (4) defined in the two-dimensional region  $\Omega$  bounded by the closed curve  $\Gamma = \Gamma_1 + \Gamma_2$

We require suitable boundary and initial conditions which we shall write as follows:

$$u = u_1(s, t) \text{ and } \phi = \phi_1(s, t) \text{ on } \Gamma_1, \quad (5)$$

$$q \equiv \frac{\partial u}{\partial n} = q_2(s, t) \text{ and } \psi \equiv \frac{\partial \phi}{\partial n} = \psi_2(s, t) \text{ on } \Gamma_2, \quad (6)$$

and the initial condition

$$u(x, y, 0) = u_0(x, y) \text{ and } \phi(x, y, 0) = \phi_0(x, y). \quad (7)$$

Before we can use the Laplace transform we must linearise eqs. (3) and (4) for an iterative approach. Suppose that we use the symbols  $\tilde{u}$  and  $\tilde{\phi}$  to denote values in the previous iteration then we write eqs. (3) and (4) as

$$\nabla^2 u = \frac{1}{k(\tilde{u})} \left( -\nabla k(\tilde{u}) \cdot \nabla u + \rho c \mathbf{v} \cdot \nabla (u) - \sigma(\tilde{u}) |\nabla \tilde{\phi}|^2 + \rho c \frac{\partial u}{\partial t} \right), \quad (8)$$

$$\nabla^2 \phi = \frac{1}{\sigma(\tilde{u})} (-\nabla \sigma(\tilde{u}) \cdot \nabla \phi). \quad (9)$$

We now define the Laplace transform in time by

$$\bar{u}(x, y; \lambda) = \int_0^{\infty} u(x, y, t) e^{-\lambda t} dt,$$

so that the initial boundary-value problem defined by eqs. (8), (9), (5) (6) and (7) becomes

$$\nabla^2 \bar{u} = \frac{1}{k(\tilde{u})} \left( -\nabla k(\tilde{u}) \cdot \nabla \bar{u} + \rho c \mathbf{v} \cdot \nabla (\bar{u}) - \frac{1}{\lambda} \sigma(\tilde{u}) |\nabla \tilde{\phi}|^2 + \rho c (\lambda \bar{u} - u_0) \right), \quad (10)$$

$$\nabla^2 \bar{\phi} = \frac{1}{\sigma(\tilde{u})} (-\nabla \sigma(\tilde{u}) \cdot \nabla \bar{\phi}), \quad (11)$$

subject to the boundary conditions

$$\bar{u} = \bar{u}_1(s, \lambda) \text{ and } \bar{\phi} = \bar{\phi}_1(s; \lambda) \text{ on } \Gamma_1,$$

$$\bar{q} = \bar{q}_2(s; \lambda) \text{ and } \bar{\psi} = \bar{\psi}_2(s; \lambda) \text{ on } \Gamma_2.$$

We shall use the dual reciprocity method to solve the Poisson-type problems (10) and (11) using the Laplacian fundamental solution

$$u^* = -\frac{1}{2\pi} \ln(R). \quad (12)$$

### The dual reciprocity method

We can write eqs. (10) and (11) in the form

$$\nabla^2 \bar{u} = b_1(x, y, \bar{u}, \bar{u}_x, \bar{u}_y; \bar{\phi}, \bar{\phi}_x, \bar{\phi}_y), \quad (13)$$

$$\nabla^2 \bar{\phi} = b_2(x, y, \bar{\phi}, \bar{\phi}_x, \bar{\phi}_y; \bar{u}). \quad (14)$$

The basis of the dual reciprocity method is to expand the domain functions in the form

$$b \approx \sum_{j=1}^{N+L} \alpha_j f_j(R)$$

and find the coefficients  $\alpha$  by collocation:

$$\mathbf{b} = \mathbf{F}\boldsymbol{\alpha}.$$

Davies *et al.* [15] develop the dual reciprocity form of the coupled equations (13) and (14) which may be written:

$$\mathbf{H}\bar{\mathbf{U}} - \mathbf{G}\bar{\mathbf{Q}} = \mathbf{S}\mathbf{b}_1,$$

$$\mathbf{H}\bar{\mathbf{\Phi}} - \mathbf{G}\bar{\mathbf{\Psi}} = \mathbf{S}\mathbf{b}_2,$$

We notice that the domain function,  $b$ , includes partial derivatives of  $\bar{u}$  and  $\bar{\phi}$  which we handle by writing

$$\bar{\mathbf{u}} = \mathbf{F}\boldsymbol{\beta}.$$

Then we have

$$\frac{\partial \bar{\mathbf{u}}}{\partial x} = \frac{\partial \mathbf{F}}{\partial x} \boldsymbol{\beta} = \frac{\partial \mathbf{F}}{\partial x} \mathbf{F}^{-1} \bar{\mathbf{u}}.$$

Following Davies *et al.* [15] we define the matrices

$$\mathbf{K}_1 = \frac{\partial \mathbf{F}}{\partial x} \mathbf{F}^{-1}, \quad \mathbf{K}_2 = \frac{\partial \mathbf{F}}{\partial y} \mathbf{F}^{-1}, \quad \mathbf{C}_1 = \text{diag}[(\rho c v_x)_i], \quad \mathbf{C}_2 = \text{diag}[(\rho c v_y)_i]$$

$$\mathbf{M}_1(\bar{\mathbf{u}}) = \text{diag}[(\mathbf{K}_1 \bar{\mathbf{u}})_i], \quad \mathbf{M}_2(\bar{\mathbf{u}}) = \text{diag}[(\mathbf{K}_2 \bar{\mathbf{u}})_i] \text{ and } \mathbf{Z}_1(\bar{\mathbf{u}}) = \text{diag}\left[-\frac{1}{k(\bar{u}_i)} \frac{dk(\bar{u}_i)}{d\bar{u}_i}\right].$$

Then the discrete forms of  $-\frac{1}{k(\bar{u})} \nabla k(\bar{u}) \cdot \nabla \bar{u}$  ( $= -\frac{1}{k(\bar{u})} \frac{dk(\bar{u})}{d\bar{u}} \nabla \bar{u} \cdot \nabla \bar{u}$ ) and  $\rho c v \cdot \nabla \bar{u}$  are

$$\mathbf{Z}_1(\bar{\mathbf{U}}) [\mathbf{M}_1(\bar{\mathbf{U}}) \mathbf{K}_1 + \mathbf{M}_2(\bar{\mathbf{U}}) \mathbf{K}_2] \bar{\mathbf{U}} \text{ and } [\mathbf{C}_1 \mathbf{K}_1 + \mathbf{C}_2 \mathbf{K}_2] \bar{\mathbf{U}}.$$

We also define

$$\mathbf{Z}_2(\bar{\mathbf{u}}) = \text{diag}[-\sigma(\bar{u}_i)],$$

so that the discrete form of the term  $-\sigma(\bar{u}) |\nabla \bar{\phi}|^2$  may be written

$$\mathbf{Z}_2(\bar{\mathbf{U}}) [\mathbf{M}_3(\bar{\mathbf{\Phi}}) \mathbf{K}_1 + \mathbf{M}_4(\bar{\mathbf{\Phi}}) \mathbf{K}_2] \bar{\mathbf{\Phi}}.$$

Similarly define  $\mathbf{M}_3(\bar{\mathbf{\Phi}}) = \text{diag}[(\mathbf{K}_1 \bar{\mathbf{\Phi}})_i]$  and  $\mathbf{M}_4(\bar{\mathbf{\Phi}}) = \text{diag}[(\mathbf{K}_2 \bar{\mathbf{\Phi}})_i]$ .

Finally we have the discrete form of the domain function  $b_1$  is given by

$$\mathbf{b}_1(\bar{\mathbf{U}}, \bar{\mathbf{U}}, \bar{\mathbf{\Phi}}) = \mathbf{Z}_1(\bar{\mathbf{U}}) [\mathbf{M}_1(\bar{\mathbf{U}}) \mathbf{K}_1 + \mathbf{M}_2(\bar{\mathbf{U}}) \mathbf{K}_2] \bar{\mathbf{U}} + [\mathbf{C}_1 \mathbf{K}_1 + \mathbf{C}_2 \mathbf{K}_2] \bar{\mathbf{U}} \\ + \mathbf{Z}_2(\bar{\mathbf{U}}) [\mathbf{M}_3(\bar{\mathbf{\Phi}}) \mathbf{K}_1 + \mathbf{M}_4(\bar{\mathbf{\Phi}}) \mathbf{K}_2] \bar{\mathbf{\Phi}}.$$

In a similar manner, considering  $-\frac{1}{\sigma(\bar{u})} \nabla \sigma(\bar{u}) \cdot \nabla \bar{u}$  ( $= -\frac{1}{\sigma(\bar{u})} \frac{d\sigma(\bar{u})}{d\bar{u}} \nabla \bar{u} \cdot \nabla \bar{u}$ ), we obtain the discrete form of the domain function  $b_2$  as

$$\mathbf{b}_2(\tilde{\mathbf{U}}, \bar{\Phi}) = \mathbf{Z}_3(\tilde{\mathbf{U}}) \left[ \mathbf{M}_1(\tilde{\mathbf{U}}) \mathbf{K}_1 + \mathbf{M}_2(\tilde{\mathbf{U}}) \mathbf{K}_2 \right] \bar{\Phi}.$$

Finally, the dual reciprocity method leads to the pair of equations of the form

$$\left[ \mathbf{H} - \mathbf{R}_1(\tilde{\mathbf{U}}) \right] \bar{\mathbf{U}} - \mathbf{G} \bar{\mathbf{Q}} = \mathbf{f}(\tilde{\mathbf{U}}, \bar{\Phi}), \quad (15)$$

$$\left[ \mathbf{H} - \mathbf{R}_2(\tilde{\mathbf{U}}) \right] \bar{\Phi} - \mathbf{G} \bar{\Psi} = \mathbf{0}, \quad (16)$$

Equations (16) and (15), after the application of the boundary conditions, may be written in the form

$$\mathbf{A}_1(\tilde{\mathbf{U}}) \mathbf{x} = \mathbf{F}_1(\tilde{\mathbf{U}}) \quad \text{and} \quad \mathbf{A}_2(\tilde{\mathbf{U}}) \mathbf{y} = \mathbf{F}_2(\tilde{\mathbf{U}}, \bar{\Phi}),$$

where

$$\mathbf{x} = \left[ \bar{\Phi}, \bar{\Psi} \right]^T \quad \text{and} \quad \mathbf{y} = \left[ \bar{\mathbf{U}}, \bar{\mathbf{Q}} \right]^T.$$

We define the iterative process

$$\begin{aligned} \mathbf{A}_1(\mathbf{U}^{(q-1)}) \mathbf{x}^{(p)} &= \mathbf{F}_1(\mathbf{U}^{(q-1)}), \\ \mathbf{A}_2(\mathbf{U}^{(q-1)}) \mathbf{y}^{(q)} &= \mathbf{F}_2(\mathbf{U}^{(q-1)}, \Phi^{(p)}), \end{aligned}$$

with  $\mathbf{x}^{(0)}$  and  $\mathbf{y}^{(0)}$  given by the initial conditions.

The stopping condition is given by

$$\frac{\max |x_i^{(p)} - x_i^{(p-1)}|}{\max |x_i^{(p)} + x_i^{(p-1)}|} < \varepsilon \quad \text{and} \quad \frac{\max |y_i^{(q)} - y_i^{(q-1)}|}{\max |y_i^{(q)} + y_i^{(q-1)}|} < \varepsilon,$$

for some suitable tolerance,  $\varepsilon$ .

### Numerical inversion of the Laplace transform

The Stehfest numerical process is implemented as follows:

Choose a specific time value,  $\tau$ , at which we seek the solution and define a discrete set of transform parameters given by

$$\left\{ \lambda_j = j \frac{\ln 2}{\tau} : j = 1, 2, \dots, m; m \text{ even} \right\}.$$

The dual reciprocity method is used for each  $\lambda_j$  to obtain a set of approximate boundary, subscript  $B$ , and internal values, subscript  $I$ :

$$\bar{U}_{B,ij}, \quad i = 1, \dots, N; \quad j = 1, \dots, m, \quad \bar{U}_{I,kj}, \quad k = 1, \dots, L; \quad j = 1, \dots, m.$$

The inverse transforms are then given as follows:

$$U_{B,r} = \frac{\ln 2}{\tau} \sum_{j=1}^m w_j \bar{U}_{B,rj} \quad \text{and} \quad U_{I,r} = \frac{\ln 2}{\tau} \sum_{j=1}^m w_j \bar{U}_{I,rj},$$

where  $r = 1 \dots N$  for boundary points and  $r = 1 \dots L$  for internal points.

The weights,  $w_j$ , are given by Stehfest [2, 3] as

$$w_j = (-1)^{\frac{m}{2}+j} \frac{\sum_{k=\lfloor \frac{1}{2}(1+j) \rfloor}^{\min(j, \frac{m}{2})} k^{\frac{m}{2}} (2k)!}{\left(\frac{m}{2} - k\right)! k! (k-1)! (j-k)! (2k-j)!}.$$

### Results

In problems in the food processing industry a good model for the thermophysical properties is that the heat capacity,  $\rho c$ , is constant and the conductivities are both linear with temperature.

Consequently we shall consider the following model problem, where we choose the functions  $h_1(x, y, t)$  and  $h_2(x, y, t)$  so that we have a known analytic solutions  $u = \left(x - \frac{1}{2}x^2\right)(2 - e^{-t})$  and  $\phi = x + (x - x^2)e^{-t}$ :

We seek a solution, in the region  $\{(x, y) : 0 < x < 1, 0 < y < 1\}$ , to the initial boundary-value problem

$$\nabla \cdot (k \nabla u) = \frac{\partial}{\partial t} (\rho c u) + \mathbf{v} \cdot \nabla (\rho c u) - \sigma |\nabla \phi|^2 + h_1(x, y, t),$$

$$\nabla \cdot (\sigma \nabla \phi) = 0 + h_2(x, y, t),$$

$$\text{with } \rho c = 1, \mathbf{v} = \mathbf{i}, k(u) = 1 + u, \sigma(u) = 1 + u,$$

subject to the boundary conditions

$$u = 0 \text{ on } x = 0, \frac{\partial u}{\partial n} = 0 \text{ on } x = 1, y = 0, y = 1, \phi = 0 \text{ on } x = 0, \phi = 1 \text{ on } x = 1, \frac{\partial \phi}{\partial n} = 0 \text{ on } y = 0, y = 1$$

and the initial conditions

$$u(x, y, 0) = x - \frac{1}{2}x^2 \text{ and } \phi(x, y, 0) = 2x - x^2.$$

We use linear elements with 10 Gauss points in the numerical quadrature and we use  $f_j(R) = 1 + R$  in the dual reciprocity approximation. For the numerical solution we choose  $N = 32, L = 9, m = 8$ . We use a tolerance  $\varepsilon = 0.001$ .

The space distribution for time values  $t = 0.1, 0.5, 1, 5$  is shown in Figs. 1 and 2 and the time development for values  $x = 0.2, 0.5, 0.8$  is shown in Figs. 3 and 4. We note here that the solution is independent of  $y$ .

We see that the approximate solution compares very well with the analytic values, typical errors being of the order of about three percent for  $\phi$  and about four percent for  $u$ . Typically we need approximately four iterations to achieve convergence within tolerance for both the  $p$  and  $q$  cycles.

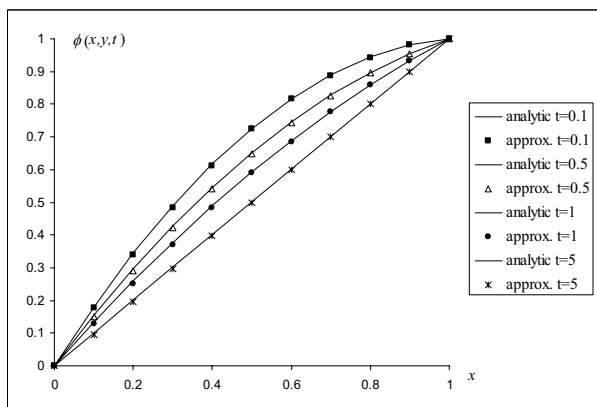


Fig. 1. Space distribution of  $\phi(x, y, t)$ .

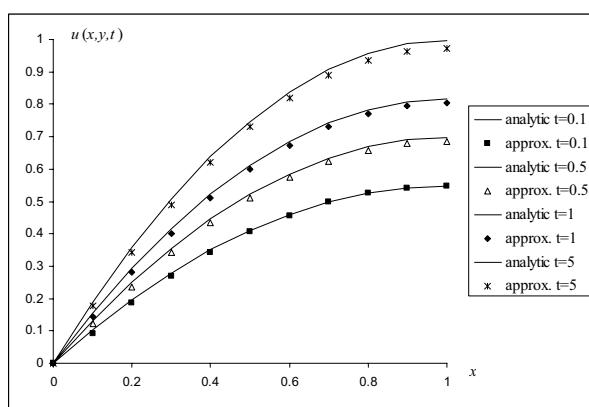


Fig. 2. Space distribution of  $u(x, y, t)$ .

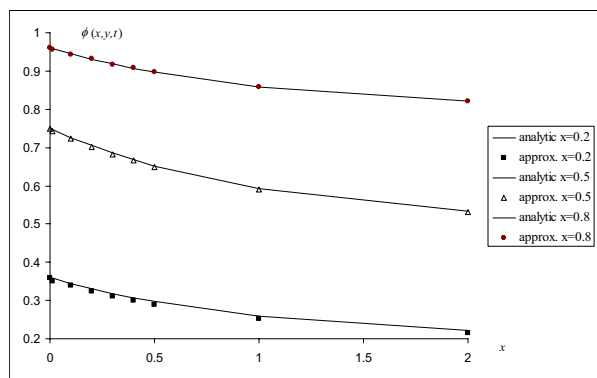


Fig. 3. Time development of  $\phi(x, y, t)$ .

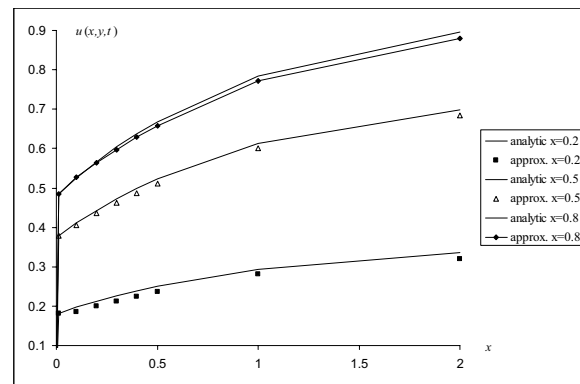


Fig. 4. Time development of  $u(x, y, t)$ .

### Conclusions

In this initial study we have shown that the Laplace transform dual reciprocity method provides a suitable technique for solving coupled nonlinear Poisson-type problems such as those which occur in ohmic heating. The problems are of particular interest in the food processing industry where the functional form of the thermal and electrical conductivities are similar to those in this study. The advantage of the Laplace transform method compared with a finite difference in the time variable is that there is no need to compute intermediate solutions in a time-marching sense and there are no stability problems to be considered. However, there is the necessity to find a suitable linearisation which leads to a convergent solution in the transform domain. No such linearisation procedure is needed with finite differences but a solution of a nonlinear system of equations is required at each stage. A feature for future work will be to consider a detailed comparison of the two solution schemes. Real problems are likely to have significantly more complicated geometry and food products frequently contain multi-phase materials. The geometry should cause little difficulty because the boundary element method is ideally suited to handling complex geometry. Multi-phase problems offer a more significant challenge but domain decomposition approaches [16, 17] offer a possible way forward.

### References

- [1] Rizzo FJ and Shippey DJ. A method of solution of certain problems of transient heat conduction, *AIAA Journal*, **8**, 2004-2009, 1970.
- [2] Stehfest H. Numerical inversion of Laplace transforms, *Comm. ACM.*, **13**, 47-49, 1970.
- [3] Stehfest H. Remarks on Algorithm 368 [D5] Numerical inversion of Laplace transforms, *Comm. ACM.*, **13**, 624, 1970.
- [4] Moridis GJ and Reddell DL. The Laplace transform boundary element (LTBE) numerical method for the solution of diffusion-type problems, *Boundary Elements XIII*, 83-97, 1991.
- [5] Davies B and Martin B. Numerical inversion of Laplace transforms: A survey and comparison of methods, *J. Comput. Phys.*, **33**, 1-32, 1979.
- [6] Honnor ME and Davies AJ. The Laplace transform dual reciprocity boundary element method for nonlinear transient field problems, *Boundary Elements XXIV*, 363-372, 2002.
- [7] Davies AJ, Mushtaq J, Radford LE and Crann D. The numerical Laplace transform solution method on a distributed memory architecture, *Applications of High Performance Computing in Engineering V*, 245-254, 1997.
- [8] Crann D, Davies AJ and Mushtaq J. Parallel Laplace transform boundary element methods for diffusion problems, *Boundary Elements XX*, 259-268, Computational Mechanics Press, 1998.
- [9] Zhu S-P. Time-dependent reaction-diffusion problems and the LTDRM approach, *Boundary Integral methods, Numerical and Mathematical Aspects*, ed. Golberg M., 1-35, Computational Mechanics Publications, 1999.
- [10] Satravaha P and Zhu S. An application of the LTDRM to transient diffusion problems with nonlinear material properties and nonlinear boundary conditions, *Appl. Math. Comp.*, **87**, 127-160, 1997.
- [11] Please CP, Schwendeman DW and Hagan PS. Ohmic heating of foods during aseptic processing, *IMA J. Maths Appl. Bus. & Ind.*, **5**, 283-301, 1995.
- [12] de Alwis AAP and Fryer PJ. A finite element analysis of heat generation in the food industry, *Chem. Eng. Sci.*, **45**, 1547-1549, 1990.
- [13] Elliot CM and Larsson S. A finite element model for the time-dependent Joule heating problem, *Maths Comp.*, **64**, 1433-1453, 1995.
- [14] Partridge PW, Brebbia CA and Wrobel LC. *The dual reciprocity method*, Computational Mechanics Publications, 1992.
- [15] Davies AJ, Toutip W and Bartholomew-Biggs MC. The dual reciprocity method for coupled thermal/electromagnetic problems, *Boundary Element Technology XIV*, 371-380, 2001.
- [16] Davies AJ and Mushtaq J. Parallel implementation of the boundary element method using PVM and HPF on a collection of networked workstations. *Applications of High Performance Computing V*, 181-188, 1997
- [17] Popov V and Power H. The DRM-MD integral equation method: an efficient approach for the numerical solution of domain dominant problems, *Int. J. Numer. Meth. Engng.*, **44**, 327-353, 1999.

## BOUNDARY ELEMENT METHODS FOR INFILTRATION FROM IRRIGATION CHANNELS

M. Lobo and D.L. Clements

Department of Applied Mathematics, The University of Adelaide

SA 5005, Australia

mlobo@maths.adelaide.edu.au

dclement@maths.adelaide.edu.au

**Keywords:** Boundary element method, Infiltration, Irrigation.

**Abstract**—In this paper some applications of Boundary Element Techniques are considered for the solution of two dimensional problems concerning infiltration from irrigation channels into an unsaturated soil. The problems involve infiltration from periodic irrigation channels of various shapes, infiltration from periodic channels into a soil which contains impermeable inclusions or impermeable sheets and infiltration from a single channel. For each case, an appropriate procedure is employed to reduce the problem to a boundary integral equation which can be solved numerically. Numerical results are obtained to provide the distribution of the matric flux potential throughout the soil. The results gives an indication of how the various shapes of irrigation channels as well as the length, number and the depth of impermeable layers influences the distribution of water in an irrigated area.

### Introduction

Problems involving steady infiltration from single or periodic irrigation channels have been considered by a number of authors (see for example Gardner [1], Batu [2], Pullan and Collins [3] and Basha [4]). In particular, Pullan and Collins [3] used the boundary element technique to consider some particular infiltration problems concerning infiltration from surface channels into a homogenous soil. The purpose of the present paper is to outline the application of boundary element techniques for the solution of problems involving infiltration from irrigation channels into a soil which contains impermeable obstacles.

An appropriate procedure is employed to reduce the problem to a boundary integral equation which is then used to compute the distribution of the matric flux potential throughout the soil. Some particular examples are considered to indicate the influence of the various shapes of irrigation channels and impermeable inclusions as well as the number and the depth of the impermeable layers on infiltration from irrigation furrows.

### Basic Equations

In terms of the matric flux potential  $\Theta$  the equation for steady flow in an unsaturated homogeneous porous media is

$$\frac{\partial^2 \Theta}{\partial X^2} + \frac{\partial^2 \Theta}{\partial Z^2} = \alpha \frac{\partial \Theta}{\partial Z} \quad (1)$$

(see (Batu [2]) where  $X$  and  $Z$  are Cartesian coordinates (see Figure 1).

The horizontal and vertical components of the flux and the flux normal to the surface with

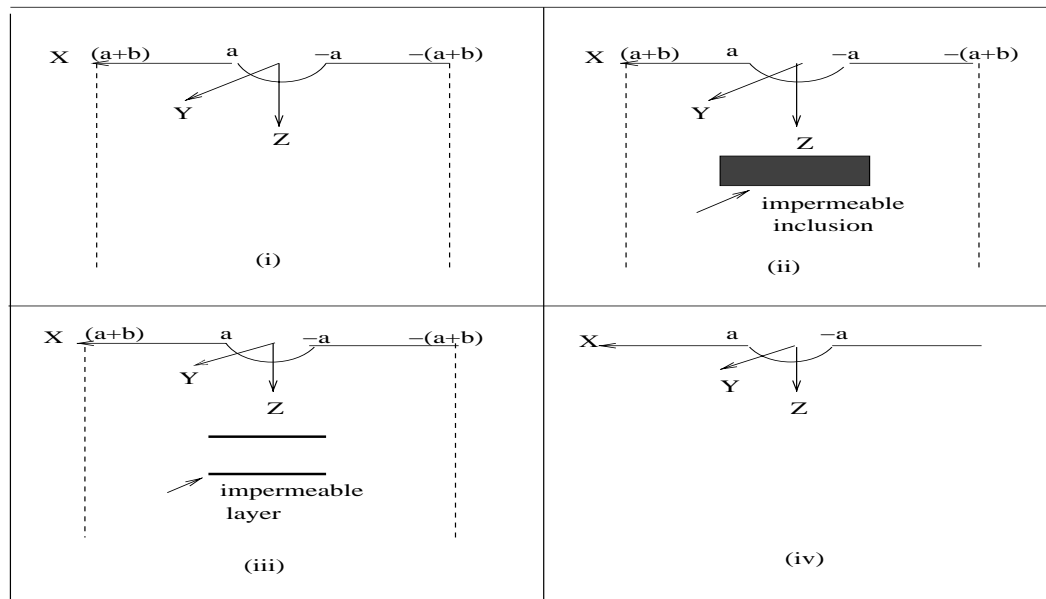


Figure 1: Illustration of the physical problem

outward pointing normal  $\mathbf{n} = (n_1, n_2)$  are given by

$$U = -\frac{\partial\Theta}{\partial X}, \quad V = \alpha\Theta - \frac{\partial\Theta}{\partial Z} \quad \text{and} \quad F = -\frac{\partial\Theta}{\partial X}n_1 + (\alpha\Theta - \frac{\partial\Theta}{\partial Z})n_2. \quad (2)$$

Dimensionless variables are now defined in the form

$$\theta = \frac{1}{V_0L}\Theta, \quad x = \frac{\alpha}{2}X, \quad z = \frac{\alpha}{2}Z, \quad u = \frac{2}{V_0\alpha L}U, \quad v = \frac{2}{V_0\alpha L}V \quad \text{and} \quad f = \frac{2}{V_0\alpha L}F, \quad (3)$$

where  $V_0$  is a reference flux per unit length,  $\alpha$  is an empirical constant and  $L$  is a reference length. In terms of these variables with  $\theta = e^z\Psi$  equations (1) and (2) yield

$$\frac{\partial^2\Psi}{\partial x^2} + \frac{\partial^2\Psi}{\partial z^2} - \Psi = 0, \quad (4)$$

and

$$u = -e^z\frac{\partial\Psi}{\partial x}, \quad v = e^z\left(\Psi - \frac{\partial\Psi}{\partial z}\right), \quad f = -e^z\left[\frac{\partial\Psi}{\partial n} - \Psi n_2\right] \quad \text{and} \quad \frac{\partial\Psi}{\partial n} = \Psi n_2 - e^{-z}f. \quad (5)$$

On the soil surface outside the channel the normal flux is zero so that

$$\Psi - \frac{\partial\Psi}{\partial z} = 0 \quad \text{for} \quad z = 0 \quad (6)$$

and the normal flow over the surface of the channel is

$$-\left[\frac{\partial\Psi}{\partial x}n_1 - \left(\Psi - \frac{\partial\Psi}{\partial z}\right)n_2\right] = -\exp(z)f_0(x, z), \quad (f_0 \text{ given}). \quad (7)$$

For periodic channels (see Figure 1(i, ii and iii)) there is also a condition of no flow perpendicular to the vertical planes having abscissas  $X = 0, \pm(2m-1)(a+b)$  for  $m = 1, 2, 3, \dots$  where  $2L$  is the surface length of the channel,  $a = 2L/\pi$  and  $2b$  is the distance between the channels, so that from equation (5)

$$\frac{\partial\Psi}{\partial x} = 0, \quad \text{for} \quad z > 0 \quad \text{and} \quad x = \pm\alpha(a+b)/2. \quad (8)$$

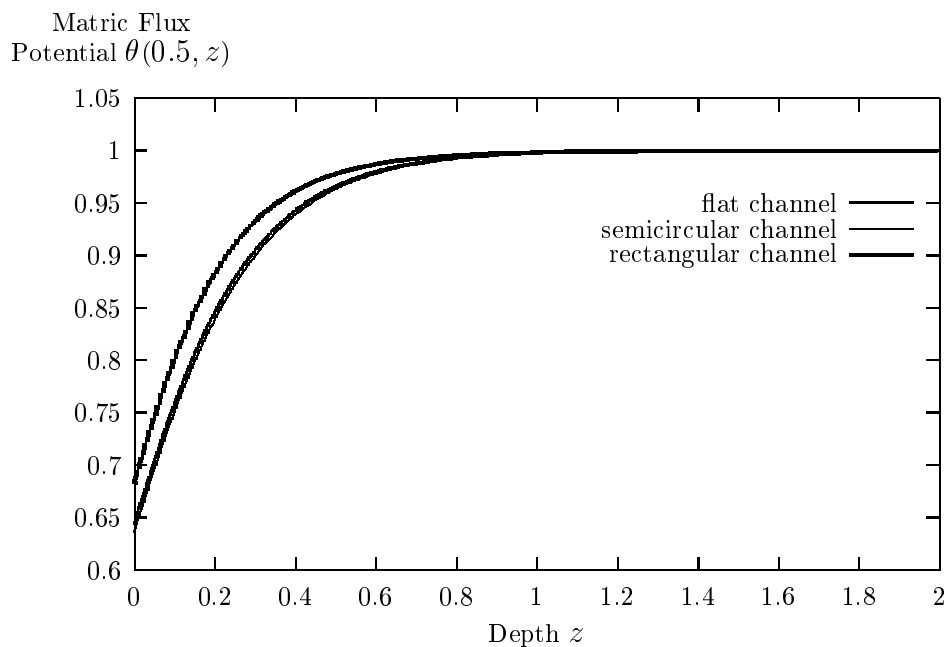


Figure 2: Values of  $\theta$  along the boundary line  $x = 0.50$  from various channel shapes

### Infiltration from Periodic Channels into a Homogenous Soil

The boundary integral equation for the solution to equation (4) is

$$\lambda\Psi(\zeta, \eta) = - \int_{\partial\Omega} \left[ \frac{\partial\Psi}{\partial n} \phi' - \frac{\partial\phi'}{\partial n} \Psi \right] dS, \quad (9)$$

where  $\mathbf{n} = (n_1, n_2)$  is the outward pointing normal to  $\Omega$  (where  $\Omega$  denotes the domain of the problem),  $\lambda = 1$  if  $(\zeta, \eta) \in \Omega$  and  $\lambda = 1/2$  if  $(\zeta, \eta) \in \partial\Omega$  and  $\partial\Omega$  has a continuously turning tangent. In the case of equation (4) the  $\phi'$  in equation (9) is

$$\phi'(x, z; \zeta, \eta) = -\frac{1}{2\pi} K_0(r) \quad (10)$$

where  $r = ((x - \zeta)^2 + (z - \eta)^2)^{1/2}$  and  $K_0$  is a modified Bessel function.

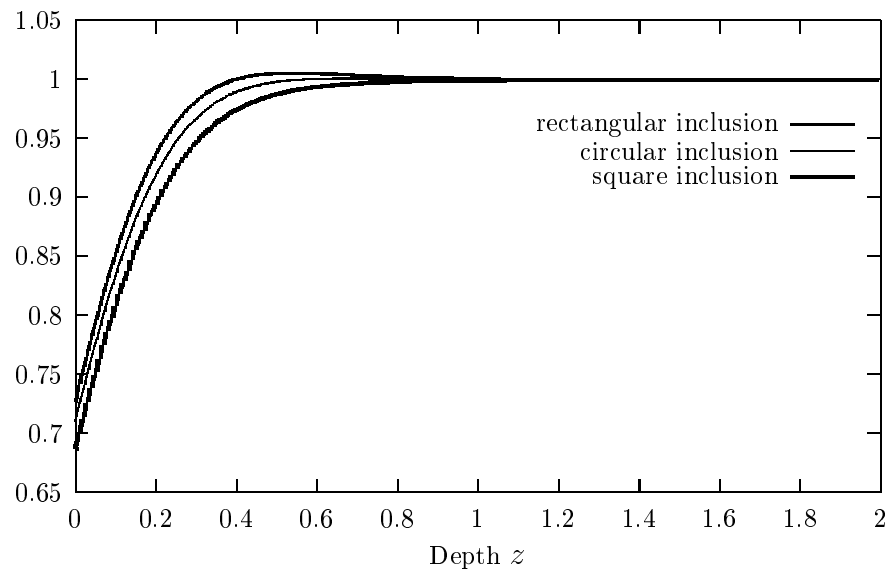
Substitution of  $\partial\Psi/\partial n$  in equation (5) into (9) gives

$$\lambda\Psi(\zeta, \eta) = - \int_{\partial\Omega} \left[ \phi' n_2 - \frac{\partial\phi'}{\partial n} \right] \Psi dS + \int_{\partial\Omega} f e^{-z} \phi' dS. \quad (11)$$

The boundary integral equation (11) is used to determine the matric flux potential for a variety of configurations for the irrigation channels. The reference length  $L$  is taken to be 100 cm and  $\alpha = 0.002 \text{ cm}^{-1}$  (see Batu [2]) so that  $\alpha L = 0.2$  which yields  $f = -10$  when the normal flux is chosen to be constant  $F = -V_0$ . Therefore the radius of the semi-circular channel is  $\alpha L/\pi = 0.06366$  and the coordinates  $(x, z)$  of the corners of the rectangular channel are  $(-0.1, 0)$ ,  $(-0.1, 0.1)$ ,  $(0.1, 0.1)$  and  $(0.1, 0)$ . Also  $\alpha(a + b)/2$  is taken to be 0.5.

To obtain the numerical values from equation (11) standard boundary element methods were employed. The value of  $\Psi$  is then transformed back to get the dimensionless values of the matric flux potential  $\theta$ .

The results in Figure 2 show that the matric flux potential is not greatly altered by replacing the flat channel by a semi-circular channel. In contrast replacement of the flat channel by a rectangular ditch gives increased values for the matric flux potential along the line  $x = 0.5$ .

Figure 3: Values of  $\theta$  along the boundary line  $x = 0.50$ 

### Infiltration from Periodic Channels into a Soil with Impermeable Inclusions

Here equation (11) is employed with the integration taken along the outer boundary as well as the boundary of the inclusions along which the normal flux is zero.

The inclusions are placed in the soil as shown in Figure 1(ii) at a depth of  $Z = \beta L$ , where  $\beta$  is a dimensionless parameter. When  $\beta = 2.5$  the inclusion is centered at  $(x, z) = (0.0, 0.25)$  with the radius of the circle 0.1 and the sides of the square 0.1771 while the rectangle is 0.2 in length in the  $0x$  direction and 0.1570 in width in the  $0z$  direction.

Figure 3 describes the value of the dimensionless matric flux potential  $\theta$  from periodic channels embedded with various shapes of impermeable inclusions of the similar area. From the graph it is apparent that, for the inclusions considered the highest value of the matric flux potential ( $\theta = 1.0052$  on  $z$  between 0.53 and 0.54) occurs when a rectangular inclusion is placed underneath the irrigation channel.

### Infiltration from Periodic Channels into a Soil with Impermeable Layers

In this section we determine the matric flux potential for periodic semi-circular channels with  $N$  impermeable layers of lengths  $L^{(1)}, L^{(2)}, \dots, L^{(N)}$ . There is no flow across the impermeable layers so that if  $\mathbf{n}^{(j)} = (n_1^{(j)}, n_2^{(j)})$  denotes the normal to the  $j$ th impermeable layer then for  $(x, z)$  on the  $j$ th impermeable layers (5) provides

$$n_2^{(j)}\Psi(\zeta, \eta) - \frac{\partial\Psi}{\partial n^{(j)}} = 0 \quad \text{for } j = 1, 2, \dots, N. \quad (12)$$

The solution of this boundary value problem is achieved by modifying the boundary integral equation (11) in order to include the impermeable layer. Specifically

$$\begin{aligned} \lambda\Psi(\zeta, \eta) = & - \int_{\partial\Omega} [P(x, z); \phi'(x, z; \zeta, \eta) - \Lambda(x, z; \zeta, \eta; n_1, n_2)\Psi(x, z)] dS(x, z) \\ & + \sum_{i=1}^N \frac{L^{(i)}}{2} \int_{-1}^1 [X^{(i)}(t), Z^{(i)}(t); \zeta, \eta; n_1^{(i)}, n_2^{(i)} - n_2^{(i)}\phi'(X^{(i)}(t), Z^{(i)}(t); \zeta, \eta)] \Delta w^{(i)}(t) dt \end{aligned} \quad (13)$$

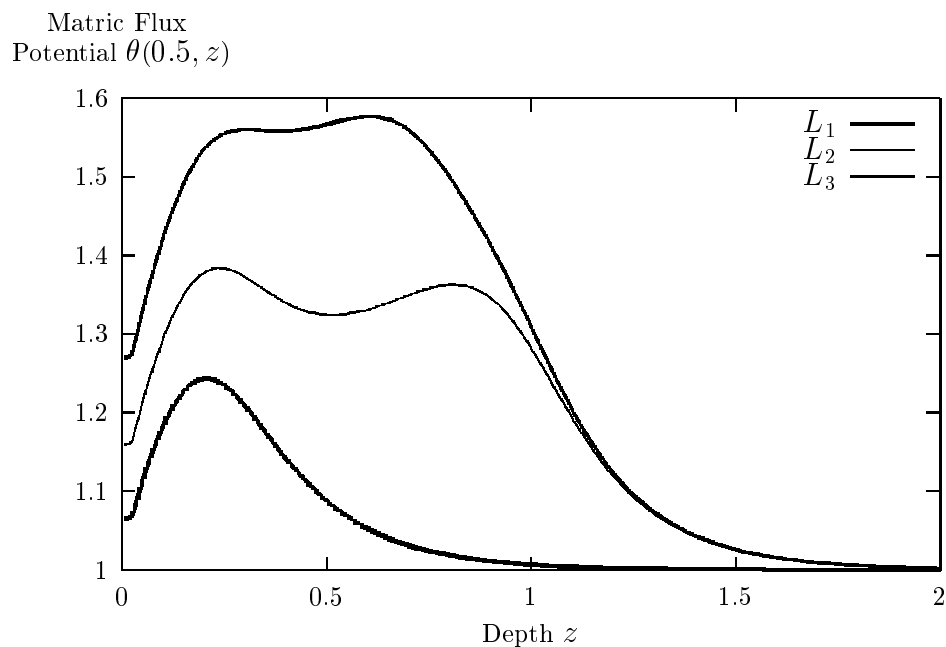


Figure 4: Values of  $\theta$  for a single layer, two layers and three layers

where

$$P(x, z) = n_2 \Psi - f e^z, \quad \phi'(x, z; \zeta, \eta) = -\frac{1}{2\pi} K_0(r), \quad \Lambda(x, z; \zeta, \eta) = \frac{\partial \phi'}{\partial n} \quad (14)$$

and

$$\Delta w^{(i)}(t) \simeq \sqrt{(1-t^2)} \sum_{k=1}^{J^{(i)}} \alpha_k^{(i)} U_{k-1}(t) \quad (15)$$

where  $U_k(t)$  denotes the Chebyshev polynomial of the second kind and  $\alpha_k^{(i)}$  for  $i = 1, \dots, N$  and  $k = 1, \dots, J^{(i)}$  are unknowns.

The integration along the outer boundary of the domain is performed in the similar manner to previous section whereas as  $(\zeta, \eta)$  approaches the  $i$ th impermeable layer the integral over the layer is interpreted as a Cauchy principal value integral. Therefore differentiation of this integral (with respect to either  $\zeta$  or  $\eta$ ) as  $(\zeta, \eta)$  approaches the impermeable layer leads to a Hadamard finite-part integral. The Hadamard finite-part integral is evaluated using a formula in Kaya and Erdogan [5].

$L_q$  for  $q = 1, 2, 3$  denotes the number of layers embedded in the region (see Figure 1(iii)). In this problem all the layers have the same length (0.6) in the  $0x$  direction and are placed at 0.25, 1.0, 0.75 in the  $0z$  direction for layer 1, 2 and 3 respectively. Figure 4 illustrates the effect of increasing the number of impermeable layers on the distribution of the matric flux potential  $\theta$  along the line  $x = 0.5$ . The graph indicates how the introduction of the additional impermeable layers provides higher values of matric flux potential along the line  $x = 0.5$ .

### Infiltration from a Single Channel and a Double Channel

In this section we consider the flow from a single semi-circular channel and two semi-circular channels in a semi-infinite soil. A Green's function derived by Basha [4] is used in the boundary integral equation (11). The Green's function takes the form

$$\phi'(x, z; \zeta, \eta) = -\frac{1}{2\pi} [K_0(r) + K_0(\bar{r})] + \frac{1}{\pi} e^z \int_z^\infty e^{-\mu} K_0 \left( \left[ (x-a)^2 + (\mu+b)^2 \right]^{\frac{1}{2}} \right) d\mu \quad (16)$$

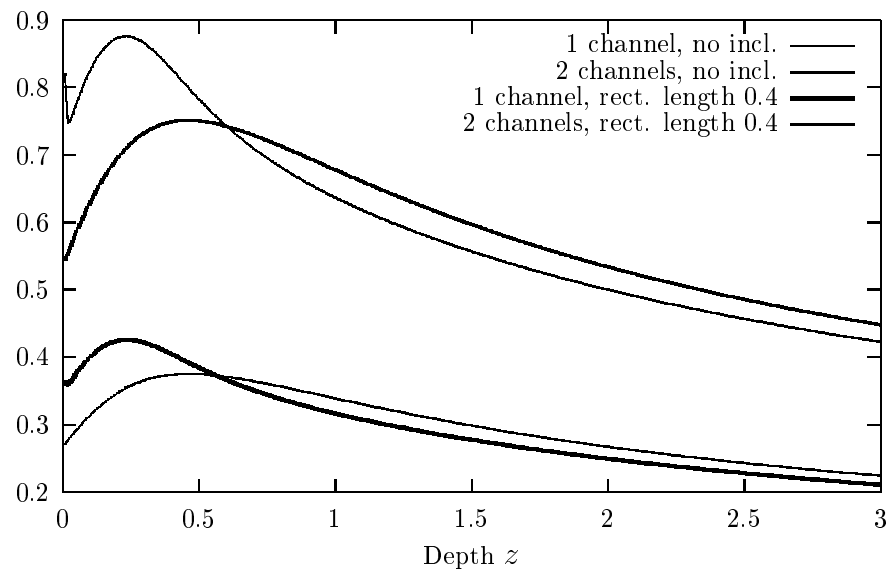


Figure 5: The value of the matric flux potential  $\theta$  at  $x = 0.5$  for single channel and double semi-circular channels

where  $\bar{r} = ((x - \zeta)^2 + (z + \eta)^2)^{\frac{1}{2}}$ .

This Green's function is such that  $\phi' - \partial\phi'/\partial z = 0$  on  $z = 0$  and since the flux is zero on  $z = 0$  outside the channel then equation (11) reduces to

$$\lambda\Psi(\zeta, \eta) = - \int_{\partial\Omega_1} \left[ \phi' n_2 - \frac{\partial\phi'}{\partial n} \right] \Psi dS + \int_{\partial\Omega_1} f e^{-z} \phi' dS \quad (17)$$

where  $\partial\Omega_1$  denotes the boundary of the channels. From equation (17) it is clear that the numerical integration is only undertaken along the surface of the channel.

For the single channel case the inclusion is centered at  $(x, z) = (0.0, 0.25)$  and is of length 0.4 in the  $0x$  direction and 0.0785 in the  $0z$  direction. For the double channel case a similar inclusion is placed under the second channel.

Figure 5 provides the matric flux potential for a single and a double semi-circular channel with and without rectangular impermeable inclusions.

## References

- [1] W. R. Gardner, Some Steady State Solutions of the Unsaturated Moisture Flow Equation with Application to Evaporation from a Water Table. *Soil Science*. **85**, 228–232 (1957).
- [2] V. Batu, Steady Infiltration from Single and Periodic Strip Sources. *Soil Science Society of America Journal*. **42**, 545–549 (1978).
- [3] A. J. Pullan and I. F. Collins, Two- and Three-Dimensional Steady Quasi-Linear Infiltration from Buried Surface Cavities using Boundary Element Techniques. *Water Resources Research*. **23**, 1633–1644 (1987).
- [4] H.A.Basha, Multidimensional Steady Infiltration with Prescribed Boundary Conditions at the Soil Surface, *Water Resources Research* **30**, 2105-2118 (1994).
- [5] A. C. Kaya and F. Erdogan, On The Solution of Integral Equations with Strongly Singular Kernels, *Quart. Appl. Maths*. **45**, 105-122 (1987).

## The Trefftz Method for Solving Laplace Eigenvalue Problems

Zi-Cai Li<sup>1</sup>, Tzon-Tzer Lu<sup>1</sup> and Heng-Shuing Tsai<sup>1</sup>

<sup>1</sup>Department of Applied Mathematics and Department of Computer Science and Engineering,  
National Sun Yat-sen University Kaohsiung, Taiwan 80424,  
and National Center for Theoretical Science, Mathematics Division, Taiwan.  
E-mail: zcli@math.nsysu.edu.tw.

**Keywords:** The Trefftz method, Laplace eigenvalue problems, Helmholtz equation, interfaces, the L-shaped domain, the cracked beam, nonlinear solutions.

**Abstract.** For Laplace eigenvalue problems, this paper presents new algorithms of the Trefftz method (i.e. the boundary approximation method), which solve the Helmholtz equation and then use an iteration process to yield approximate eigenvalues and eigenfunctions. The new iterative method has superlinear convergence rates and gives a better performance in numerical testing, compared with the other popular methods of rootfinding. Moreover, piecewise particular solutions are used for a basic model of eigenvalue problems on the unit square with the Dirichlet condition. Numerical experiments are also carried out for two eigenvalue problems with singularities, one on the L-shaped domain, and the other of the cracked beam. Our new algorithms using piecewise particular solutions are well suited to seek very accurate solutions of eigenvalue problems, in particular those with multiple singularities, interfaces and those on unbounded domains. Using piecewise particular solutions also has the advantage to solve complicated problems because uniform particular solutions may not always exist for the entire solution domain. This paper may be regarded as a development of Fox, Henrici and Moler [2] by using the uniform particular solutions over the entire domain.

**1 Introduction.** For solving eigenvalue problems, there exist a number of numerical methods and their parallel implementation. We will follow [4, 5, 6] to employ the boundary approximation method (BAM), i.e., the Trefftz method (TM) [8] called in engineering journals and in this paper. In the TM, the solution domain is divided into several subdomains, different particular solutions on subdomains (i.e., piecewise particular solutions) are used, and an approximation of the solution is then obtained by satisfying only the interior and exterior boundary conditions. An important advantage of the TM is that high accuracy of solutions can be achieved with a modest effort in computation.

In this paper, we seek the eigenvalues  $\lambda_l$  and the nonzero eigenfunction  $\phi_l$  satisfying

$$\begin{cases} -\Delta\phi_l = \lambda_l\phi_l, & \text{in } \Omega, \\ \phi_l = 0, & \text{on } \Gamma, \end{cases} \quad (1)$$

where  $\Delta = \frac{\partial^2}{\partial x^2} + \frac{\partial^2}{\partial y^2}$ , and  $\Omega$  is a polygonal domain with the external boundary  $\Gamma$ . For simplicity, only the Dirichlet boundary condition is described here; other boundary conditions are treated in Sections 3-5 (also see [4, 5, 6]). Denote the eigenvalues in an ascending order:

$$0 < \lambda_1 \leq \lambda_2 \leq \dots \leq \lambda_l \leq \dots, \quad \lambda_1 = \lambda_{min}. \quad (2)$$

The eigenfunctions will satisfy the orthogonality property:

$$(\phi_i, \phi_j) = \int \int_{\Omega} \phi_i \phi_j d\Omega = \delta_{ij} = \begin{cases} 1, & i = j, \\ 0, & i \neq j. \end{cases} \quad (3)$$

Let the solution domain  $\Omega$  be divided into two subdomains,  $\Omega^+$  and  $\Omega^-$ , by a piecewise straight line

$\Gamma_0$ . Then the eigenfunction  $\phi_l$  must satisfy the continuity conditions across the interface  $\Gamma_0$ :

$$\begin{cases} -\Delta\phi_l = \lambda_l\phi_l, & \text{in } \Omega^+ \text{ and } \Omega^-, \\ \phi_l^+ = \phi_l^-, \quad \frac{\partial\phi_l^+}{\partial\nu} = \frac{\partial\phi_l^-}{\partial\nu}, & \text{on } \Gamma_0, \\ \phi_l = 0, & \text{on } \Gamma, \end{cases} \quad (4)$$

where  $\nu$  is the unit normal vector to  $\Gamma_0$ .

Let us first recall from Ortega [7], p.40, that the matrix eigenvalue problem  $A\vec{x} = \lambda\vec{x} (\lambda > 0)$  can be solved by solving the linear algebraic equations,

$$(A - k^2I)\vec{x} = \vec{b}, \quad (5)$$

where  $I$  is the identity matrix,  $k(> 0)$  is chosen, and  $\vec{b}$  is a nonzero vector. If (5) is ill-conditioned (called degeneracy in this paper), then  $k^2$  and  $\vec{x}$  can be regarded approximately as an eigenvalue and its corresponding eigenvector of matrix  $A$ . Note that the nonzero vector  $\vec{b}$  can be chosen rather arbitrarily, but not necessarily to be small.

Analogously, for solving (4), we may seek the following Helmholtz solutions instead

$$\begin{cases} -\Delta u = k^2u, & \text{in } \Omega^+ \text{ and } \Omega^-, \\ u^+ = u^-, \quad \frac{\partial u^+}{\partial\nu} = \frac{\partial u^-}{\partial\nu}, & \text{on } \Gamma_0, \\ u|_{\Gamma} = g, \end{cases} \quad (6)$$

where  $k > 0$ ,  $g \in H^{\frac{1}{2}}(\Gamma)$  is a given nonzero function, and  $H^{\frac{1}{2}}(\Gamma)$  is the Sobolev space on  $\Gamma$ . Consequently, when  $k$  is suitably chosen so as to lead to a degeneracy (or ill-conditioning) of (6),  $k^2$  and  $u$  can be regarded approximately as an eigenvalue and its corresponding eigenfunction of (4).

Define the smallest relative distance between  $k^2$  and  $\lambda_i$  by

$$\delta = \min_i \left| \frac{k^2 - \lambda_i}{\lambda_i} \right|. \quad (7)$$

When  $k$  approaches one of  $\lambda_i$ , the solution  $u$  of (6) will approach an eigenfunction [2]. Besides, when  $k^2 = \lambda_\ell$  (*i.e.*,  $\delta = 0$ ) and  $u = \phi_\ell$ , the non-homogeneous term  $g$  must be zero. It seems to be a paradox due to the assumption  $g \neq 0$  in (6). How can we clarify this paradox? In practical computation, we have either  $\delta > 0$  or  $u \neq \phi_\ell$  due to rounding errors in computer or truncation errors in numerical algorithms. So, the equation (6) could be very ill-conditioned, but never be exactly singular. Therefore, the Helmholtz solutions can be solved by some numerical methods, *e.g.*, by the Trefftz method [4, 5, 6]. Surprisingly, such a degeneracy of (6) can lead to a very high accuracy of eigenvalues and eigenfunctions by the new algorithms developed in this paper. In fact, it is just due to such a degeneracy of matrix  $(A - k^2I)$  that the inverse power method works well, see [7], p.40. Moreover, the new algorithms for (6) and numerical experiments in this paper display that such a degeneracy of (6) may grant a very high accuracy of eigenvalues and eigenfunctions in (4) by the new algorithms developed.

The full paper is organized as follows. In Section 2, we present new algorithms, and in Section 3, we carry out a simple eigenvalue problem to display the effectiveness of the proposed algorithms. In Sections 4 and 5, numerical experiments are carried for the eigenvalue problems on an L-shaped domain with the Dirichlet condition, and those of the cracked beam. In the last section, summaries and discussions are given.

**2 New Algorithms.** Based on the above ideas that a degeneracy of (6) implies the infinitesimal values of  $\lambda_{\min}(A(k))$ , we propose Algorithms (A) and (B).

Suppose  $k^2 = \lambda_l$ , i.e.,  $\delta = 0$  defined in (7). Then  $u_{m,n} \rightarrow \phi_l$  as  $m \rightarrow \infty$  and  $n \rightarrow \infty$ , since the eigenfunctions  $\phi_l$  can be expressed by the complete particular solutions  $\{\psi_i^\pm\}$ . Therefore, we may choose  $k_i$  such that

$$\lambda_{\min}(A(k_i)) = \min_k \lambda(A(k)), \quad (8)$$

as  $m \rightarrow \infty$  and  $n \rightarrow \infty$ . We now present the following algorithm to find the sequence  $\{k_i\}$ .

**Algorithm (A)** for seeking eigenvalues and eigenfunctions:

**Step 1.** Choose suitable term numbers  $m$  and  $n$ , and a good initial values of  $k^2$  near to the target eigenvalue  $\lambda_l$ .

**Step 2.** Based on the local particular solutions  $\{\psi_i^\pm\}$  form the admissible functions  $u_{m,n}$ .

**Step 3.** For solving problem (6), the solution  $u_{m,n}$  is obtained from the TM by the least squares method using the QR method or the singular value decomposition [1, 3]. Then the scaled solution  $\bar{u}_{m,n}$ , and the minimal eigenvalue is given by

$$f(k) = \lambda_{\min}(A(k)) = d_{\min}^2, \quad (9)$$

where  $d_{\min}$  is the smallest singular value.

**Step 4.** If  $f(k)$  is satisfactorily small, the values  $k^2$  can be regarded as a good approximation to  $\lambda_l$ . So  $\bar{u}_{m,n}$  can approximate  $\phi_l$ . Otherwise, we obtain a new value of  $k$  to minimize  $f(k)$  in (8), based on Algorithm (B) given below, and then return back to Step 2. If  $f(k)$  can not be reduced sufficiently after many iterations through Step 2-3, we should reasonably increase the term numbers,  $m$  and  $n$ , and then go to Step 1 for a new trial computation.

**Algorithm (B)** for minimizing  $f(k)$ :

**Step 1.** Give three good, distinct initial values

$$k_i \approx \sqrt{\lambda_l}, \quad i = 0, 1, 2, \quad (10)$$

and evaluate the target eigenvalue  $\lambda_l$  by some numerical methods, for instance, by the QR method or the singular value decomposition [1, 3].

**Step 2.** Compute

$$k_{n+1} = \frac{k_n + k_{n-1}}{2} - \frac{1}{2} \frac{f[k_n, k_{n-1}]}{f[k_n, k_{n-1}, k_{n-2}]}, \quad n \geq 2, \quad (11)$$

where  $f(k) = \lambda_{\min}(A(k))$ .

**Step 3.** Stop if  $k_{n+1}$  is satisfactory, otherwise return to Step 1.

To integrate Algorithm (B) with Algorithm (A), we may embed (11) into Step 4 in Algorithm (A), and should also supply three good guesses (10).

**3 Summary.** To close this paper, let us summarize the nature and novelties of these new algorithms for eigenvalue problems, and give a few concluding remarks.

- (a) The new algorithms rely on the Helmholtz equation (6) by modifying  $k$  to lead to a degeneracy. The degeneracy is measured by the infinitesimal values of the minimal eigenvalue of the stiffness matrix  $A(k)$ , and the modification to  $k$  is realized by Algorithm (B). Algorithms (A) and (B) are based on the fact that the eigenfunctions of (4) will dominate the solutions of (6) when a degeneracy occurs.

- (b) The degeneracy plays an important role in our algorithms. The leading coefficients such as  $c_1$  are huge, and the scale solutions are recommended due to simplicity and high accuracy of  $c_1$ . It is interesting to note that arbitrariness of the bounded function  $g(\neq 0)$  in (6) does not influence much on the final eigenvalue solutions of the algorithms. Hence we may simply choose  $g|_{\Gamma} = 1$  in computation.
- (c) Based on a minimum of a interpolatory quadratic function, a specific iteration of Algorithm (B) is designed to conduct the calculation of eigenvalue and eigenfunctions effectively. Algorithm (B) may be regarded as a variation of Muller's method for real roots. Since matrix  $A$  is symmetric, the eigenvalues of  $\lambda_{\min}(A(k))$  are all real. Of course, Algorithm (B) is expected to be better than Muller's method.

## References

- [1] K.E. Atkinson, **An Introduction to Numerical Analysis (Sec. Ed.)**, Wiley John & Sons, New York (1989).
- [2] L. Fox, P. Henrici and C. Moler, Approximations and bounds for eigenvalues of elliptic operators, *SIAM J. Numer. Anal.*, **4**, 89–102 (1967).
- [3] G.H. Golub and C.F. van Loan, **Matrix Computation (Sec. Ed.)**, John Hopkins University Press, Baltimore (1989).
- [4] Z.C. Li, **Combined Methods for Elliptic Equations with Singularities, Interfaces and Infinities**, Kluwer Academic Publishers, Dordrecht, London (1998).
- [5] Z.C. Li, R. Mathon and P. Sermer, Boundary methods for solving elliptic problems with singularities and interfaces, *SIAM J. Numer. Anal.*, **24**, 487–498 (1987).
- [6] T.T. Lu, H.Y. Hu and Z.C. Li, Highly accurate solutions of Motz's and the cracked beam problems, *Engineering Analysis with Boundary Elements*, **28**, 1387–1403 (2004).
- [7] M. Ortega, **Numerical Analysis, A Second Course**, SIAM Philadelphia (1990).
- [8] E. Trefftz, Ein Gegenstück zum Ritz'schen Verfahren, *Proceeding of the 2nd In. Cong. Appl. Mech.*, Zurich, 131–137 (1926).

## The flux-correct Green element method for linear and nonlinear potential flows

Akpofure E. Taigbenu

*School of Civil and Environmental Engineering, University of the Witwatersrand. P. Bag 3,  
Johannesburg, WITS 2050. South Africa. Email: [aetaigbenu@civil.wits.ac.za](mailto:aetaigbenu@civil.wits.ac.za)*

**Keywords:** Green element method, flux-based formulation, boundary element theory, steady and transient potential flows.

### Abstract

One of the unique computational features of the boundary element method is its ability to correctly calculate the flux and derivatives of the potential for potential flow problems. When the theory is implemented in the finite element sense, as in the Green element method (GEM), that feature is only retained on the boundary but, within the domain, numerical differentiation is carried out to avoid calculating the internal fluxes. While that has the advantage of solving sparse and banded matrices comparable to those in finite element methodology, it introduces errors that affect the quality of the numerical solution. In many applications where there is the need to evaluate directional derivatives of the primary variable or fluxes at internal points, methods which do numerical differentiation give erroneous results that, in certain instances, have nothing to do with the physical phenomenon being modeled. Since the boundary element theory provides for flux correct solutions, it can be exploited within the Green element method to estimate internal fluxes. That is the thrust of this paper. The usefulness of this approach is that while a greater number of degrees of freedom have to be addressed, it yields very reliable and accurate solution estimates with grid much coarser than in earlier Green element calculations. Two examples of linear and nonlinear potential flow problems are used to demonstrate the computational advantages of the flux-correct Green element formulation.

### Introduction

This paper solves by GEM the mathematical description of the problem given by

$$\nabla \cdot (K \nabla h) = \frac{\partial h}{\partial t} + f(x, y, t) \quad (1)$$

where  $\nabla$  is the 2-D gradient operator and  $h$  is the dependent or primary variable, and the medium parameter  $K$  is allowed to have spatial variation and dependence on the primary variable (the nonlinear case). Previous GEM formulations [1, 2, 3] of eq (1) have implemented the boundary element theory in an element-by-element fashion and numerically differentiated internal fluxes in the terms of  $h$  to achieve sparse banded matrices that are then decomposed. The accuracy of the formulation is degraded by the numerical approximation of the internal fluxes when linear elements are used and, to enhance accuracy, Hermitian interpolation have been used in 1-D [4] and Overhauser interpolation in 2-D [5]. Pecher et al. [6] proposed for the steady form of eq (1) a Green element formulation that replaces the normal fluxes with fluxes in the Cartesian coordinate directions. While that approach reduces the number of degrees of freedom at the internal nodes considerably, it requires reformulating the differential equation and is not amenable to irregular flow geometries. In this work, the normal fluxes are directly calculated. The issue of closure of the algebraic equations at internal nodes as a result of having more degrees of freedom than equations is addressed in a unique manner that does not resort to artificially relocating nodes nor imposing certain conditions on the geometry of the elements meeting at the internal node. It involves providing an additional equation for the continuity of the fluxes at the internal point. One advantage of this formulation, referred to as the flux GEM, is that the complete solution information becomes available for each element so that detailed solution at any point/node is obtained by the implementation of the integrations within the element in which belongs the node without recourse to the entire flow region. The formulation is essentially amenable to any kind of elements used to discretize the computational region. Two examples (a steady linear case and an unsteady nonlinear case) are used to demonstrate the computational features of the current formulation.

**Green element formulation**

The flow eq (1) is rearranged to give

$$\nabla^2 h = -\nabla\Phi \cdot \nabla h + \Psi \left( \frac{\partial h}{\partial t} + f(x, y, t) \right) \quad (2)$$

where  $\Phi = \ln K$  and  $\Psi = 1/K$ . Applying Green's identity to eq (2) and using the fundamental solution to  $\nabla^2 G = \delta(r - r_i)$ , that is  $G = \ln(r - r_i)$ , gives the integral representation to eq (2) [7, 8]. That is

$$-\lambda h_i + \int_{\Gamma} \left( h \frac{\partial G}{\partial n} + G \frac{q}{K} \right) ds + \iint_{\Omega} G \left[ -\nabla\Phi \cdot \nabla h + \Psi \left( \frac{\partial h}{\partial t} + f \right) \right] dA = 0 \quad (3)$$

where  $h_i$  is the primary variable at the source point, and  $\lambda$  is the nodal angle at the source point from the Cauchy integration of the Dirac delta function. In eq (3),  $q = -K\nabla h \cdot n$  is the normal flux at the boundary. Eq (3) applies equally to the entire flow domain and a computational element that is used to discretised the flow domain. Implementing eq (3) in the Green element sense requires prescribing suitable interpolation representations of the functional quantities over a typical element, and aggregating the elemental integrations for all the elements [9]. Linear interpolation functions are used for all quantities in this work. For a typical element, implementation of eq (3) takes the matrix form

$$\mathbf{A}\mathbf{h} + \mathbf{B}\mathbf{q} + \mathbf{T} \frac{d\mathbf{h}}{dt} = \mathbf{R} \quad (4)$$

The character of the elemental matrices is very much dependent on the geometry of the elements used to discretized the solution domain. The current formulation has been programmed with rectangular and triangular elements and, using Fig. 1, the element matrices depend on  $a$  and  $b$  for rectangular elements, and  $\eta$ ,  $d_1$  and  $d_2$  for triangular elements. Using a generalized finite differencing within the time interval  $\Delta t = t_2 - t_1$  with a weighting factor,  $\alpha$  ( $0 \leq \alpha \leq 1$ ), eq (4) becomes

$$\left( \alpha \mathbf{A} + \frac{\mathbf{T}}{\Delta t} \right) \mathbf{h}^{(2)} + \alpha \mathbf{B}\mathbf{q}^{(2)} = \alpha \mathbf{R}^{(2)} + \omega \mathbf{R}^{(1)} + \left( \frac{\mathbf{T}}{\Delta t} - \omega \mathbf{A} \right) \mathbf{h}^{(1)} - \omega \mathbf{B}\mathbf{q}^{(1)} \quad (5)$$

where  $\omega = 1 - \alpha$ , and the superscripts (2) denote quantities at current time  $t_2$  and (1) at previous time  $t_1$ . Eq (5) can be written in a simpler manner with unknown quantities that are calculated at current time on the left hand side, and known quantities on the right hand side. That is

$$\mathbf{P}\mathbf{h} + \mathbf{L}\mathbf{q} = \mathbf{S} \quad (6)$$

Eq (6) is nonlinear because the matrices  $\mathbf{P}$  and  $\mathbf{L}$  depend on the primary variable. Its solution can be addressed using either the Picard or Newton-Raphson linearization technique, and then a matrix solver. It should be pointed out that although the coefficient matrix is banded, its bandwidth is larger than that from earlier Green element formulation which numerically differentiated the internal fluxes.

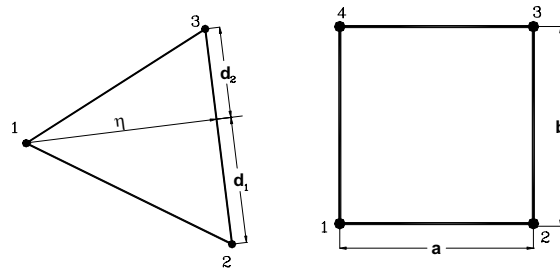


**Figure 1: Triangular and rectangular elements.**

**Treating Internal nodes**

At internal nodes, the number of degrees of freedom that is generated by this formulation is  $N + 1$ , in which there are  $N$  normal fluxes ( $N$  also equals the number of elements meeting at the internal node), and one

primary variable. Reference can be made to Fig. 2 where  $N = 4$  elements meet at the internal node. A closure problem arises because the number of element equations generated is one less than the number of unknowns. In the past resolution of such closure problems in boundary element circles has been carried out by artificially creating additional nodes and relocating them by small distances from the original location of the internal node along the internal segments [7]. That approach is not followed here. Rather, an additional equation that expresses the continuity of the normal fluxes at the node is written. It essentially states that the algebraic sum of the normal fluxes equals the strength of source/sink at the node. If no source/sink exist at the internal node, then the additional equation becomes

$$\sum q = 0 \quad (7)$$

To effect eq (7), it is prudent to adopt a convention that fluxes are in the direction from a higher numbered element to a lower numbered one, and are considered positive when their turning effect about the internal node is clockwise. It should be noted that this convention can be altered as long as there is consistency in tracking these normal fluxes. With this additional equation, the closure problem is resolved.

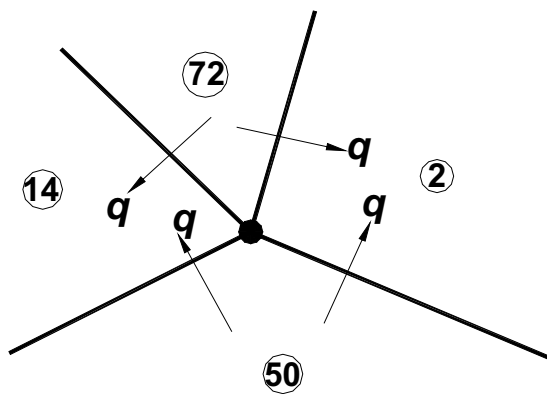


**Figure 2: Treatment of fluxes at internal with arbitrarily numbered elements (circled).**

#### **Complete Solution Characterization in the Element**

By resolving the closure problem at the internal nodes, the formulation is capable of providing the complete solution information (primary variable and normal fluxes) at every node (external and internal). At external nodes, there is no closure problem because of the availability of the prescribed boundary condition on the primary variable or normal flux. With the complete solution information available for each element, any solution that is required at a point other than the grid point in a particular element is obtained by implementing the integrations in eq (3) strictly within that element without recourse to other elements in the flow region. This is very significant for two reasons: the first being that the solution at points other than grid points is more easily calculated, and secondly it provides a means of refining a coarse grid and calculating solutions at points of interest that may not coincide with the grid points. This feature of this formulation is demonstrated with two examples.

#### **Numerical Examples**

Two examples are used to demonstrate the computational advantage of the current formulation. The first is a steady linear flow case and the second is a nonlinear transient flow example. In each case, it is demonstrated that high solution accuracy is achieved with coarse grid of elements, and numerical solutions at other points are obtained by implementing the integrations within the element to which the point belongs.

#### **Example 1**

This example is a steady state form of governing eq (1) in a square domain  $[0.5 \times 0.5]$  with no forcing term. It is also linear. The parameter  $K$  takes unit value, and the boundary conditions are:

$$h(0, y) = 0; \quad \frac{\partial h}{\partial x}(0.5, y) = 0; \quad \frac{\partial h}{\partial y}(x, 0) = 0; \quad h(x, 0.5) = \sin(\pi x) \quad (10)$$

The exact solution to this example is known and will be used for benchmarking. The example has been solved by Taigbenu [9] and Archer [5] with previous GEM formulations that numerically differentiate the internal fluxes; Taigbenu's formulation used linear elements and is herein referred to as linear GEM, while Archer's, which used Overhauser shape functions, is referred to as Overhauser GEM. The reported results by Taigbenu [9] with linear GEM on  $4 \times 4$  grid of rectangular elements gave maximum and mean relative errors of 4.57% and 1.30%, respectively, for nodal  $h$  values. The results with Overhauser GEM and Galerkin finite element method (FEM) that are presented in Table 1 were taken from Archer [5]. The Overhauser GEM cannot be applied to a  $2 \times 2$  because there is insufficient number of nodes to generate the interpolation functions. The results in Table 1 indicate that the current formulation provides excellent results with a coarse grid of  $2 \times 2$  even when only 2 elements are used to linearly interpolate  $\sin(\pi x)$  at the upper boundary. As earlier indicated, the flux GEM provides complete solution information for the primary variable and fluxes. With the  $2 \times 2$  grid, the solutions generated at points other than grid points are presented in Table 2 and asterisked. It should be pointed out that the solutions at those points were obtained using only the calculated grid point solutions within the element in which the points are located. The accuracy of these solutions at those points attest to the high quality of the solutions for  $h$  and  $q$  within each element. In addition, Table 2 shows a comparison of the flux GEM solution for the fluxes and the exact for the  $4 \times 4$  grid. In the x-direction, the maximum and mean relative errors in the flux values are respectively 1.59% and 0.95%, while similar values for fluxes in the y-direction are 1.47% and 0.78%. These values are within the same error bounds for  $h$ . Worth noting is the escalation in the total number of degrees of freedom,  $M$ , and size of bandwidth,  $B$ , with grid. In this example,  $M = 17$  and  $B = 13$  for the  $2 \times 2$  grid, while  $M = 73$  and  $B = 35$  for the  $4 \times 4$ , and  $M = 305$  and  $B = 63$  for the  $8 \times 8$  grid. The computational advantage of the flux GEM lies in its ability to correctly calculate  $h$  and  $q$  with coarse grids.

Grid	Overhauser GEM		Flux GEM		FEM	
	Max rel. error (%)	Mean rel. error (%)	Max rel. error (%)	Mean rel. error (%)	Max rel. error (%)	Mean rel. error (%)
$2 \times 2$			5.24	1.69		
$4 \times 4$	2.14	0.69	0.95	0.44	1.88	0.86
$8 \times 8$	0.35	0.10	0.24	0.12	0.47	0.24

**Table 1: Comparison of Overhauser GEM, flux GEM and FEM for example 1**

### Example 2

This example, commonly referred as the Boussinesq example [10], is a nonlinear case of eq (1) with no forcing term. The parameter  $K = h$  and the flow is only in the  $x$  direction. The boundary and initial are:

$$h(x = 0, t) = 0; \quad q(x = 1, t) = 0; \quad h(x, t = 0) = \frac{B_x(0.67, 0.5)}{B(0.67, 0.5)} \quad (11)$$

where  $B_x$  and  $B$  denote the incomplete and complete Beta functions. The exact solution provided by Boussinesq [10] is used to evaluate the performance of the current formulation. Using a uniform time step of 0.05 and the fully implicit scheme in the current formulation, three simulations with 3, 5 and 10 rectangular elements are used to discretize the flow region. Comparison of the flux GEM solution with 10 elements and exact solution for  $h$  at times of 0.25, 0.5, 1 and 2 is presented in Fig. 3a, while that for the flux at  $x = 0$  is presented in Fig. 3b. As in the previous example, solution for  $h$  is generated with the 3-element and 5-element simulations at points other than grid points using calculated solutions within elements to which those points are located. The points are chosen to correspond to the grid points of the 10-element simulations. An error plot of the three simulations is presented in Fig. 4. Error bound for the 3-element simulation is comparable to than of the 5- and 10-element simulations.

x	y	Exact		Flux GEM (4 × 4 grid)				Flux GEM (2 × 2 grid)	
		q <sub>x</sub>	q <sub>y</sub>	q <sub>x</sub>	% rel. error	q <sub>y</sub>	% rel. error	h	% rel. error
0.000	0.000	1.2520	0.0000	1.2321	1.59	0.0000	0.00	0.0000▪	0.00
0.125	0.000	1.1567	0.0000	1.1383	1.59	0.0000	0.00	0.1498*	1.76
0.250	0.000	0.8853	0.0000	0.8712	1.59	0.0000	0.00	0.2708	3.89
0.375	0.000	0.4791	0.0000	0.4715	1.59	0.0000	0.00	0.3617*	1.76
0.500	0.000	0.0000	0.0000	0.0000	0.00	0.0000	0.00	0.3830	3.89
0.000	0.125	1.3498	0.0000	1.3296	1.50	0.0000	0.00	0.0000▪	0.00
0.125	0.125	1.2471	0.1930	1.2284	1.50	0.1950	1.02	0.1587*	3.49
0.250	0.125	0.9545	0.3567	0.9402	1.50	0.3603	1.02	0.2927*	3.68
0.375	0.125	0.5166	0.4660	0.5088	1.50	0.4708	1.02	0.3831*	3.49
0.500	0.125	0.0000	0.5044	0.0000	0.00	0.5096	1.02	0.4071*	5.24
0.000	0.250	1.6585	0.0000	1.6377	1.25	0.0000	0.00	0.0000▪	0.0
0.125	0.250	1.5322	0.4162	1.5130	1.25	0.4209	1.12	0.1990*	1.49
0.250	0.250	1.1727	0.7691	1.1580	1.25	0.7777	1.12	0.3639	2.51
0.375	0.250	0.6347	1.0048	0.6267	1.25	1.0161	1.12	0.4804*	1.49
0.500	0.250	0.0000	1.0876	0.0000	0.00	1.0998	1.12	0.5147	2.51
0.000	0.375	2.2262	0.0000	2.2050	0.95	0.0000	0.00	0.0000▪	0.0
0.125	0.375	2.0567	0.7044	2.0371	0.95	0.7134	1.27	0.2678*	1.26
0.250	0.375	1.5741	1.3016	1.5592	0.95	1.3181	1.27	0.4938*	1.45
0.375	0.375	0.8519	1.7006	0.8438	0.95	1.7222	1.27	0.6464*	1.26
0.500	0.375	0.0000	1.8407	0.0000	0.00	1.8641	1.27	0.6870*	3.05
0.000	0.500	3.1416	0.0000	3.1214	0.64	0.0000	0.00	0.0000▪	0.0
0.125	0.500	2.9025	1.1026	2.8838	0.64	1.1188	1.47	0.3827▪	0.0
0.250	0.500	2.2214	2.0374	2.2071	0.64	2.0673	1.47	0.7071▪	0.0
0.375	0.500	1.2022	2.6620	1.1945	0.64	2.7011	1.47	0.9239▪	0.0
0.500	0.500	0.0000	2.8813	0.0000	0.00	2.9236	1.47	1.0000▪	0.0
Mean					0.95		0.78		1.69

Table 2: Flux GEM solution for  $q$  with  $4 \times 4$  grid and for  $h$  with  $2 \times 2$  grid, example 1 (\*: generated solutions, ▪: boundary conditions).

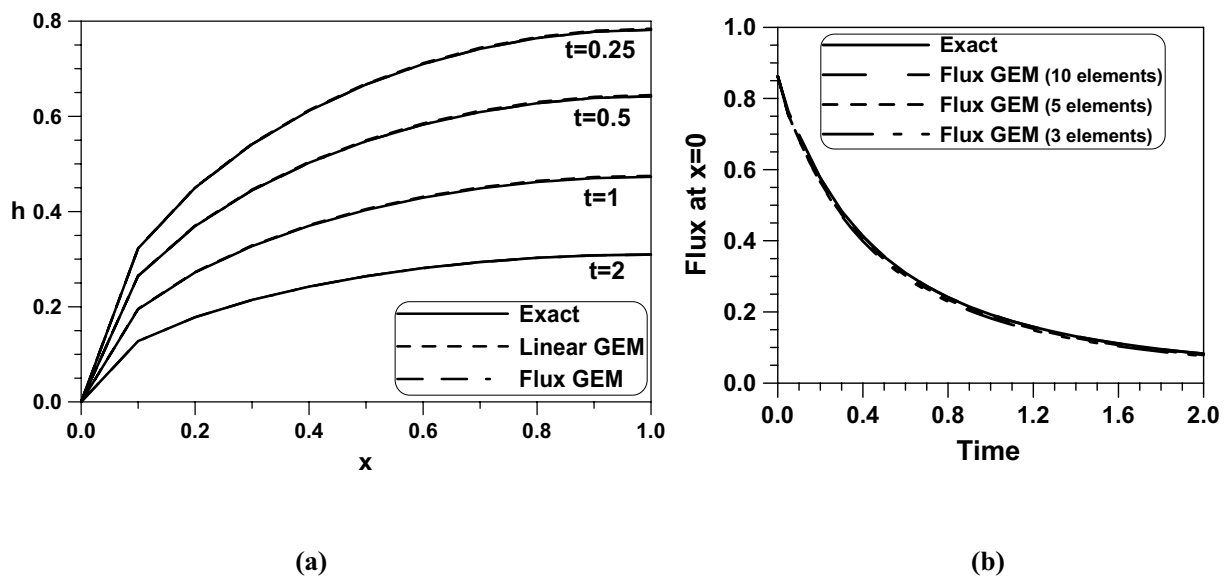


Figure 3: Comparison of GEM and exact for: (a)  $h$ , and: (b)  $q$  for example 2.

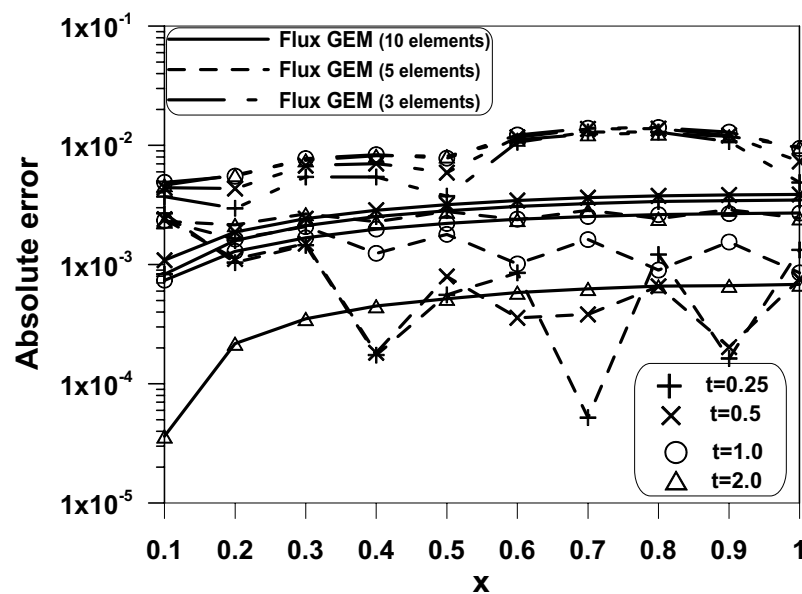


Figure 4: Error plots of 3 flux GEM simulations for example 2.

### Conclusion

This paper has presented the flux-based GEM formulation for linear and nonlinear potential flow problems. The formulation has some computational advantages over the previous one that numerically differentiates the internal fluxes in the sense that it provides complete solution information in each element, and achieves high accuracy with coarse discretization. The coarseness of the discretization compensates for the larger degrees of freedom and bandwidth of the coefficient matrix that are encountered with the formulation. Furthermore, the complete solution information available for each element implies that the solution at a point other than a grid point is obtained only from the integrations within the element to which the point is located without recourse to the entire flow domain. That provides tremendous savings in computing resources when evaluating such solutions.

### References

1. A.E. Taigbenu *The Green Element Method*, Int. J. Numerical Methods in Engrg., **38**, 2241-2263 (1995).
2. A.E. Taigbenu, and O.O. Onyejekwe *Green's Function-based Integral Approaches to Nonlinear Transient boundary-value problems (II)*, App. Math. Mod., **23**, 241-253 (1999).
3. A.E. Taigbenu *Green element calculations of nonlinear heat conduction with a time-dependent fundamental solution*, Engrg. Anal. with Boundary Elements, **28**(1), 53-60 (2004).
4. A.E. Taigbenu *Enhancing the accuracy of the solution to unsaturated flow by a Hermitian Green element model*, Adv. Engrg Software, **29**(2), 113-118 (1998).
5. R. Archer  *$C_1$  Continuous Solutions from the Green Element Method using Overhauser Elements*, App. Num. Math., in press (2005).
6. R. Pecher, S.D. Harris, R.J. Knipe, L. Elliot and D.B. Ingham, *New formulation of the Green element method to maintain its second-order accuracy in 2D/3D*, Engrg. Anal. with Boundary Elements, **25**, 211-219 (2001).
7. J.A. Liggett and P. L-F. Liu *The Boundary Integral Equation Method for Porous Media Flow*, George Allen & Unwin (1983).
8. P.K. Banerjee, and R. Butterfield *Boundary Element Methods in Engineering Science*, McGraw-Hill, London (1981).
9. Taigbenu, A.E. *The Green Element Method*, Kluwer, Boston, USA (1999).
10. J. Boussinesq *Recherches Theoretiques sur l'ecoulement des Nappes d'eau infiltrées dans sol et sur le debit des sources*, J. de Mathematiques pures et Appliquees, **10** (5<sup>th</sup> series), 5-78, 363-394 (1904).

## A BEM for the propagation of non-linear free-surface waves

S A Kinnas<sup>1</sup>, V Vinayan<sup>2</sup>

<sup>1,2</sup> The University of Texas at Austin, Civil, Architectural and Environmental  
 Engineering Department-EWRE, 1 University Station C1786,  
 Austin, TX 78712-0273,

<sup>1</sup>[kinnas@mail.utexas.edu](mailto:kinnas@mail.utexas.edu), <sup>2</sup>[vinayan@mail.utexas.edu](mailto:vinayan@mail.utexas.edu)

**Keywords:** BEM, Boundary Element Method, Non-Linear free-surface, Stokes wave

### Abstract.

This paper presents the development of a BEM model for the propagation of nonlinear free-surface waves. The model is validated through a rigorous study of the propagation of fifth-order Stokes waves (Figure 1) and then applied to the analysis of the flow around 2-D FPSO hull-sections (Figure 2) subject to forced roll motions.

An ideal fluid is assumed and the flow is described in terms of a velocity potential with the additional assumption of being irrotational. The Stokes-wave propagation and the roll-motion analysis of the 2-D FPSO hull are formulated as an initial boundary-value problem for the velocity potential and solved for using the BEM model combined with a semi-Lagrangian approach for updating the free-surface boundary conditions.

The flow is described by a velocity potential  $\Phi(\vec{x}, t)$  which satisfies the Laplace equation

$$\nabla^2 \Phi(\vec{x}, t) = 0; \quad \vec{x} \in \Omega(t) \quad (1)$$

with appropriate boundary conditions on the domain boundaries. A detailed description of the boundary conditions for the roll-motion analysis is provided in [1]. For the Stokes-wave propagation, analytical velocities are applied on the upstream (**U**) and downstream (**D**) boundaries, and a no-flux boundary condition on **B**. The ability of the algorithm to propagate an initially specified wave through the domain, subject to the time-dependent boundary conditions, is studied.

Fully nonlinear kinematic (KFSBC) and dynamic boundary (DFSBC) conditions are applied on the exact free-surface.

$$\text{KFSBC} \quad : \quad \frac{\delta \eta}{\delta t} = \frac{\partial \Phi}{\partial y} - \frac{\partial \Phi}{\partial x} \frac{\partial \eta}{\partial x} \quad (2.1)$$

$$\text{DFSBC} \quad : \quad \frac{\delta \Phi}{\delta t} = -\frac{1}{2} |\nabla \Phi|^2 - g\eta + v_p \frac{\partial \Phi}{\partial y} \quad (2.2)$$

In the semi-Lagrangian approach, the wave elevation is determined at the panel nodes that are followed only along the vertical direction.

The boundary value problem for the velocity potential is converted into a boundary-integral-equation (BIE) by introducing a Green's function  $G(p, q) = \ln(r_{pq})$ . The BIE obtained by applying Green's third identity to  $\Phi(\vec{x}, t)$  and  $G(p, q)$  is

$$\frac{\Phi(p)}{2} + \int_{\Gamma} \Phi(q) \frac{\partial G(p, q)}{\partial n(q)} d\Gamma_q = \int_{\Gamma} G(p, q) \frac{\partial \Phi(q)}{\partial n(q)} d\Gamma_q \quad (3)$$

where  $\Gamma$  represents the boundary of the fluid domain.

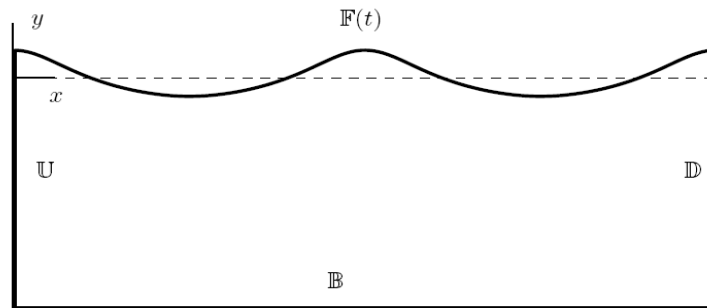


**Figure 1 : BEM Domain: Fifth Order Stokes Waves**

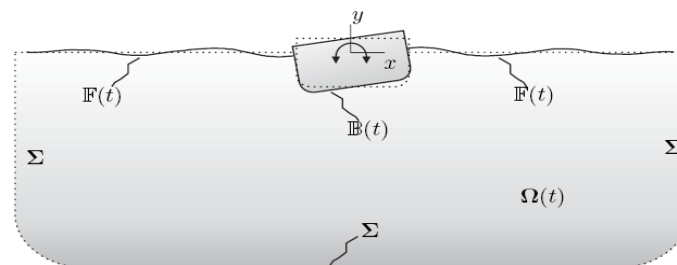


**Figure 2 BEM Domain: FPSO Roll-motion**

Two important aspects that dominate the numerical formulation of the problem are the solution of the boundary integral equation and the time integration of the free-surface boundary conditions. A low-order method, constant strength elements with the computational nodes at the mid-point of each panel/element, is used to approximate the BIE. The accuracy of the low-order method was found to be affected by discontinuities in the velocity potential/flux at the intersection of the domain boundaries. To improve the accuracy, an iterative scheme similar to that described in [2] is applied to take into account the difference between a constant strength and continuous distribution of velocity potential/flux on the domain boundaries. The BIE is solved and the iterative scheme is applied at each stage of a Fourth-order Runge-Kutta scheme, used to integrate the time-dependent free-surface boundary conditions (2.1) and (2.2), and advance the solution in time.

Results for the wave-propagation and FPSO roll-motion problems are presented in terms of the predicted wave-profiles. In addition, for the wave-propagation of the Stokes-wave, the velocity potential and velocities on the different domain boundaries are compared with the analytical solution. Results pertaining to a convergence-study of the scheme with respect to the panel size and the time-step size are also presented.

#### References

[1] V. Vinayan, S. A. Kinnas and Y. Yu *Modeling of flow around FPSO hull sections subject to roll motions : effects of nonlinear boundary conditions*, 24<sup>th</sup> International conference on Offshore Mechanics and Arctic Engineering (OMAE 2005), Halkidiki, Greece (to be presented), (2005)

[2] S. A. Kinnas and C-Y Hsin *The local error of a low-order boundary element method at the trailing edge of a hydrofoil and its effect on the global solution*. *Computers Fluids*, Vol. 23, No.1, pp 63-75, (1994)